

Electrical Impedance Tomography in 3D:  
characterization and evaluation

by

Justin Wagenaar

A thesis submitted to the Faculty of Graduate and Postdoctoral  
Affairs in partial fulfillment of the requirements  
for the degree of

Master of Applied Science

in

Biomedical Engineering

Department of Systems and Computing Engineering  
Carleton University  
Ottawa, Ontario

© 2015

Justin Wagenaar

## ABSTRACT

Electrical Impedance Tomography (EIT) uses body surface electrical stimulation and measurements to create images of the conductivity contrasting fluids. Identifying and monitoring regions of inhomogeneous behaviour in the lungs can be a vital part of the treatment of lung injuries. Traditionally, EIT uses a placement of electrodes in a 2D ring around the thorax, and thus produces cross-sectional images. 3D EIT has a potential to image regional inhomogeneities with 3D spatial extent and to improve planar resolution over 2D EIT. However, while 3D reconstruction algorithms are available, little evaluation has been done to understand the performance of 3D EIT in terms of the measurement configurations available. This thesis focuses on this evaluation task. It has three main objectives. First, to examine different measurement patterns, and determine the best-suited pattern for *in vivo* 3D lung imaging of regional inhomogeneities. Second, to capture regional inhomogeneities in the lungs caused by gravitational effects by recording EIT on human subjects in the standing, sitting, supping, and decline postures. This method is used in order to cause and measure regional inhomogeneities in the lungs. Third, to verify the ability of 3D EIT to measure global lung volume changes in volunteers by comparing reconstructed images to spirometry lung volume measurements.

To address these objectives, the thesis develops an analysis methodology, and applies it to data from simulation, phantom, and measurements on 8 healthy volunteers. Results indicate that 3D EIT can provide meaningful and stable reading of the global change in lung volume. Functional EIT images are created from inhalation curve features to analyze the effect of posture on regional lung behaviour with the greater lung activity moving upwards in the thorax when moving from the standing postures to a declined posture. The Planar and Zigzag Offset patterns show statistically significant difference in vertical lung activity between the decline and standing postures and the supine and standing postures for several fEIT features. While inconsistent, the positive results indicate that 3D EIT is capable of capturing region lung inhomogeneities in 3D space. Overall, this thesis presents analysis methodologies (simulation, phantom, and experimental) to characterize and optimize 3D EIT imaging.

## ACKNOWLEDGEMENTS

First, I would like to extend a huge thank you to my supervisor, Dr. Andy Adler, whose unwavering support and encouragement led me through the steps and pitfalls of this process. He was a reliable source of sound advice, experience, and understanding.

I would also like to thank Bartek Grychtol, who provided excellent insight into the inner workings of the 3D GREIT reconstruction method. His input and feedback have been extremely important during the writing process. I would like to acknowledge as well the rest of my colleagues in the biomedical field and in the academic community at large. The discussions, sharing, and collaborations have been truly rewarding.

I would like to extend my appreciation to the group of volunteers who were an essential part of this work. Additionally the Athletics Department graciously provided space and equipment to perform the experiment. I would like to add a special thanks to Marta Wein and Nicolas Westcott for their cooperation in this regard.

Finally I would like to thank my family, my girlfriend and her dog Jio who all provided me with their love and support throughout this process. I would not have made it without you.

## Table of Contents

ABSTRACT .....	ii
ACKNOWLEDGEMENTS .....	iii
LIST OF TABLES .....	viii
LIST OF FIGURES .....	ix
1 Introduction .....	1
1.1 Motivation .....	1
1.2 Thesis Objectives .....	3
1.3 Outline .....	4
1.4 Contributions .....	4
2 Background .....	6
2.1 What is Electrical Impedance Tomography? .....	6
2.2 What is the Inverse Problem? .....	7
2.3 GREIT .....	8
2.4 Electrical impedance tomography in 3D .....	12
2.5 Electrode positions & placement strategies .....	13
2.5.1 Electrode Placement Configurations for 3D EIT .....	14
2.5.2 Distinguishability .....	18
2.6 EIT in Medical Applications .....	19
2.6.1 EIT and Lung Imaging .....	19
2.6.2 EIT and Heart Imaging .....	21
2.6.3 EIT and Brain Imaging .....	21
2.6.4 EIT and Breast Cancer Detection .....	22
2.7 EIT vs. Lung Mechanics .....	23

2.7.1	Electrode Plane Height.....	23
2.7.2	Cystic Fibrosis.....	24
2.7.3	EIT vs. Posture/Gravity.....	24
3	Reconstruction Approach .....	26
3.1	3D GREIT Method.....	26
3.2	3D GREIT vs. 2D GREIT.....	28
3.2.1	Method .....	28
3.2.2	Results.....	29
4	Simulations.....	32
4.1	EIT Measurement Patterns .....	32
4.2	Simulation Models .....	34
4.2.1	Cylindrical Model .....	34
4.2.2	Thorax Model.....	35
4.3	Analysis Approach .....	36
4.3.1	GREIT Parameters .....	36
4.3.2	Noise Stability .....	39
4.4	Simulation Methods.....	41
4.4.1	Electrode Placement Error.....	41
4.4.2	Electrode Impedance Error.....	44
4.5	Simulation Results.....	45
4.5.1	Electrode Placement Error.....	45
4.5.2	Electrode Impedance Error.....	52
4.6	Discussion.....	58
4.6.1	GREIT Parameters .....	58

4.6.2	Noise Stability .....	59
5	Tank Phantom Experiment .....	62
5.1	Experimental Apparatus.....	62
5.2	Experimental Procedure.....	64
5.3	Analysis Method.....	65
5.3.1	GREIT Parameters .....	65
5.3.2	Z-Constraint Score.....	66
5.4	Results .....	67
5.4.1	Qualitative Analysis.....	67
5.4.2	GREIT Parameters in the X-Y Plane .....	74
5.4.3	Z-Constraint.....	76
5.5	Discussion.....	78
5.5.1	Tank Phantom Results vs. Simulations Results.....	79
5.5.2	Pattern Selection for Human Measurements.....	80
6	Human Measurements .....	82
6.1	Motivations .....	82
6.2	Experimental Method .....	83
6.3	Analysis Method.....	88
6.3.1	Spirometry vs. EIT .....	88
6.3.2	Vertical Regional Thoracic Effects.....	90
6.4	Results .....	96
6.4.1	Correlation .....	96
6.4.2	Root Mean Square Error .....	97
6.4.3	Vertical Gravity .....	98

6.5	Discussion.....	108
6.5.1	Spirometry vs. EIT .....	108
6.5.2	Functional EIT Images .....	109
6.5.3	Vertical Gravitational Effects .....	110
7	Conclusion.....	114
7.1	Future Work .....	119
	Appendix A.....	125
	Function EIT Image 1: Amplitude Difference .....	125
	Function EIT Image 2: Polynomial Coefficient $a_0$ .....	126
	Function EIT Image: Polynomial Coefficient $a_1$ .....	128
	Function EIT Image: Polynomial Coefficient $a_2$ .....	129

## LIST OF TABLES

<b>Table 1.</b> Reconstructed Images of a plastic block suspended in a cylindrical tank with <b>3.2 cm</b> electrode plane spacing. ....	70
<b>Table 2.</b> Reconstructed Images of a plastic block suspended in a cylindrical tank with <b>7.1 cm</b> electrode plane spacing. ....	72
<b>Table 3.</b> Qualitative Results for Tank Experiment Images for the 7 Measurement Patterns .....	78
<b>Table 4.</b> Quantitative Results of GREIT Parameter Performance for Tank Experiment Images ..	78
<b>Table 5.</b> Summary of Correlation results by pattern. ....	97
<b>Table 6.</b> Summary of RMSE results by measurement pattern. ....	98
<b>Table 7.</b> Qualitative Results of fEIT Images for Feature 1 .....	102
<b>Table 8.</b> Qualitative Results of fEIT Images for Feature 2. ....	103
<b>Table 9.</b> Qualitative Results of fEIT Images for Feature 3. ....	103
<b>Table 10.</b> Qualitative Results of fEIT Images for Feature 4. ....	104
<b>Table 11.</b> Results of paired t-test comparing %Activity slope values between postures. ....	108

## LIST OF FIGURES

<b>Figure 1.1</b> Current flow across a human thorax model.....	3
<b>Figure 2.1</b> EIT system block diagram .....	6
<b>Figure 2.2</b> GREIT algorithm target optimization.....	12
<b>Figure 2.3</b> GREIT performance figures of merit.....	12
<b>Figure 2.4</b> Aligned and Offset 3D electrode patterns.....	15
<b>Figure 2.5</b> 3D measurement patterns 1 through 4.....	16
<b>Figure 2.6</b> 3D measurement patterns 5 through 7.....	17
<b>Figure 2.7</b> PulmoVista 500 by Draeger. Image source [ <a href="http://campaigns.draeger.com/pulmovista500">http://campaigns.draeger.com/pulmovista500</a> ]. .....	21
<b>Figure 3.1</b> Reconstructed images using 2D GREIT and 3D GREIT methods.....	29
<b>Figure 3.2</b> Centre image slice from 2D GREIT method (left) and 3D GREIT method (right).....	30
<b>Figure 3.3</b> 3D GREIT images using different reconstruction planes. ....	30
<b>Figure 4.1</b> 3D EIT measurement patterns 1 through 5.....	33
<b>Figure 4.2</b> 3D EIT measurement patterns 7 and 8.....	34
<b>Figure 4.3</b> Cylindrical FEM model generated by EIDORS.....	35
<b>Figure 4.4</b> Thorax Model generated by EIDORS. ....	36
<b>Figure 4.5</b> GREIT performance figures of merit.....	38
<b>Figure 4.6</b> Block Diagram of method for calculation of Noise Stability measure. ....	40
<b>Figure 4.7</b> Method for electrode placement error.....	42
<b>Figure 4.8</b> Forward Model using FEM showing 7 reconstruction layers. ....	43
<b>Figure 4.9</b> Position of targets for GREIT parameter calculations. ....	44
<b>Figure 4.10</b> Graph of Position Error and Resolution with added electrode placement error.....	47
<b>Figure 4.11</b> Graph of absolute GREIT parameters by layer with electrode placement error. ....	48
<b>Figure 4.12</b> Graph of Noise Stability measure vs electrode placement error.....	50
<b>Figure 4.13</b> Graph of Position Error and Resolution with added electrode impedance error.....	53
<b>Figure 4.14</b> Graph of absolute GREIT parameters by layer with electrode impedance error. ....	55
<b>Figure 4.15</b> Graph of Noise Stability measure vs electrode impedance error. ....	56
<b>Figure 5.1</b> Tank Phantom experimental apparatus .....	62

<b>Figure 5.2</b> Dimensions of tank phantom experimental apparatus. ....	63
<b>Figure 5.3</b> Diagram of tank phantom experiment block placement locations.....	65
<b>Figure 5.4</b> Block diagram of analysis of measurement patterns using GREIT parameters. ....	66
<b>Figure 5.5</b> Diagram of Z-Constraint Score.....	67
<b>Figure 5.6</b> Graph of Amplitude vs. block position. ....	74
<b>Figure 5.7</b> Graph of Position Error vs. block position. ....	75
<b>Figure 5.8</b> Graph of Resolution vs. block position. ....	75
<b>Figure 5.9</b> Graph of Z-Constraint Score vs. block position. ....	77
<b>Figure 6.1</b> Experimental Protocol for Human Measurements experiment.....	84
<b>Figure 6.2</b> EIT Electrode Placement on male subject (aligned).....	85
<b>Figure 6.3</b> EIT Electrode Placement on male subject. (offset). ....	85
<b>Figure 6.4</b> Diagram of measurement patterns used in Human Measurements experiment.....	86
<b>Figure 6.5</b> Breathing protocol for Human Measurements experiment. ....	87
<b>Figure 6.6</b> Example of 6 <sup>th</sup> order polynomial line fit to the raw spirometry data. ....	90
<b>Figure 6.7</b> Block diagram of generation of functional EIT (fEIT) images. ....	91
<b>Figure 6.8</b> Segmentation of mean pixel amplitude from EIT image set.....	92
<b>Figure 6.9</b> Functional EIT images from features $f_1, f_2, f_3$ , and $f_4$ . ....	93
<b>Figure 6.10</b> Analysis method of vertical gravitational effects in fEIT images.....	95
<b>Figure 6.11</b> Graph of correlation between global EIT Amplitude and spirometry lung volume..	96
<b>Figure 6.12</b> Graph of RMSE between global EIT Amplitude vs. spirometry lung volume. ....	97
<b>Figure 6.13</b> Time series EIT images vs. fEIT images. ....	99
<b>Figure 6.14</b> A set of graphs of %Activity Layer Slope vs. Posture for all 8 subjects. ....	106
<b>Figure 6.15</b> A set of graphs of %Activity Layer Slope vs. Posture averaged over all 8 subjects.	107

# 1 Introduction

## 1.1 Motivation

Electrical Impedance Tomography (EIT) is an imaging technology that has been in development for medical applications since the late 1970's [1]. The technology applies current to a body and measures the resulting voltages at the body surface in order to reconstruct a map of the internal conductivity. EIT is suitable for imaging bodies comprised of regions of large contrasts in conductivity. The technology offers a number of advantages over other imaging technologies, which has led to continued interest and active research in the field. EIT offers a non-invasive, safe, real-time technology for imaging physiological functions. Furthermore the device is low cost and portable, and easy to use in combination with other medical devices.

There are a number of imaging technologies with significantly higher spatial resolution than EIT. However, these technologies have drawbacks of their own. Imaging technologies such as Magnetic Resonance Imaging (MRI) and Computed Tomography (CT) scanning devices tend to have lower temporal resolution [1]. CT scans also use dangerous radiation and exposure to patients needs to be minimized during medical procedures [2]. Finally, they tend to be stand-alone devices with bulky, stationary hardware, and cannot be used conjunction with other devices.

EIT does have its own disadvantages. The main issue is low spatial resolution. Image reconstruction using EIT is considered an ill-posed problem, in that the conductivity distribution has a higher degree of freedom than the measurements. This leads to multiple solutions for the conductivity distribution, and when noise is factored in, the solution uncertainty is even greater. The result is low-resolution, 'blobby' images. Results can be improved by advancements in reconstruction algorithms, reduction of measurement noise, and optimization of the measurement strategy.

The fact that EIT is a real-time, safe, portable imaging tool makes it a suitable imaging method for a number of applications. EIT is particularly well-suited for lung imaging. The lungs make up a large portion of the thorax cavity, and since the lungs are filled with air there is a strong contrast

in conductivity between lung regions and the surrounding tissue. Furthermore, the lungs are a dynamic system with constantly changing lung volume. EIT has been shown to be useful in a number of lung imaging contexts, such as providing real-time feedback during ventilation procedures [3] [4], and also characterizing mechanical properties of the lungs in cystic fibrosis patients [5]. There are clinical EIT devices available, and progress is being made particularly in using EIT images to control ventilation settings [2].

Currently most research and device development in the field of EIT focuses on 2D images. However, 3D imaging is an attractive possibility. A 3D EIT image has several apparent advantages over a 2D image. The approach can show regional inhomogeneities in a volume such as an organ, whereas a 2D image can only show a cross-section. A 3D reconstruction also takes into account the path of the electric field in 3 dimensions, whereas a 2D solution only considers the movement of the electric field through a plane. This means that a 2D image is influenced by the conductivity of regions outside of the reconstruction plane. The development and improvement of 3D EIT is therefore very valuable with the potential to show regional inhomogeneities while improving resolution. The higher computational requirements of 3D image reconstruction has been prohibitive in past years, but with the ever-increasing power of modern computing along with advancements in reconstruction algorithms, 3D imaging is becoming an increasingly relevant field of EIT research.

The optimization of EIT measurement protocols is another area which requires exploration and development. An EIT measurement system uses a large set of electrodes placed at the surface. Current is applied at one electrode pair and voltage measured at the remaining pairs. An example of the current flow is shown in Figure 1.1. Current is then applied at the next pair and voltage is measured at the remaining pairs. This is repeated for all stimulation pairs to form one measurement frame, which is then used to reconstruct an image. The most commonly used protocol for 2D EIT images has been the *adjacent* current patten, which uses adjacent electrodes for the stimulation and measurement pairs.

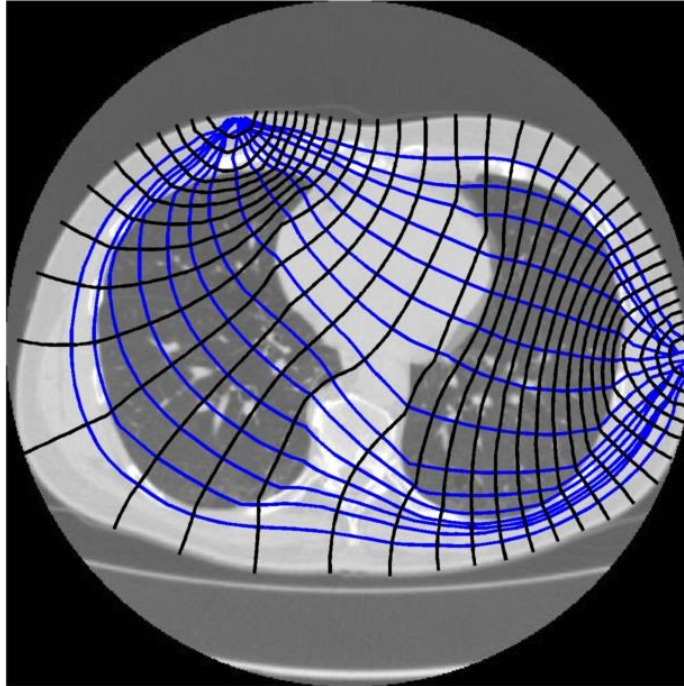


**Figure 1.1** Current flow across a human thorax model. Blue lines show current flow direction, black lines show field strength. Image source [6].

It has been shown that the *adjacent* current pattern is suboptimal [7], and that increasing the electrode spacing for both the stimulation and measurement electrodes can improve image quality. For 3D measurements using multiple bands of electrodes, there is greater flexibility in the measurement protocol. Research has been done to analyze the performance of different 3D measurement strategies [8], [9]. However, there is a need for further exploration of 3D measurement protocols, particularly during *in vivo* measurements.

## 1.2 Thesis Objectives

The purpose of this thesis is to analyze the performance of different measurement protocols for 3D EIT image reconstruction during *in vivo* imaging. This has been accomplished using a three stage process. First, simulations are run in order to obtain a measure of the baseline performance of different measurement protocols. Second, a phantom tank experiment is run in order to analyze the measurement protocols against real data. Finally, the top three performing measurement protocols are used to acquire EIT data on healthy human subjects in four different postures.

The goals of the thesis are as follows:

1. Compare 3D measurement patterns in terms of various image quality parameters using simulations, phantom tank experiment, and human measurements.
2. Observe vertical gravitational effects of subject posture (standing, sitting, supine, decline) on reconstructed 3D EIT images. The purpose of this step is to verify the ability of 3D EIT to detect regional inhomogeneities.
3. Compare 3D EIT image reconstruction results with spirometry lung volume measurements to determine whether 3D EIT can be used to measure global change in lung volume.

### 1.3 Outline

This work is divided into five main chapters. Chapter 2 describes background information and research relevant to the thesis. This provides further insight into the motivations of this work. Chapter 3 describes the 3D GREIT Reconstruction algorithm which is used in this thesis. Chapter 4 describes initial simulations that are done to set benchmarks for expected performance of different measurement patterns. In Chapter 5, a Phantom Tank experiment designed to compare measurement protocols is described and the results are presented. Finally, Chapter 6 describes the results of a human measurement experiment in which measurements are recorded during a breathing protocol, from healthy human male subjects, in four different postures.

### 1.4 Contributions

The following contributions have been made to the field of EIT during the course of the thesis.

1. Developed a novel EIT measurement performance measure 'Noise Stability', which measures the change in image quality due to the addition of noise. This parameter allows for the characterization of noise performance of 3D EIT measurement patterns in

simulations. This is useful for simulating the response of a measurement pattern in a potentially noisy *in vivo* measurement setting.

2. Developed a novel EIT image analysis parameter 'Z-Constraint', which measures the spread of a reconstructed object along the z-axis. This parameter is useful in evaluating the vertical resolution of an EIT image reconstructed onto multiple planar reconstruction layers.
3. Created a 3D EIT human measurements data set. This data set will be useful in future work done by Dr. Adler's research group to evaluate EIT algorithms and analysis techniques using *in vivo* data.
4. Evaluated and made recommendations concerning the new 3D GREIT reconstruction method. Evaluation illustrates improved vertical spatial resolution over 2D GREIT method as well as improved planar resolution. Recommendations include the variance of desired performance over reconstruction layers.
5. Used 3D GREIT method to reconstruct *in vivo* lung measurements. Achieved high correlation between 3D EIT global amplitude and spirometry lung volume change, which suggests that 3D EIT is a useful tool in monitoring lung volume changes.
6. Used functional EIT images to perform a vertical analysis of the gravitational effects of change in posture on regional lung mechanics. Determined statistically significant differences in regional lung mechanics between the decline and supine postures and the standing posture for both Planar and Zigzag Offset measurement patterns. Results were inconsistent across fEIT features.

## 2 Background

### 2.1 What is Electrical Impedance Tomography?

Electrical Impedance Tomography a method for estimating an impedance map of a body using electrical stimulation and measurement at the boundary of the body. In a typical EIT measurement system, as shown in Figure 2.1, a series of electrodes are applied to the body surface. A small AC current is applied at one pair of electrodes, and voltage is measured at the remaining electrode pairs. The current is then applied at the next electrode pair, and voltage is again measured at the remaining pairs, and this is repeated for all pairs. This measurement set represents one EIT measurement set, from which an image can be reconstructed [10].

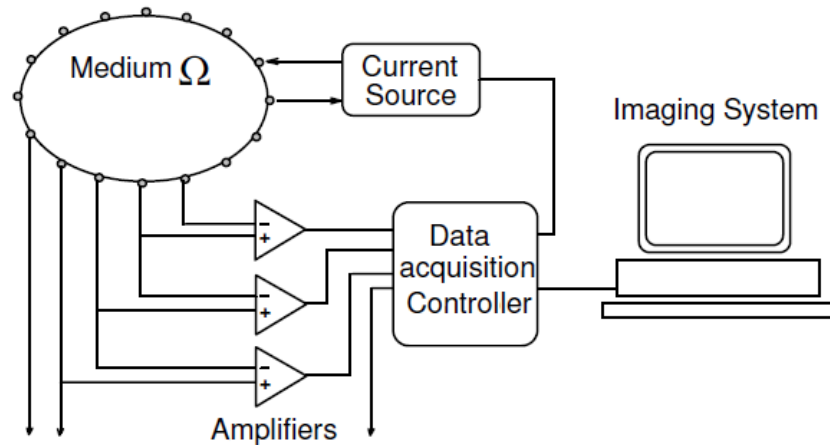


**Figure 2.1** Block Diagram of an EIT Imaging System. The system consists of a current source, data acquisition controller, and imaging system. The imaging system consists primarily of the reconstruction software. Image source [11].

The use of EIT for *in vivo* imaging is considered a non-invasive imaging technology. EIT applies high frequency, small amplitude current to the surface of the medium in order to measure the path of the electrical field through the medium. International standards set the safe current injection limit to be 100  $\mu\text{A}$  rms frequencies of  $\leq 1$  kHz and 10 mA rms for  $\geq 100$  kHz [12]. EIT measurement systems generally operate in current ranges of 1-5 mA rms, which puts it within a safe operating range for *in vivo* measurements.

## 2.2 What is the Inverse Problem?

EIT image reconstruction is a difficult problem to solve for several reasons. First, the problem is part of a field known as inverse problems. This means that we are trying to solve a problem by working backwards from the solution. The problem can be formulated using the following equation:

$$v = F(\sigma) + n \quad (1)$$

where  $v$  is the measurement set,  $F()$  characterizes the EIT system,  $\sigma$  is the impedance distribution, and  $n$  is system noise [13]. The measurement set  $v$  results from directing current through the body with impedance distribution  $\sigma$  and measuring the voltage at the boundary. For EIT, the value for  $v$  is known, or measured, and used to calculate  $\sigma$ . However, this is a difficult problem to solve, due to the fact that the EIT problem is an *ill-posed* problem. A simple reason for the ill-posedness of the problem is that there are a greater number of unknowns in the conductivity  $\sigma$  than in the measurement set  $v$ .

If Equation 1 is linearized to give  $v = A\sigma$ , then the solution for  $\sigma$  is  $\sigma = vA^{-1}$ . However, since EIT is an ill-posed problem, matrix  $A$  is difficult to invert. There are multiple solutions for  $\sigma$ , so regularization is used to find an ideal solution.

Equation 1 is then linearized as  $y = Jx + n$ , where  $y$  is the measurement set,  $x = \sigma - \sigma_r$  which represents the difference data,  $J$  is the Jacobian characterizing the EIT system, and  $n$  is again the system noise. The value  $x$  represents EIT difference imaging in which a conductivity  $\sigma$  is compared to a reference conductivity  $\sigma_r$  such that  $\sigma = \sigma_r + \Delta \sigma$ , where  $\Delta \sigma$  is a perturbation in the conductivity. The Jacobian is the sensitivity matrix, defined as  $J_{ij} = \frac{\partial y_i}{\partial x_j}$ , in which each element  $J_{ij}$  represents the change in voltage  $\partial y_i$  due to a change in conductivity  $\partial x_j$  [14].

For the one-step Gauss-Newton solver, Tikhonov Regularization is used. The solution for  $x$  derives from minimization of the following term:

$$\|y - J\hat{x}\|_{\Sigma_n^{-1}}^2 + \|x - x^0\|_{\Sigma_x^{-1}}^2 \quad (2)$$

Here,  $\Sigma_n$  is the noise covariance,  $\Sigma_x$  is the expected image covariance,  $\hat{x}$  is the calculated conductivity change estimate, and  $x^0$  is the expected conductivity change [10], which is zero for difference imaging. The first norm  $\|y - J\hat{x}\|_{\Sigma_n^{-1}}^2$  represents the error between the measurement data  $y$  and an estimate of  $y$  given by  $J\hat{x}$ . The second norm  $\|x - x^0\|_{\Sigma_x^{-1}}^2$  is the expected difference in the conductivity.

Equation 2 is solved by obtaining a solution for  $\hat{x}$ :

$$\begin{aligned}\hat{x} &= \left( J^T \frac{1}{\sigma_n^2} V^{-1} J + \frac{1}{\sigma_x^2} P^{-1} \right)^{-1} J^T \frac{1}{\sigma_n^2} V^{-1} y \\ &= (J^T V^{-1} J + \lambda^2 P^{-1})^{-1} J^T V^{-1} y\end{aligned}\quad (3)$$

where  $\lambda = \sigma_n / \sigma_x$ ,  $V = \sigma_n^2 \Sigma_n$  and  $P = \sigma_x^2 \Sigma_x$ . The term  $\sigma_n$  represents the average measurement noise amplitude and  $\sigma_x$  is the *a priori* amplitude of conductivity change  $x$ . The reconstruction matrix  $R$  is then defined as  $R = (J^T V^{-1} J + \lambda^2 P^{-1})^{-1} J^T V^{-1}$  such that  $\hat{x} = Ry$ . The term  $\lambda$  is the hyperparameter, which controls the balance between resolution and noise reduction in the image [10]. The formula for the reconstruction matrix  $R$  can be reformulated as:

$$R = PJ^T (JPJ^T + \lambda^2 V)^{-1}\quad (4)$$

This solution provides a one-step solver for the estimation of the conductivity distribution  $x$ .

### 2.3 GREIT

The GREIT algorithm (Graz consensus Reconstruction algorithm for EIT) has been developed by a group of leading experts in the field of EIT as a way of combining diversified knowledge in the field into a single formulated EIT reconstruction approach [10].

The algorithm is comprised of a 3D finite element model (FEM) with a single-ring electrode configuration using the *adjacent* current pattern, a 2D difference image reconstruction, a noise model, and a 32x32 pixel array onto specific shapes including thorax and cylindrical tank. The pixel array is the reconstruction matrix onto which images are reconstructed. The *adjacent*

current pattern uses adjacent electrodes for both current stimulation and voltage measurements.

The approach of the GREIT reconstruction algorithm is to calculate a reconstruction matrix  $R$  which achieves desired performance over the range of the FEM in terms of both image reconstruction and noise performance. In order to achieve this, a set of small training targets is simulated within the reconstruction plane. An example of a training target can be seen in Figure 2.3. Measurements are simulated for each target and a set of target images is reconstructed. The images are then compared with the desired performance. This is shown in . Weighting is applied to each image pixel to fit the reconstructed image to the desired performance figure. The reconstruction matrix is then a product of the measurements, the desired performance figure and the applied weighting.

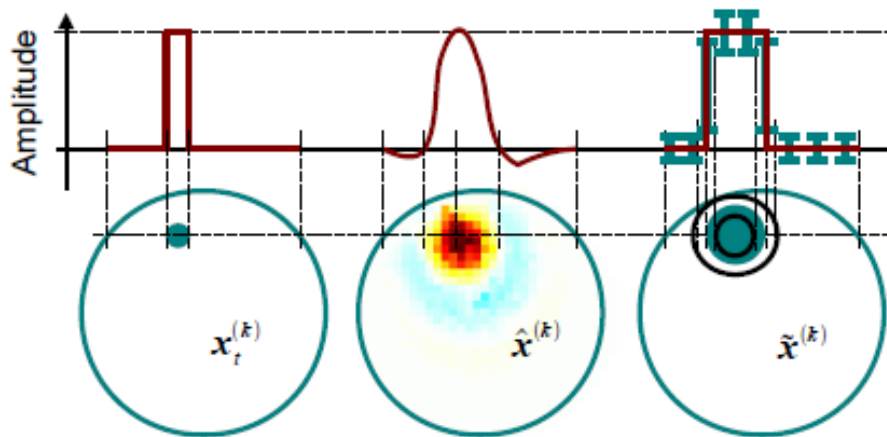


**Figure 2.2** The algorithm uses a target (*left*) and reconstructs an image (*centre*). Weighting is used in the calculation of the reconstruction matrix to match the reconstructed image to the ideal image (*right*) which has uniform performance in the centre and zero amplitude in the outer region. Image source [10].

The characteristics of the desired performance are based on five figures of merit: Amplitude, Position Error, Resolution, Shape Deformation, and Ringing. These parameters are described in . They are calculated from the reconstructed images  $\hat{x}$  as well as the quarter-max images  $\hat{x}_q$ . The quarter-max images are calculated by setting all pixel values less than  $\frac{1}{4}$  the maximum value to 0, and all values greater or equal to  $\frac{1}{4}$  the maximum to 1.

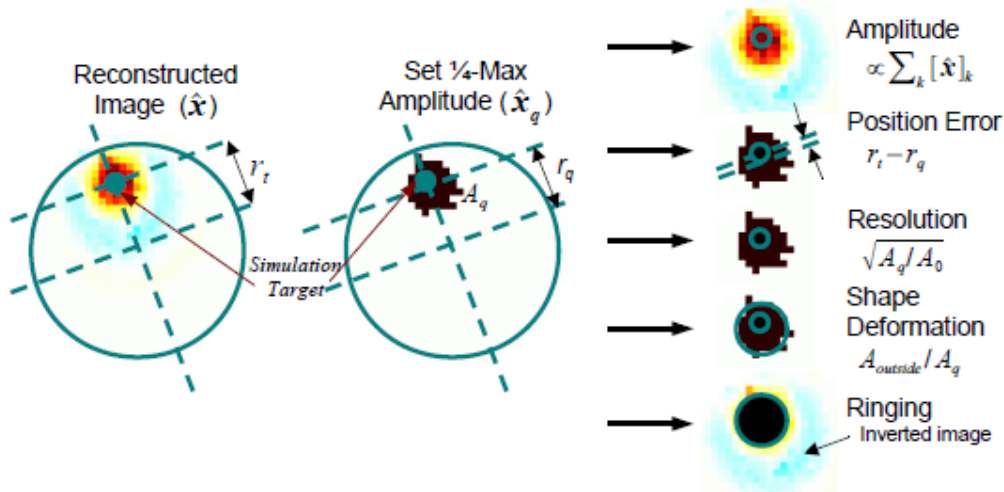


**Figure 2.3** The 5 GREIT performance figures of merit are calculated from reconstructed images  $\hat{x}$  and quarter-max images  $\hat{x}_q$ . The definitions are illustrated on the *right*. Image source [10].

The **Amplitude** parameter is defined as the ratio of the sum of the pixel values in the target region to the total pixel values of the reconstructed image  $\hat{x}$ . The desired performance is uniform Amplitude over the entire reconstruction plane.

The **Position Error** parameter is defined as the distance from the target centre to the distance to the centre of mass of the quarter-max image  $\hat{x}_q$ . The position error should be small with uniform values over area of the reconstruction plane.

The **Resolution** is defined as the ratio of the area of the quarter-max image  $\hat{x}_q$  to the area of the reconstruction plane. The resolution should be small with uniform performance over the area of the reconstruction plane.

The **Shape Deformation** is defined as the percentage of the area of  $\hat{x}_q$  that lies outside of a circle C of equal area. The circle is centred at the centre of mass of  $\hat{x}_q$  which is the mean of pixel locations in the image. The desired performance is small values and uniform response over the reconstruction plane.

The **Ringing** is an effect where regions of the reconstructed image  $\hat{x}$  have the opposite sign as the region of interest. This is calculated as the ratio of the sum of pixel values of opposite sign outside

of circle C to the sum of pixel values inside of circle C. The desired performance is small values and uniform response over the reconstruction plane.

An additional performance metric is the noise amplification or noise figure (NF) parameter. This value is given as the ratio of the output to input signal quality, or signal-to-noise ratio (SNR). The SNR of the signal is calculated as the mean of the signal divided by the standard deviation of the noise. In an EIT system the input is the measurements, and the output is the image. Therefore, NF is calculated using:

$$NF = \frac{\frac{E[\text{mean}|\hat{x}_t|]}{E[\text{std } \hat{x}_n]}}{\frac{E[\text{mean}|y_t|]}{E[\text{std } y_n]}} \quad (5)$$

The standard NF is set to 0.5 when running the algorithm.

The NF is meant to characterize the noise performance of the EIT device. The significance of the NF parameter is that it balances the performance of the algorithm between the noise performance of the image and the desired performances of the previous five figures of merit. There is an inherent trade-off between good noise performance and fidelity to the other figures of merit.

The GREIT algorithm linearizes Equation 1 to get the equation  $y = Jx + n$ . A reconstruction matrix R is sought such that  $\hat{x}^{(k)} = Ry^{(k)}$  for each training target  $k$  such that the error, given as  $\epsilon = \tilde{x}^{(k)} - \hat{x}^{(k)}$ , is small and the noise is small. The error is the difference between the reconstructed target image  $\hat{x}^{(k)}$  and the desired image  $\tilde{x}^{(k)}$ .

R is defined as minimizing the error  $\epsilon^2$  given by:

$$\epsilon^2 = \sum_k \|\tilde{x}^{(k)} - Ry^{(k)}\|_{W^{(k)}}^2 \quad (6)$$

where  $W^{(k)} = (\text{diag } w^{(k)})^2$  is a diagonal matrix giving a weighting for each measurement. The  $w^{(k)}$  term gives a weight to each pixel in the desired image  $\tilde{x}^{(k)}$  in order to reach the desired

performance. R can be solved for by expanding Equation 6, taking the derivative in terms of R, and setting  $\frac{\partial^2}{\partial R_{ij}} = 0$ .

In order to achieve both the desired image and the desired noise performance, a set of  $n_T$  target measurements  $y_t^{(k)}$  and  $n_N$  Gaussian noise samples  $y_n^{(k)}$  are generated. The target measurements are given as  $Y_t = \frac{1}{n_T} [y_t^{(1)} \dots y_t^{(n_T)}]$  and the noise samples are given as  $Y_n = \frac{1}{n_N} [y_n^{(1)} \dots y_n^{(n_N)}]$ .

The norm from Equation 6 can then be rewritten as:

$$\|[\tilde{X}_t|0] - R[Y_t|Y_n]\|_W \quad (7)$$

where  $\tilde{X}_t = \frac{1}{n_T} [\tilde{x}_t^{(1)} \dots \tilde{x}_t^{(n_T)}]$ . The term  $\tilde{X}_t$  is concatenated with 0 to give the desired performance for the noise sample vector  $Y_n$ .

The reconstruction matrix R which minimizes the norm in Equation 7 is calculated as:

$$\begin{aligned} R &= [\tilde{X}_t|0][Y_t|Y_n]^T ([Y_t|Y_n][Y_t|Y_n]^T)^{-1} \\ &= \tilde{X}_t Y_t^T (Y_t Y_t^T + Y_n Y_n^T)^{-1} \\ &= \tilde{X}_t Y_t^T (J \Sigma_x J^T + \Sigma_n)^{-1} \end{aligned} \quad (8)$$

where  $\Sigma_x$  is the expected image covariance of the target sample and  $\Sigma_n$  is the noise covariance.

The algorithm will iterate through a number of R calculations until the desired NF is reached. At the start of each iteration, the weighting is adjusted. The matrix R is then calculated, and is used to calculate a new NF using Equation 5. The weighting is then adjusted according to the new NF. This is repeated until the desired NF is achieved.

## 2.4 Electrical impedance tomography in 3D

The development of 3D EIT has been going on for close to two decades. Initially, reconstruction was complex and computationally expensive and results were poor. However, the potential benefits of having three-dimensional spatial resolution in applications such as lung and brain imaging drove the development of the 3D approach. In 1996 a paper was published by P. Metherall which described a 3D reconstruction approach having significantly improved

resolution over previous attempts [15] and having the potential for practical applications in medical imaging. The 3D algorithm produced planar spatial resolution of 10-12.5%.

Another significant development step was the development of a software suite by N. Polydorides in 2002 for reconstructing EIT images using Matlab [16]. The software was an early version of EIDORS, which is the software used for image reconstruction in this thesis. EIDORS has been developed and maintained as open source software by the EIT community, which is available at <http://eidors3d.sourceforge.net>. The version developed by Polydorides included tools for calculating three dimensional forward and inverse models in order to calculate 3D EIT reconstructions. The availability of this software provided a common set of tools for the EIT community to explore and improve upon 3D EIT algorithms.

A study published by D. R. Stephenson in 2005 looked at comparing five common 3D reconstruction algorithms using real experimental data [17]. The algorithms used were Linear Backprojection, Linear Landweber, Linear Conjugate Gradients, Linear Regularised Gauss-Newton and Non-Linear Regularised Gauss-Newton. Experimental data was recorded using the LCT2 EIT device. Four cylinders were placed upright in a tank filled with water, with 64 electrodes attached to the tank over 4 rings. The strongest performer was the Linear Conjugate Gradients algorithm, followed by the Non-Linear Regularised Gauss-Newton algorithm. However, the Linear Conjugate Gradients algorithm was calculated using both a 3D approach and a 2D approach, and results were quite similar with the 3D approach performing marginally better. The results of the study suggested that 3D EIT algorithms do have value and require further development.

## 2.5 Electrode positions & placement strategies

Most of the work that has been done with Electrical Impedance Tomography (EIT) has used a single band of electrodes to produce a 2 dimensional image. This approach limits the versatility and effectiveness of the technology as a clinical tool since it is unable to observe behavior in a volume, and also considers the path of the electric field in a plane rather than a volume. 3D EIT can provide volumetric spatial resolution and potentially improve and expand the range of EIT applications. However, there are challenges to overcome before this is possible. The main roadblock has been the added computational complexity of a 3D image reconstruction. This is

being overcome with faster processing speed as well as improvements to the image reconstruction algorithm [3]. Another challenge is the proper evaluation of the various electrode placement and stimulation patterns that are possible. This review examines the results of several studies that have explored possible 3D EIT measurement and stimulation patterns.

The selection of the stimulation and measurement pattern for 3D EIT imaging will have a strong influence on the resulting image. In a 2D measurement pattern, all stimulations and measurements are in a single plane. With a 3D measurement pattern there can be a mix of horizontal, vertical, and diagonal measurements. The combination of measurement orientations will affect the spatial resolution and quality in the X-Y plane and along the Z-axis. It can be assumed that more horizontal measurements will improve resolution in the X-Y plane, whereas more vertical measurements improved resolution along the Z-axis. The patterns explored in this study range from mostly horizontal to mostly vertical measurements.

There have been several studies involving the analysis of measurement protocols for 3D EIT. The approach depends highly on the application or region being imaged. As this work is primarily interested in thoracic measurements, exploration was limited to studies involving this region.

#### 2.5.1 Electrode Placement Configurations for 3D EIT

In chapter 6 of the thesis by B. Graham, several electrode placement configurations for 3D EIT are described [8]. These configurations are based around a 16 electrode EIT system. The basic layout consists of 2 concentric rings placed around the medium to be imaged, whether it is a tank or thorax. The electrodes in the two rings can be lined up or offset by half the horizontal electrode separation.

The 3D patterns described below are taken from work done by B. Graham. The patterns are Planar, Planar-Offset, Planar-Opposite, Zigzag, Zigzag-Offset, Zigzag-Opposite, and Square. The patterns are illustrated in Figure 2.5 and Figure 2.6. These patterns are specific to a 2 layer, 16 electrode EIT system having 8 electrodes per layer. Figure 2.4 shows the two different electrode ring alignment strategies, 'aligned' and 'offset'. The offset has the electrodes of the second layer offset from the first layer by half the inter-electrode distance.

## 2 Electrode Arrangements

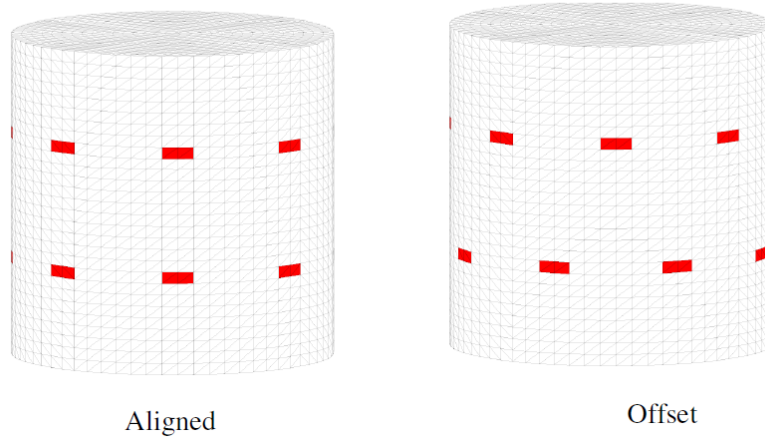
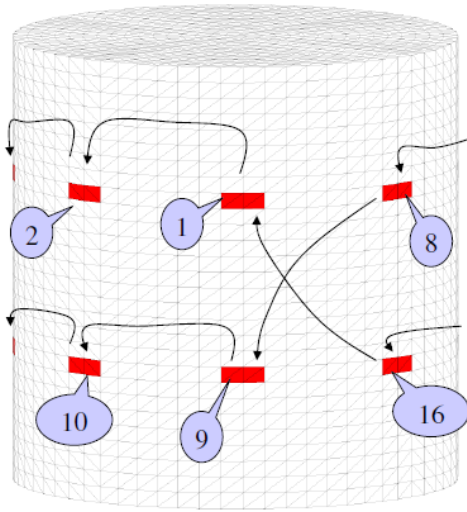


**Figure 2.4** Diagram of electrode placement patterns for Aligned and Offset electrode patterns. Image source [18].

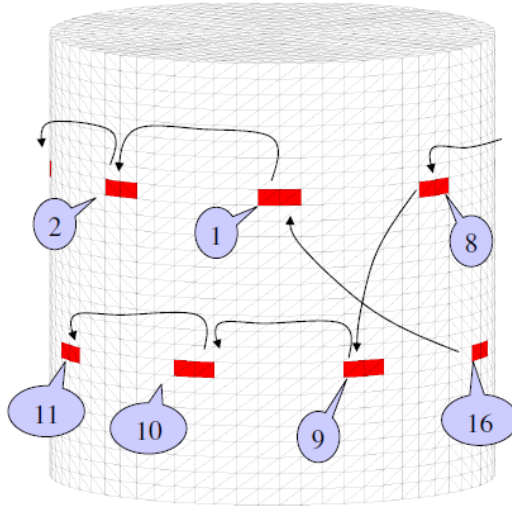
Each pattern uses the *adjacent* current protocol, in which electrodes 1 and 2 are used to apply the current and the subsequent pairs (3-4, 4-5, etc.) are used to measure voltages. Next current is applied using electrodes 2 and 3 and voltage measurements are taken on the remaining pairs. This results in 208 measurements for one EIT measurement frame which is used to produce an image. Both the number of electrodes and the separation between the stimulation and measurement electrode pairs can be varied (eg. e1-e2 for stimulation, e2-e6, e3-e7, etc. for measurements). However, one of the goals of this study is to verify simulated results with real data. The equipment being used in this study is limited to 16 electrodes and the *adjacent* current pattern, where the electrode separation is fixed at 1. Therefore, the simulations are performed using these limits.

In the work by B. Graham, the seven patterns were analyzed using simulations in EIDORS. A 3D FEM was created to match the geometry of an available phantom tank setup. Image reconstruction was performed using one-step linearized reconstruction with a Nodal Jacobian [14] inverse solver algorithm to reduce the complexity of the 3D calculation problem.

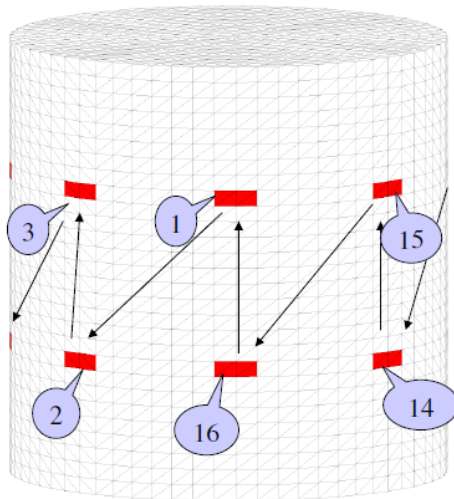
Planar



Planar-Offset



Zigzag



Zigzag-Offset

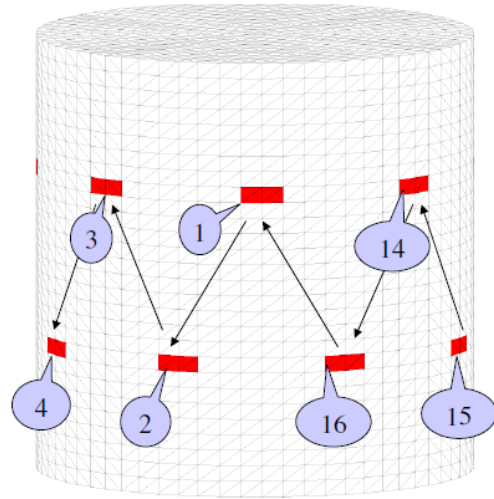
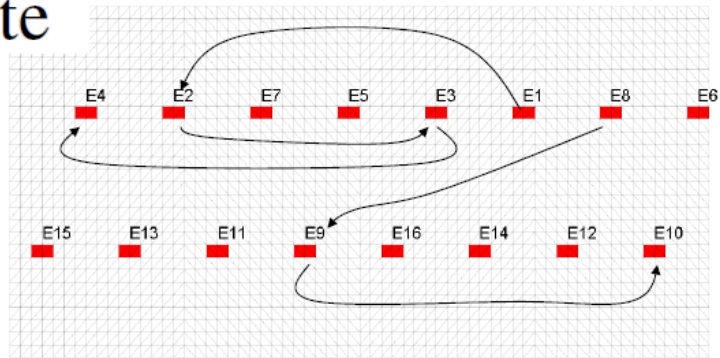
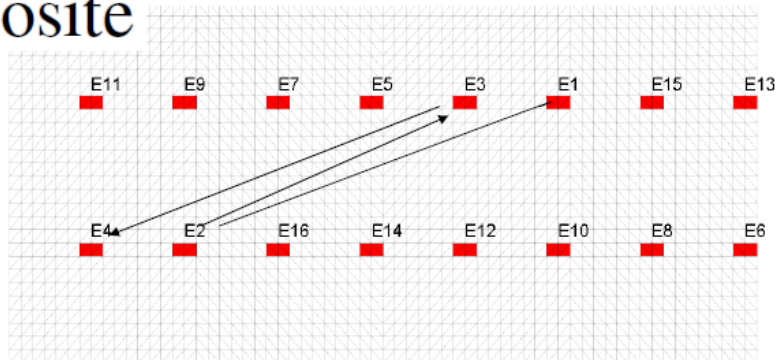


**Figure 2.5** Electrode placement patterns 1-4 for 2 ring arrangement. The arrangement is based on a 16 electrode EIT device. Image source [18].

# Planar-Opposite



# ZigZag-Opposite



# Square

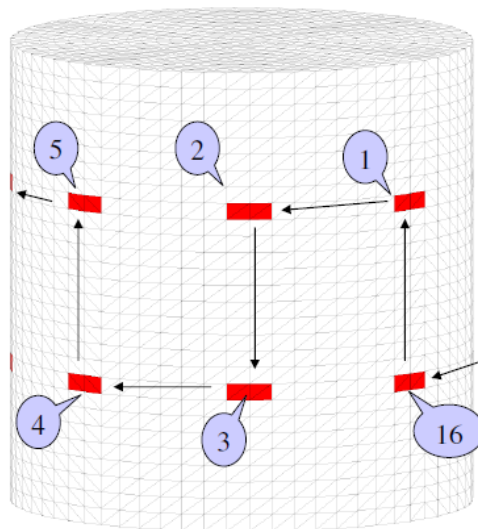


**Figure 2.6** Electrode placement patterns 5-7 for 2 ring arrangement. The arrangement is based on a 16 electrode EIT device. Image source [18].

The results are analyzed based on a number of criteria including SNR, Resolution, Radial Position Error, Vertical Position Error, Image Magnitude, Qualitative Evaluation, Immunity to Noise, and Electrode Placement Errors (both inter-ring offset error and plane separation error).

Under the different conditions, several conclusions are made. First, both Opposite patterns are highly susceptible to noise and not recommended. Second, the Zigzag pattern performs poorly under noisy conditions. Third, Zigzag-Offset is susceptible to Offset Error. Fourth, the Square pattern performs poorly for Vertical Position Error, noisy conditions, and artefacts. Fifth, Planar and Planar-Offset patterns are most robust to noise and systematic electrode placement errors and perform equally or better than other patterns in the region of interest (ROI). Sixth, the Planar pattern provides the largest image energy in the central regions, and is the most robust to noise.

In general, different patterns show different performance levels under different tests. The final recommendation of this work are that the Planar and Planar-Offset patterns are the best overall performers, the Planar being slightly stronger.

### 2.5.2 Distinguishability

The seven 3D patterns described above were explored in more detail in [19] by Y. Mamatjan. First, the stimulation and measurement patterns are varied by adjusting the electrode pair separation. Second, the criterion of 'Distinguishability', described in [13], is applied to analyze the pattern performance. Distinguishability uses a hypothesis-testing model where the null-hypothesis is that the impedance change estimate between two conductivity distributions is 0. Finally, simulations are performed by first moving a target to different radial positions both on- and off-plane, and second by creating a vertical cylinder inside of a vertical hollow cylinder.

Results show that Zigzag, Square, and Planar-Interleaved (modified –Opposite) with electrode separation of 8 provide good performance, and Zigzag-Interleaved provides best overall performance.

A 2D exploration of electrode stimulation and measurement pair separation has been done by Y. Mamatjan in [7]. This work again used the Distinguishability criterion, and uses both simulation and phantom tank results. The pair separation refers to the number of electrodes separating a

pair of stimulation or measurement electrodes. The results suggest that the Distinguishability performance increases as the angle between electrodes increased, and that the *adjacent* current pattern should not be used for a basic 2D setup. The recommended electrode separation is one less than opposite, which would be a separation of 7 electrodes in a 1-ring, 16 electrode system.

Besides the work done by B. Graham and Y. Matmatjan described above, little focus has been put on the systematic evaluation of measurement patterns for 3D EIT. Furthermore, the problem of optimizing electrode placement and measurement patterns for imaging human subjects has not been explored. The main objective for this thesis is to evaluate 3D measurement patterns in order to better understand the effects of measurement strategy on image quality and establish a methodology for characterizing measurement pattern performance.

## 2.6 EIT in Medical Applications

Common EIT medical applications focus on physiological processes involving contrasting or changing conductivity. In cases involving static conductivity distributions, absolute imaging is used. This approach consists of reconstructing a single measurement frame or an averaged set of measurement frames to produce an image. The most common example of this is cancer detection, such as breast cancer, in which the cancerous tissue has a different conductivity than the healthy tissue.

For processes with changing conductivity distributions, difference imaging is used. In this technique, time series measurements are compared to a reference measurement in order to measure the change in the conductivity distribution. This is used in applications such as lung, heart, and brain imaging. The lungs will expand and contract during the breathing cycle, the heart will change as blood is pumped through the four chambers and out through the aortas, and the blood flow in the brain changes according to brain activity. These changes are well-suited for EIT difference imaging.

### 2.6.1 EIT and Lung Imaging

There are a number of medical procedures where EIT as a safe, portable, real-time imaging system fills a need for which high resolution systems are not suited. An example of this is during

lung ventilation of an injured lung, where EIT can be used to provide real-time images of the lungs during. The pressure applied during ventilation needs to be high enough to promote lung recovery, but not so high that the healthy lung tissue is damaged. EIT is capable of providing real-time feedback required for physicians to properly manage the ventilation system.

This application was explored in an *in vivo* study in [4]. The purpose of this work was to monitor regional atelectasis and overdistension in the lungs during a ventilation procedure using EIT. Atelectasis is the improper expansion of part of all of the lungs, and overdistension is injury to the lungs due to overexpansion. The study monitored 10 subjects under the age of 18 having acute lung injury for less than 72 hours. EIT images were recorded while the patients underwent a ventilation procedure consisting of lung recruitment steps.

This study showed that EIT could be used to determine regions of atelectasis and overdistension in the lungs during a ventilation procedure. The EIT results were used to determine several key parameters of lung mechanics during the lung recruitment procedure. First, reversal of atelectasis preceded improvements in gas exchange, which suggests the validity of the parameterization approach. Second, lung recruitment of dependent regions (those most influenced by gravity) involved simultaneous overdistention in non-dependent regions. Finally, subject response was greater in subjects with higher atelectasis. Subjects with lower atelectasis had lower lung recruitment and higher overdistension. These findings indicate that EIT would be useful as a complimentary tool which provides real-time feedback to optimize ventilation settings.

There are clinical lung imaging devices available. A device such as the PulmoVista500 by Draeger, shown in Figure 2.7, uses a 16 electrode single ring belt and produces a 2D image of a patient's lungs in real-time [20]. A physician is able to see inhomogeneities in lung functionality for a cross-section of the lungs. This is crucial for monitoring lung function during medical procedures such as ventilation, where applying pressure at too high of a level can damage the lungs, and pressures set too low will prevent proper lung recruitment [20].



**Figure 2.7** Clinical bedside monitoring EIT device: PulmoVista 500 by Draeger. Image displays electrode belt around thorax of patient and screen displaying real-time EIT images. Image source [<http://campaigns.draeger.com/pulmovista500>].

### 2.6.2 EIT and Heart Imaging

The use of EIT for cardio-related imaging is more difficult than for lung imaging. In the thorax, the expansion and contraction of the lungs dominates the conductivity changes, making the weaker cardio-related signal difficult to extract. A great deal of research has been done in this area, as documented in [21]. This overview outlines a number of ways that have been employed to extract the cardiac signal. These include frequency domain filtering, ECG gating, contrast agents, and principle component analysis. However, this field remains in the research domain and has not yet entered clinical use.

### 2.6.3 EIT and Brain Imaging

A great deal of research has been done on using EIT to image brain activity. EIT imaging of the brain typically uses 3D image reconstruction. There are multiple applications where EIT of the brain can provide useful information. Several examples are events such as seizures and strokes. A study done by A. P. Bagshaw [22] built on work done in a previous study [23] in which EIT scalp measurements were taken during a subject response to various external stimuli. In the original study, reproducible impedance changes of  $\sim 0.5\%$  were seen. The work done by Bagshaw improved the results by improving the reconstruction algorithm. The new algorithm was based on the finite element method and incorporated a more accurate geometry and extracerebral layers into the reconstruction. The results saw significant improvement over the original study.

EIT measurements were also taken from two patients during seizures. The images agreed with the ictal activity from simultaneous EEG data. The results are encouraging for the use of EIT in brain imaging applications.

A study done by Y. Mamatjan [24] analyzed the effect of electrode placement strategy as well as stimulation and measurement patterns for the purpose of cerebral edema and stroke detection. The work aimed to use the distinguishability measure described in [13] to determine optimal measurement strategies. This involved first running simulations on a hemispherical phantom FEM and evaluating a number of electrode configurations. These included 1 ring of 16 electrodes, 2 rings of equal electrodes (8 each), 3 rings of electrodes, and a 10-20 placement system. The 2 ring system used the 7 electrode patterns developed by B. Graham [8] as described in Section 2.5.1. The 10-20 placement system placed the electrodes in a spread out fashion to cover the surface of the phantom. The electrode ordering was set as a spiral around the x-axis in one configuration and around the z-axis in another. For each pattern, the electrode pair separation was varied as well from  $\Delta 11$  (*adjacent*) to  $\Delta 88$ .

The 10-20 system had the highest distinguishability. All patterns showed maximum sensitivity towards the edges. Measurements with the z-spiral 10-20 placement system were carried out on an experimental phantom made from a plastic hemisphere. The distinguishability results matched well with the simulations results. The findings of this study are very relevant for researchers using EIT to image the brain. Also, the experimental method provides a useful framework for the analysis of electrode placement patterns and stimulation/measurement patterns for a 3D system.

#### 2.6.4 EIT and Breast Cancer Detection

Breast cancer detection is an application for which absolute EIT imaging is well suited. Absolute imaging reconstructs each data frame individually, rather than comparing to a reference measurement as in applications involving dynamic processes. Cancer detection is a static process, and is therefore restricted to absolute imaging. The cancerous tissue has different conductivity than the healthy tissue, which makes it possible to detect using EIT. Time-averaging can be used to further reduce noise in order to improve image quality.

A 3D EIT device was developed in 2000 to detect breast cancer [25]. The device consisted of a 256 electrode array along with a designated stimulation electrode and designated measurement electrode. Due to the large number of measurements, a single data frame took ~20s to collect. The image was reconstructed using weighted back projection. During an *in vivo* trial the device performed with 86% accuracy including 14/21 detection of focal abnormalities (cancer) as well as 4 cases of abnormal conductivity distributions considered a positive detection.

A larger study [26] was conducted consisting of an *in vivo* trial on 117 female patients. The subjects included healthy patients and patients with mastopathy, benign tumours, or breast cancer. The results of the breast cancer test showed an 87.4% efficiency with 12.6% false positives, which is a slight improvement from the previous study. The study also noted that the EIT device offered a safe, comfortable, and fast method for breast cancer detection.

Breast cancer detection devices based on EIT are also available for clinical use. The MEIK electroimpedance mammograph was used in the two studies mentioned above. The device uses a circular array of 256 electrodes to image the conductivity over the breast [26]. The T-SCAN device is another clinically available device [27]. It consists of an 8x8 or 16x16 electrode array. In this case, as with many EIT applications, the device is used as a complimentary tool to enhance standard procedures rather than as a standalone system.

## 2.7 EIT vs. Lung Mechanics

One of the primary goals of this thesis is to extract useful information from *in vivo* lung measurements using EIT imaging. This section looks at several relevant studies which deal specifically with the use of EIT during *in vivo* experiments. The material covers a range of topics pertinent to this thesis, including the analysis of electrode placement during *in vivo* EIT measurements, a comparison of EIT to spirometry for lung functionality testing, and the measuring of gravitational effects on lung mechanics using EIT imaging.

### 2.7.1 Electrode Plane Height

There are many considerations to be made when using EIT to measure lung properties in human subjects. One key parameter is the placement of the electrode ring(s). Different studies place the

electrode plane at different vertical locations on the thorax. Several studies using a 2D electrode arrangement have placed the electrode plane at the fifth or sixth intercostal space, along with a reference electrode against the abdomen [5], [28].

In [29], the effects of electrode plane location were explored. A single electrode ring was varied between 2 cm and 7 cm above the xiphoid process. This location is the point in the chest where the lowest joining ribs meet. The results showed best results between 4 and 5 cm above the xiphoid process.

### 2.7.2 Cystic Fibrosis

One application where EIT could potentially have application is in the monitoring of lung mechanics in Cystic Fibrosis (CF) patients. CF is a disease which causes the slow degeneration of lung health which leads to increased lung resistivity. Standard tests for monitoring CF include spirometry measurements, which can capture global lung parameters but not regional ones. In [5], both spirometry and EIT were measured on subjects, both healthy and having CF. The data set was analyzed to determine several lung parameters including global inhomogeneity (GI) index. The GI score was calculated as the 25-75 Maximum Expiratory Flow (MEF) ratio during a vital capacity breathing protocol. While the difference between the lungs of the CF and healthy patients was not always clear directly from the images, the GI score was found to be a strong indicator of typical CF lung mechanics.

### 2.7.3 EIT vs. Posture/Gravity

There have been several papers reporting evidence supporting the capture of regional lung behavior using EIT. In [30], lung density estimates were calculated based on 2D EIT readings measured at the 3<sup>rd</sup>, 4<sup>th</sup>, 5<sup>th</sup>, and 6<sup>th</sup> intercostal spaces. Measurements were taken with subjects in various postures. Results showed that lung density at the 6<sup>th</sup> intercostal space was generally different from the density at other levels, and that the lung densities at the 4<sup>th</sup> and 5<sup>th</sup> intercostal spaces in male subjects were independent of posture. Finally, the paper suggests the possibility of a gravitational effect on lung density.

EIT has also been shown to capture the regional effects of gravity on lung mechanics. In [28], EIT measurements were taken on subjects during parabolic flights, which provided periods of

microgravity (0G), normogravity (1G), and hypergravity (2G). Patients were in both supine and right lateral postures in order to observe the gravitational effects in the transverse thoracic plane.

The study used functional EIT (fEIT) images to analyze mechanical properties of the lungs. Lung ventilation was calculated as the end-inspiration to end-expiration amplitude of relative impedance change. Regional shift in lung volume was calculated as the change in local end-expiration values of relative impedance change (2G or 0G vs. 1G). Finally, curvilinearity of lung emptying was determined by calculating the 2<sup>nd</sup> degree coefficient of the polynomial fit of pixel value over time.

Results showed several gravitational effects on regional lung ventilation. First, there was a gravitational effect on regional forced residual capacity, with rapid lung volume redistribution during gravity transitions. Second, microgravity had the most homogeneous functional residual capacity (FRC). FRC is the volume of air remaining in the lungs upon a relaxed exhalation. During vital capacity (VC) and forced vital capacity (FVC) in right lateral posture, the decrease in lung volume on expiration was larger in the right lung region. VC is the volume from maximum exhalation to maximum inhalation, and FVC is the exhalation of the VC volume at maximum force. Finally, significant non-linearity of lung emptying was determined at normo- and hypergravity but none at microgravity.

## 3 Reconstruction Approach

### 3.1 3D GREIT Method

The 3D reconstruction approach is an extension of the 2D GREIT method [10], which is described in the Background chapter. The 3D method was developed by Bartłomiej Grychtol, and has been presented in [31] at the 2014 EIT Conference. This section describes the new algorithm in greater detail.

The 3D GREIT method builds on the framework of the original 2D method. Several steps have been taken in key areas of the algorithm to create an inverse model with a one-step reconstruction matrix calculation. The one-step calculation leads to an interdependency between the layers of the reconstruction model in order to improve image quality. The changes to convert the algorithm to a 3D approach include:

1. The creation of a 3D target set.
2. The building of a 3D reconstruction model.
3. The calculation of a 3D reconstruction matrix.

The GREIT method consists of a forward model, a noise model, and a set of desired performance metrics. The forward model in this work is a 3D cylindrical FEM using 16 circular electrodes. The purpose of the forward model is to describe the system that is being measured in order to generate simulated measurements. The forward model includes a 3D mesh, an electrode model, and a conductivity distribution. The term ‘forward’ refers to the mathematical problem of using a known parameter of a system to calculate an effect or measurement.

Conversely, the inverse model is used to calculate the conductivity of the medium being measured from the EIT measurements. In this case the problem is reversed as the effect or measurement is used to determine the characteristics of the system. In EIT this is classified as an ill-posed problem, since the measurement information is limited and there will be multiple solutions to the problem.

The 2D algorithm reconstructs an image onto a 2D plane. In the 3D method, the image is reconstructed onto multiple 2D planes perpendicular to the z-axis. These reconstruction layers are selected heuristically in order to provide proper coverage of the region of interest, depending on the application, with consideration of memory limits and speed requirements. The layer selection has an effect on the image quality due to changes in layer location and separation. This effect is described in the *3D vs. 2D GREIT* section below. Inadequate coverage can result in off-plane effects and lower resolution.

The set of training targets is then extended to cover all reconstruction layers. This step multiplies the size of the training measurements by the number of layers, and extends the GREIT training algorithm to take all layers into account. All layers will therefore be incorporated into the optimization of the reconstructed image to adhere to the desired performance.

Next the 3D method creates a multi-level reconstruction model. The 2D reconstruction model consists of a single plane. In the 3D algorithm, the reconstruction model is comprised of a set of 2D planes representing the target planes.

The final significant change is in the calculation of the reconstruction matrix. The formula for the reconstruction matrix  $R$  is given in Equation 8, given as  $R = \tilde{X}_t Y_t^T (J \Sigma_x J^T + \Sigma_n)^{-1}$ .

It can be shown that the term  $J \Sigma_x J^T$  is equivalent to  $Y_t Y_t^T$  which is due to the fact that the training target measurements  $Y_t$  are taken from a distribution characterized by  $J$  and  $\Sigma_x$ . The signal  $Y_t$  is the set of simulated target measurements, and is taken from distribution  $P = \sigma_x^2 \Sigma_x$  where  $\Sigma_x$  is the expected image covariance and  $\sigma_x$  is the *a priori* amplitude of the conductivity change. So  $J \Sigma_x J^T = J P J^T / \sigma_x^2$ .  $J P J^T$  represents the signals for each  $x$ , or  $J$ , over the likelihood of  $x$ , which is  $P$ . Because  $P$  is positive definite, it can be written as  $P^{1/2} P^{1/2}$  so that  $Y = J P^{1/2}$  and  $Y^T = P^{1/2} J$ .

The implementation of Equation 8 is therefore given by following equation:

$$R = \tilde{X}_t Y_t^T (Y_t Y_t^T + \Sigma_n)^{-1} \quad (9)$$

where  $\tilde{X}_t$  is the set of desired images based on the target set,  $Y_t$  is the set of simulated target difference measurements, and  $\Sigma_n$  is the noise covariance term.

For the 3D GREIT method, the parameters are extended to cover the multiple target planes. Now, the number of targets  $n_T = [(\text{targets per layer}) \times (\text{number of layers})]$ .

The set of desired images  $\tilde{X}_i$  is determined by calculating the Point Spread Function (PSF) for each target using the desired performance metrics. This gives a matrix  $A_i = \text{PSF}_i$  matrix for each layer. Summing the PSF for all results in a matrix  $D_{i,j} = A_i$  of dimensions  $n_P \times n_T$ , where  $n_P$  is the number of conductivity elements per image and  $n_T$  is the number of targets.

$$D = \begin{bmatrix} A_1 & 0 & \dots & 0 \\ 0 & A_2 & \dots & 0 \\ \dots & \dots & \dots & \dots \\ 0 & 0 & \dots & A_L \end{bmatrix} \quad (10)$$

where  $L$  is the number of layers in the system. It should be noted that this approach assumes that the target radius is smaller than the target plane separation.

The noise covariance  $\Sigma_n$  is calculated using the weight  $w$  such that  $\Sigma_n = (w * \text{mean}(Y))^{2*} I$  where  $I$  is an  $n_V \times n_V$  matrix. The term  $w$  represents the weighting assigned to each measurement and is set with an initial guess. In this algorithm the weighting is constant for each measurement.

The algorithm is designed to adjust weight  $w$  in order to satisfy the desired noise figure (NF), which is described in Section 2.3. The calculation of the reconstruction matrix  $R$  remains a one-step problem. This allows for the simultaneous consideration of the target layers and thereby accounts for the interdependency between layers. This leads to the improved spatial resolution on the  $z$ -axis and reduces the influence of off-plane objects. This is further discussed in the next section.

## 3.2 3D GREIT vs. 2D GREIT

### 3.2.1 Method

The proposed 3D GREIT method is compared to the 2D GREIT method to examine the effects of off-plane targets on image quality. The forward model is built using a cylindrical finite element model (FEM) mesh using 35 089 elements. The 2D model includes one ring of 16 circular electrodes and the 3D model uses 2 rings of 16 electrodes. Measurements are simulated using

the *adjacent* current pattern. The 2D method solves each plane individually while the 3D method uses a single reconstruction matrix. Simulations are done using EIDORS v3.7.1, an open-source software package developed by EIT experts available at <http://eidors3d.sourceforge.net>.

### 3.2.2 Results

The reconstructed images, overlaid onto the FEM mesh, are shown in Figure 3.1. The 2D GREIT image shows strong off-plane influence. For each slice, the image extends towards the off-plane sphere, resulting in a wide column. The 3D GREIT image is better constrained to the object regions for both the on- and off-plane objects.

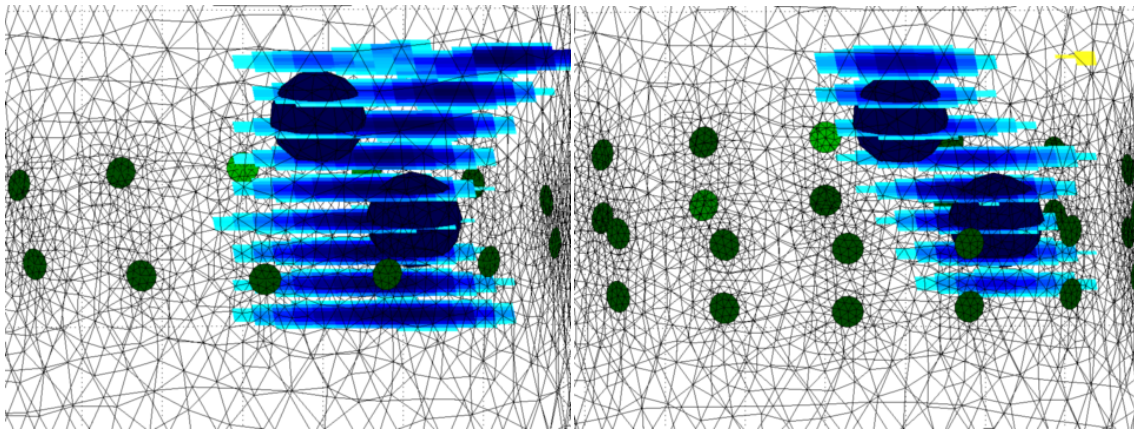


**Figure 3.1** Reconstructed images using 2D GREIT method (left) and 3D GREIT method (right). Images generated using EIDORS.

The 3D GREIT method provides better resolution and lower position error, as illustrated in Figure 3.2. This suggests that the 3D method has improved immunity to off-plane effects while also providing useful information concerning regions outside the electrode planes.

Although the 2D GREIT method allows the specification of the position of the desired image plane, since a single image must explain all the data, it necessarily conflates the two targets. By simultaneously reconstructing images at multiple planes, 3D GREIT allows to distinguish changes occurring at different levels, resulting in reduced off-plane influence. Consequently, the selection of the target planes has high significance in the 3D GREIT method.

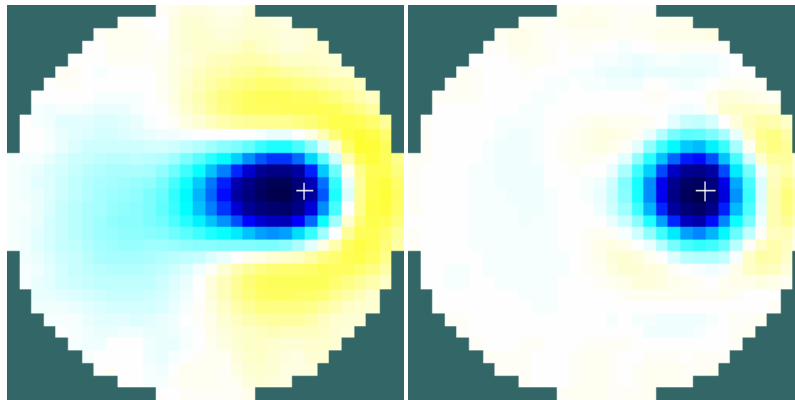


**Figure 3.2** Centre image slice from 2D GREIT method (left) and 3D GREIT method (right). Images generated using EIDORS. White hashmarks indicate the centre of the cube being imaged.

These results demonstrate the reduction of off-plane effects and allows for the imaging of off-plane objects, while improving resolution and position error. However, the 3D GREIT reconstruction method leads to interdependency between the layers used in the inverse model. Therefore the selection of the reconstruction layers requires careful consideration. The images below demonstrate some of the effects that can be observed. The electrode plane separation is 0.4 cm with the centre plane at 3.0 cm, and the reconstruction layer separation is 0.2 cm.

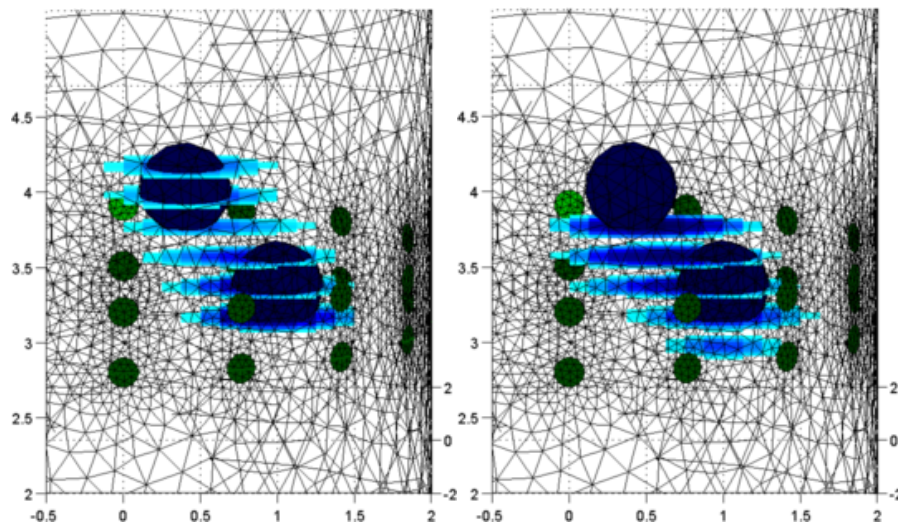


**Figure 3.3** 3D GREIT images using planes a)  $z=[2.8-3.8]$  and b)  $z=[2.6-3.4]$ . Units in cm.

In Figure 3.3, the left image shows a reconstructed image with proper coverage of both objects. The right image only has partial coverage of the upper target. The difference in coverage leads

to a much higher amplitude in the space under the upper object in the right image. This indicates that the upper sphere is having a stronger influence on the plane below it. By setting proper coverage of the upper sphere, as in the left image, the conductivity in the region of the upper sphere is considered in the reconstruction matrix and the upper sphere's influence on lower planes is reduced.

## 4 Simulations

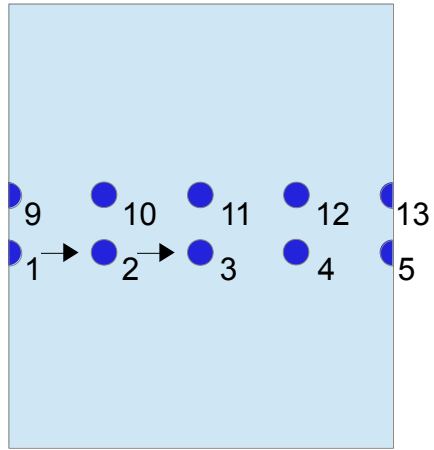
The purpose of this chapter is to establish a baseline for the performance of different measurement protocols under the conditions of impedance error and electrode placement error. The seven 3D measurement protocols described by B. Graham [8] and described below are examined under these conditions in order to determine their performance in terms of the GREIT parameters, which have been described in Section 2.3, as well as a Noise Stability measure which is described below in Section 4.3.2.

The goal is to work towards a selection of the three most suitable patterns to be used for the human measurements experiment. The suitability is determined based on the noise performance in the simulations and on the quality of reconstructed images of each pattern in the Tank Phantom experiment described in Chapter 5. The 5 GREIT parameters are used to analyze the pattern performance, as well as additional relevant parameters.

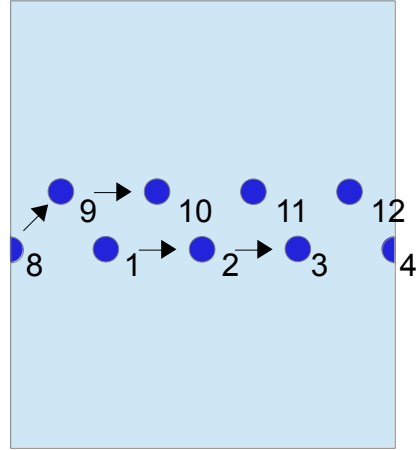
The Simulations chapter attempts to characterize the performance of the patterns under the two aforementioned noise conditions. The Tank Phantom chapter then measures the performance of the 7 3D patterns using real data from an experimental apparatus, which is then compared to the Simulations chapter results. From this analysis, three patterns are selected to be used in the Human Measurements experiment.

### 4.1 EIT Measurement Patterns

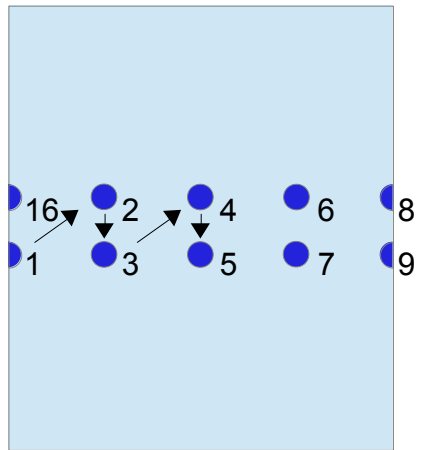
The seven EIT measurement patterns proposed by B. Graham, which have been described in Section 2.5.1, are shown below in Figure 4.1 and Figure 4.2. These patterns represent a wide range of electrode pair coverage, including horizontal, vertical, diagonal and cross-plane electrode pairs. In practice, the patterns are achieved by moving the numbered electrodes to fit the patterns described in the figures and applying the *adjacent* current pattern. This current pattern uses adjacent stimulation and measurement electrodes. The current pattern will then follow the numbering for each measurement pattern shown in the figures.



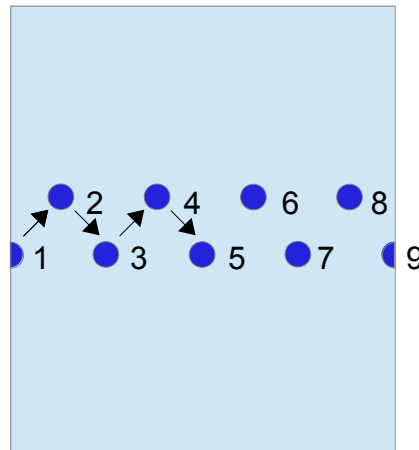
PLANAR



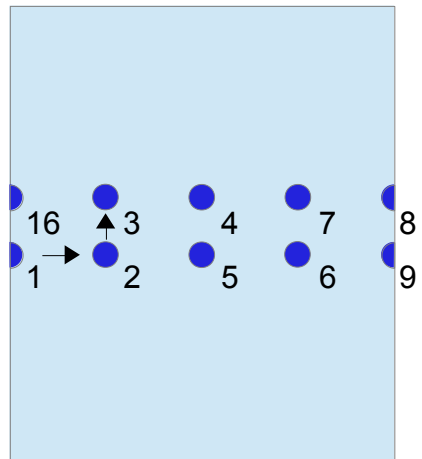
PLANAR OFFSET



ZIGZAG

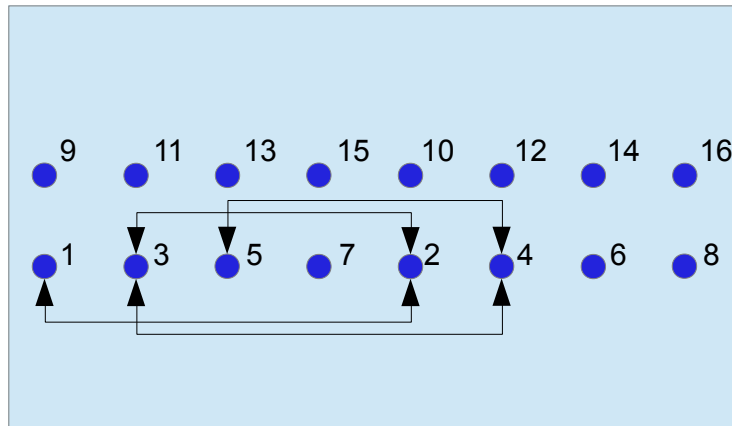


ZIGZAG OFFSET

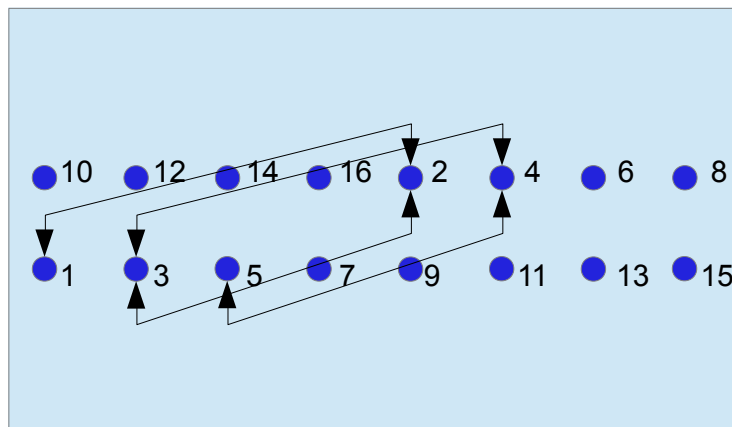


SQUARE

Figure 4.1 Five out of seven EIT measurement patterns described by B. Graham [8].



PLANAR OPPOSITE



ZIGZAG OPPOSITE

**Figure 4.2** Two out of seven EIT measurement patterns described by B. Graham [8].

## 4.2 Simulation Models

The simulation approach consists of a 3D finite element model (FEM), a stimulation pattern, an inverse model calculated using the 3D GREIT Method, and the final data analysis. The simulations are run using the EIDORS v3.7.1 software package. EIDORS is an open-source software package available at <http://eidors3d.sourceforge.net>. The software has been developed by members of the EIT community.

### 4.2.1 Cylindrical Model

Two FEM meshes are created in EIDORS for both simulated and experimental image reconstruction. The first model simulates a tank apparatus, similar to the one used in the Tank

Phantom experiment described in Chapter 5. A cylindrical mesh, shown in Figure 4.3 is created of dimensions matching the physical tank with electrodes arranged around the centre. The cylindrical FEM is built using 49 244 elements, and uses 2 rings of 8 circular electrodes to simulate 3D measurements. EIDORS uses the open source Netgen software package, available at <http://sourceforge.net/projects/netegen-mesher>, to generate the 3D mesh. The model is designed to increase mesh density close to the electrodes.

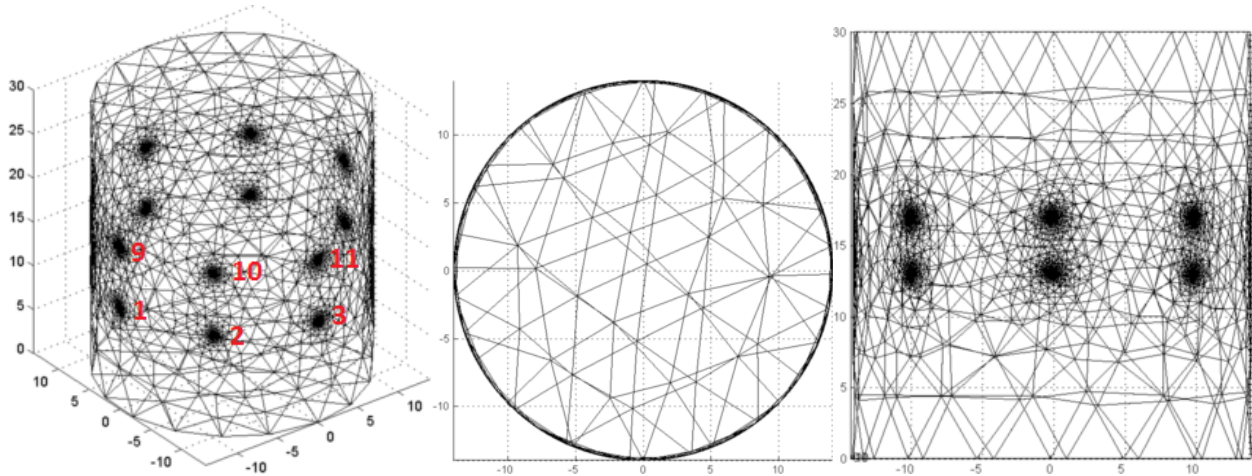


**Figure 4.3** A cylindrical FEM model generated by EIDORS from perspective, top, and side views. The model includes 2 rings of 8 electrodes. Electrodes are numbered 1-16 and are re-arranged to match the 7 measurement patterns. The mesh density is higher close to the electrodes.

#### 4.2.2 Thorax Model

The second model simulates an adult human male thorax. The model is available in EIDORS v3.7.1, and is described in the paper presenting the GREIT method [10]. The 3D FEM model is created using CT scans of a human thorax to determine the physical lung and surface boundaries, and is shown in Figure 4.4. The model uses 21 426 elements, and has been modified to use 2 rows of 8 circular electrodes. This model is used in the reconstruction of human EIT data in the Chapter 6.

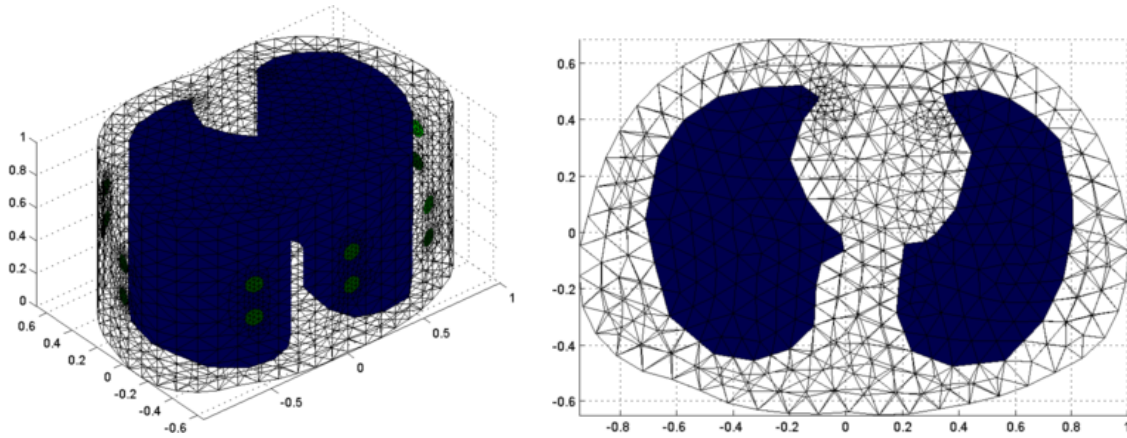


**Figure 4.4** Thorax Model generated by EIDORS. The model consists of two lung regions of lower conductivity. 2 rows of 8 electrodes are included. The lung dimensions are from [10]. Electrodes are numbered 1-16 and are re-arranged to match the 7 measurement patterns.

For both forward models, the electrode stimulation pattern is set to the *adjacent* current pattern, and the electrodes are then rearranged in the simulation to fit the desired measurement pattern. The offset patterns include a shift in location of the upper row of the electrodes by 45 degrees. The *adjacent* current pattern sets the stimulation electrode pair and measurement electrode pairs to a separation of 1. The stimulation pattern could also be altered manually without moving the electrodes to generate the different measurement patterns. However, the EIT device that is used in subsequent chapters is limited to the *adjacent* current pattern so the simulations are designed to match.

### 4.3 Analysis Approach

The first set of simulations looks at the performance of the seven measurement patterns under two conditions: electrode placement error and electrode impedance error, which are described below. The results are analyzed using two approaches. The first approach looks at the overall image quality, which is quantified using the five GREIT parameters. The second approach describes the stability of the pattern when noise is applied, and is quantified using the Noise Stability measure which is defined below in Section 4.3.2.

#### 4.3.1 GREIT Parameters

The GREIT reconstruction method includes five performance metrics: **Amplitude**, **Position Error**, **Resolution**, **Shape Deformation**, and **Ringing**. The parameter calculations are described in Figure

4.5. These parameters have been described in the Background chapter in Section 2.2, and are defined by the GREIT algorithm [10]. The performance metrics are used in the GREIT algorithm to describe the desired characteristics of a reconstructed target image, which is used in the calculation of the reconstruction matrix.

The weighting of the performance metrics in the GREIT algorithm can be adjusted to favour specific performance metrics if desired. In the standard application, the desired performance characteristic for AR is to have a uniform response across the region of interest, and the desired characteristic for the other parameters is to be small and uniform.

The performance metrics are a set of calculated image quality parameters. They can therefore be applied to any image using any reconstruction method. This provides a valuable method for analyzing elements of EIT including measurement patterns and reconstruction algorithms.

The methods for calculating the five performance metrics are given below. For the calculations, a forward model is created which contains an object of contrasting conductivity. An image is reconstructed using the chosen algorithm and is compared to the original object. For 3D GREIT reconstructions, the final image is comprised of multiple 2D reconstructed layers. This thesis takes a direct parameter calculation approach by calculating a separate value for each layer rather than converting the calculations to 3D parameters.

Finally, a number of the calculations make use of the  $\frac{1}{4}$  max image. The  $\frac{1}{4}$  max image sets the elements of the image with conductivity above or equal to  $\frac{1}{4}$  the maximum conductivity equal to 1 and all remaining elements equal to 0.

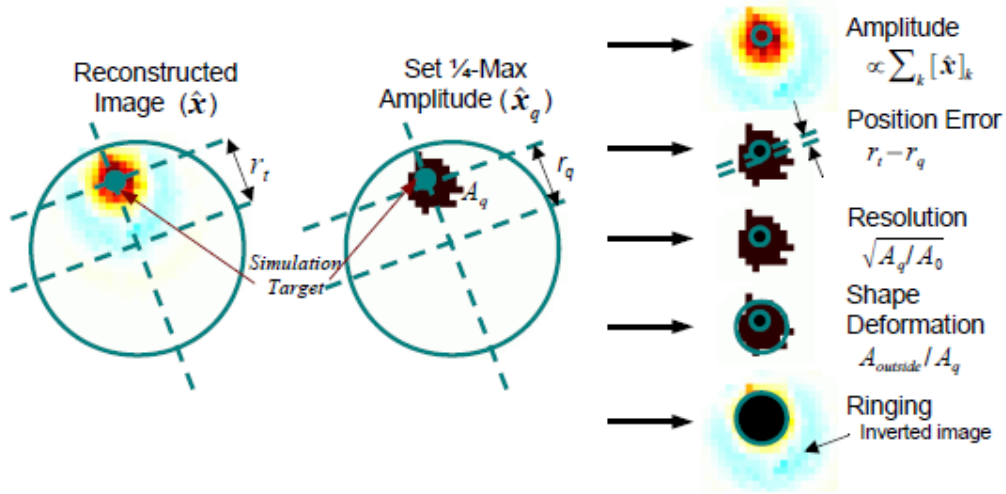


**Figure 4.5** The 5 GREIT performance figures of merit are calculated from reconstructed images  $\hat{x}$  and quarter-max images  $\hat{x}_q$ . The definitions are illustrated on the *left*. Image source [10].

**Amplitude:** the ratio of conductivity amplitudes of the original object (of volume  $V_t$ , object conductivity  $\sigma_t$  and reference conductivity  $\sigma_r$ ) to the conductivity amplitudes  $\hat{x}$  of the reconstructed image.

$$AMP = \frac{\Sigma[\hat{x}]}{V_t \frac{\sigma_t - \sigma_r}{\sigma_r}} \quad (11)$$

**Position Error:** the difference between the calculated centre of mass of the  $\frac{1}{4}$  max image  $r_q$  and the centre of mass of the original object  $r_t$ . A positive value indicates that the image centre of mass is closer to the centre of the image plane than the original object.

$$PE = r_t - r_q \quad (12)$$

**Resolution:** the area of the  $\frac{1}{4}$  max image  $A_q$  divided by the total area of the image reconstruction layer  $A_0$ .

$$RES = \sqrt{A_q / A_0} \quad (13)$$

**Shape Deformation:** a circle  $C$  of area  $A_q$  is calculated, centred on  $r_q$ . Shape Deformation is the area outside of the circle divided by the total  $\frac{1}{4}$  max area.

$$SD = \sum_{k \notin C} [\hat{X}_q]_k / \sum_k [\hat{X}_q]_k \quad (14)$$

**Ringing:** The ratio of the sum of opposite-signed conductivity values outside of circle C to the sum of values inside circle C.

$$RNG = \sum_{k \notin C \& X_q < 0} [\hat{X}_q]_k / \sum_{k \in C} [\hat{X}_q]_k \quad (15)$$

The GREIT parameters as described above are used for analysis methods throughout the thesis results, including the Simulations, Tank Phantom, and Human Measurements. While all contain valuable information, the Amplitude, Position Error and Resolution parameters are considered to be most relevant in this thesis for lung imaging analysis. Amplitude and Resolution relate to the accuracy in lung area and volume measurements, and Position Error can relate to lung boundary positioning as well as regional positioning or inhomogeneous behaviour.

#### 4.3.2 Noise Stability

The Noise Stability is a quantitative approach that has been specifically developed within this thesis as a means of measuring the immunity of a measurement pattern to noise. EIT is prone to a number of sources of error, especially when taking measurements on live subjects. There are a number of sources of noise that may arise, such as electrode movement due to subject movement or electrode cable tension, and changes in electrode surface impedance due to sweat or pressure changes. Noise Stability is proposed as a method for evaluating the stability of a measurement pattern with respect to specific sources of error. A description of the Noise Stability measure is given in Figure 4.6.

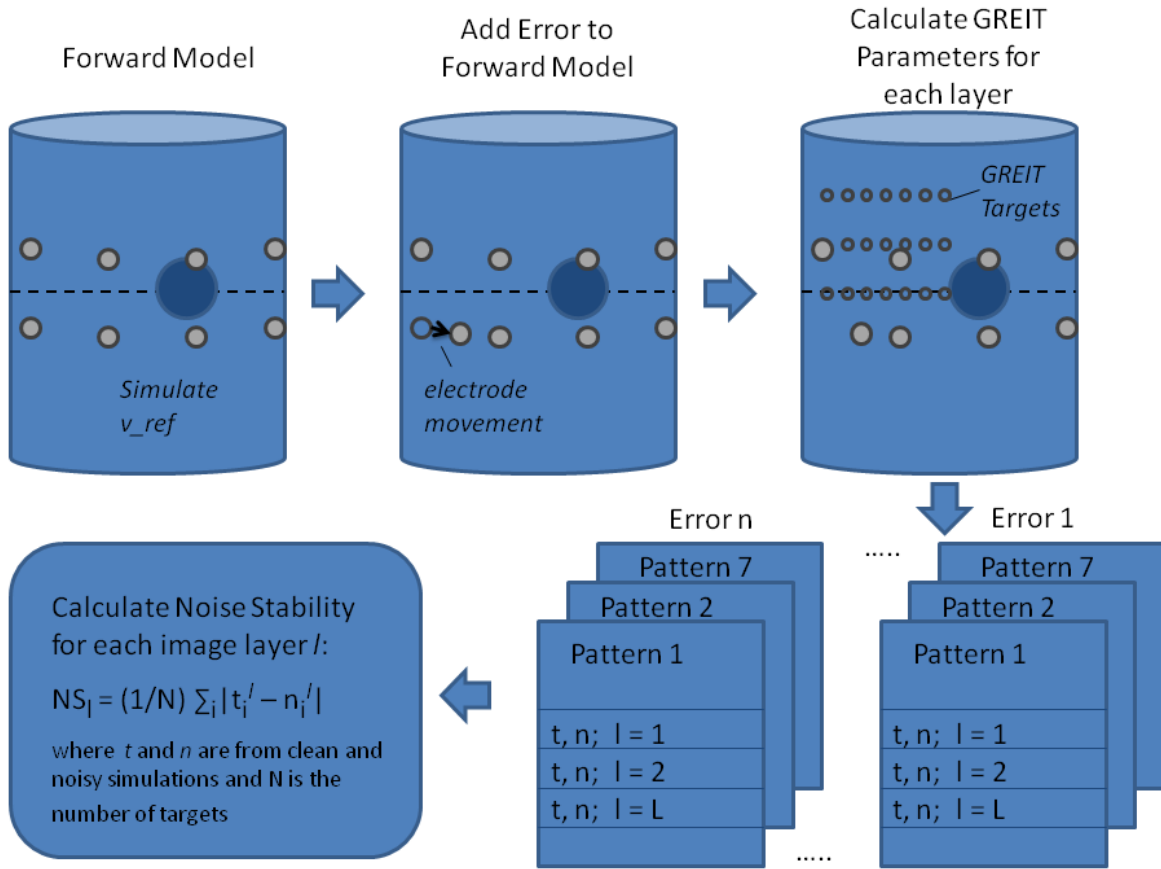


**Figure 4.6** Block Diagram of method for calculation of Noise Stability measure. The parameters  $n$  and  $t$  are the noisy and clean calculated parameter values for each target set for each level. A forward model is created, data is simulated with induced errors, and images are reconstructed. GREIT parameters are calculated from the images, and Noise Stability is calculated using the clean and noisy GREIT parameter values.

In order to calculate the noise figure, a forward model is first created. The object to be imaged is added to the model. The 5 GREIT parameters are then calculated using the forward model as variable  $t$ . This calculation involves creating a set of  $N$  targets on each layer of interest, simulating a measurement set for each target, reconstructing the image, and then calculating the GREIT parameter for that target. Next, an error is added to the model. Figure 4.6 shows an example of an electrode placement error, although the method is used for electrode impedance error as well and can be used for any error. The 5 GREIT parameters are then calculated using the forward model with the error included as variable  $n$ . This results in a set of  $N$  values for each parameter and for each layer. This is repeated for various levels of error.

The Noise Stability can then be calculated. Noise Stability compares the noisy data  $t$  to the clean data  $n$ . two results, generally noisy data and clean data. The Noise Stability  $NS_l$  (where  $l$  is the image layer of interest) is calculated as the mean of the absolute difference between the noisy signal  $n$  and clean signal  $t$ . The calculation is as follows:

$$NS_l = \frac{1}{N} \sum_i |t_i^l - n_i^l| \quad (16)$$

The absolute difference vector  $|t_i^l - n_i^l|$  is also useful to consider when looking at radial variations in response to a given pattern.

The electrode placement error and electrode impedance error are evaluated using both the GREIT parameters and Noise Stability. For the Noise Stability, the result for a parameter is calculated for each reconstructed slice. The values are then normalized.

#### 4.4 Simulation Methods

A large number of simulations have been performed during this research. The two considered to be most significant are Electrode Placement Error and Electrode Impedance Error. The methods for these simulations are described below.

During the acquisition of EIT lung measurements on human subjects, Electrode Placement Error and Electrode Impedance Error can become significant [32]. There are two main reasons for this. First, impedance errors can arise due to poor electrode contact. This can be brought on by patient movement, sweat, or a faulty electrode [33]. Second, electrode placement error can occur due to a subject breathing or moving and pulling on the electrode cables [34]. This is especially true for when a subject must change postures.

##### 4.4.1 Electrode Placement Error

The purpose of this simulation is to test the response of the 7 measurement patterns to an electrode placement error in which a number of electrodes become shifted out of place. An electrode placement error occurs when a physical electrode position does not match the anticipated position in the forward model. This scenario is common when taking measurements on human subjects. There are a variety of physical factors that lead to this, including the physical

rise and fall of the thorax during respiration, potential sweat on the surface of the skin, and tension on the leads attached to the electrodes. All of these factors can give rise to electrode position errors.

The diagram of the Noise Stability measure shown in Figure 4.6 illustrates the steps for the electrode placement error simulation. In order to compare measurement pattern noise response, a forward model is first created. Next, an electrode is moved out of position in order to add an error into the model to generate noisy data. The error is induced by shifting electrodes 1 and 3 along the circumference from 0 to  $10^\circ$  by increments of  $2^\circ$ , as shown in Figure 4.7 One ring of electrodes from the Planar measurement pattern. Electrode placement error is added to the forward model by shifting the electrodes in positions 1 and 3 by  $\theta$  along the circumference of the electrode plane. The data are used to calculate GREIT parameters and Noise Stability measures for each measurement pattern. The noise response is then compared using both evaluation methods.

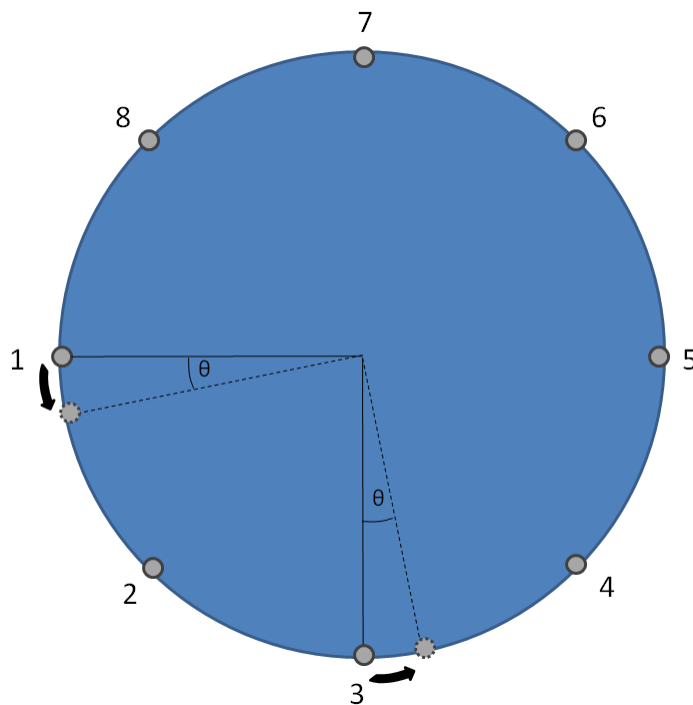


**Figure 4.7** One ring of electrodes from the Planar measurement pattern. Electrode placement error is added to the forward model by shifting the electrodes in positions 1 and 3 by  $\theta$  along the circumference of the electrode plane.

The simulation uses the Cylindrical model designed to match the dimensions of the tank phantom. Electrodes are placed in 2 rings of 8 spanning the centre of the tank. An inverse model is created using the error-free forward model, with the noise figure set to 0.5. Seven equally spaced reconstruction layers are selected to cover the regions around the electrode rings from  $z = 11.1$  to  $22.8$  cm as shown in Figure 4.8. The planes  $13.05$  and  $16.95$  cm fall on the electrode planes. Data are then generated for electrode placement errors from  $0$  to  $10$  degrees. The error is added to the electrodes in positions 1 ( $0^\circ$  on upper layer) and 3 ( $90^\circ$  on upper layer). This is consistent for each pattern.

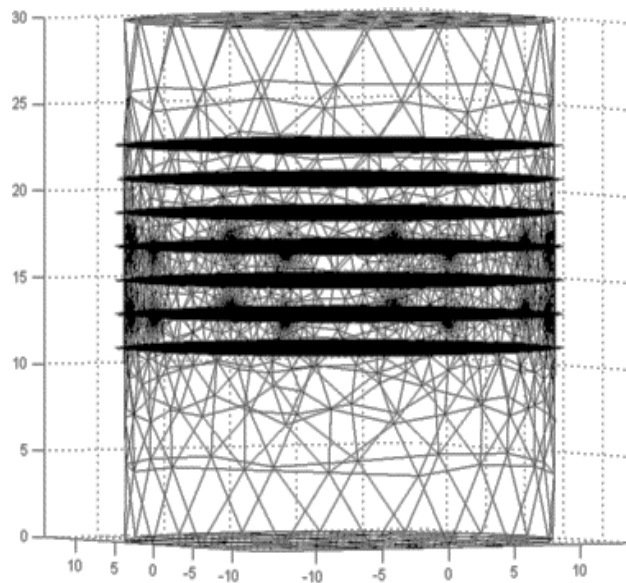


**Figure 4.8** Forward Model using FEM showing 7 reconstruction layers. The layers are at  $z = [11.1, 13.05, 15, 16.95, 18.9, 20.85, 22.8]$  cm. Also shown are the 2 rings of 8 electrodes. The model is used for both Electrode Placement Error and Impedance Error Simulations. Units in cm.

The generated data are used to calculate the GREIT parameters for each layer. The target set that is created to calculate the parameters is shown in Figure 4.9. There are 5 layers of targets at  $z = [15, 16.95, 18.9, 20.85, 22.8]$  cm. These layers are chosen to match the reconstruction layers, and cover the upper half of the model. The set of targets for each layer is placed radially along the  $y$  axis from  $y = 0$  to  $13$  cm, with 100 targets per layer. The target radius is  $0.7085$  cm. The

calculated GREIT parameters therefore represent the behaviour or performance of the image reconstruction radially along the y-axis.

The GREIT parameters are then used to calculate the Noise Stability measure for each layer. This measure represents the amount of change seen in a GREIT parameter when an error is added into the forward model.

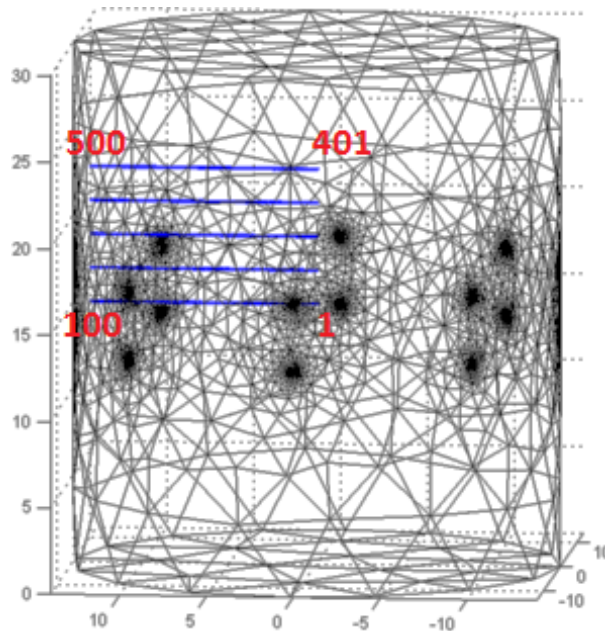


**Figure 4.9** Position of targets for GREIT parameter calculations. There are 100 targets per layer at ( $x = 0$ ) and ( $y = 0$  to 13). Target numbering is shown in red. Layers are set at  $z = [15, 16.95, 18.9, 20.85, 22.8]$ . The target radius is 0.7085. Units in cm.

#### 4.4.2 Electrode Impedance Error

The purpose of this simulation is to test the response of the 7 measurement patterns to an increase in electrode contact impedance. This type of error generally arises due to sweat at the skin surface, poorly cleaned skin, or tension on the electrode connector wire causing the electrode to pull away. This error is simulated by adding large contact impedances into the forward model at multiple electrodes. This simulation uses the Cylindrical model with the same characteristics as the previous test described in Section 3.1.1.

An inverse model is created using the error-free forward model, with a noise figure of 0.5. Seven equally spaced reconstruction layers are again selected to cover the regions around the electrode rings from  $\ell = 11.1$  to 22.8 cm as shown in Figure 4.8. Data are then simulated for different levels of electrode impedance error. For each increased level of error, the contact impedance at two additional electrodes is set to  $1e12 \Omega$ . The electrode pairs are (1,4), (2,5), (11,12), (6,7), and (14,15). For example, the third level of error has the impedance error added to electrodes (1,4), (2,5), and (11,12)..

The simulated data are used to calculate the GREIT parameters for each layer. The same target set is used as for the Electrode Placement Error simulation, as shown in Figure 4.9. The GREIT parameters are then used to calculate the Noise Stability measure for each layer.

## 4.5 Simulation Results

### 4.5.1 Electrode Placement Error

The results described in this section are focused on GREIT parameter calculations derived from the Electrode Placement Error simulation. Errors are introduced into the electrode positioning in the forward model in order to create sets of noisy data. The performance of the patterns in relation to this noise are explored in terms of GREIT parameter values, average GREIT parameter value by layer, and finally by Noise Stability.

#### 4.5.1.1 GREIT Parameter Performance

The first important results are derived from the analysis of the GREIT parameters. The results shown in Figure 4.10 are for the Position Error and Resolution parameters. These parameters along with Amplitude are considered to be the most interesting for lung imaging, as discussed in Section 4.2.1. The results for Amplitude did not indicate clear differences in pattern performance and are not shown. Parameter values are calculated for 500 radial points as shown in Figure 4.9.

Several trends are apparent in the results shown in Figure 4.10. The behaviour of each pattern is quite similar over the target layers, which is not unexpected. However, there are clear similarities in performance for groups of similar patterns. Furthermore, the similarities are present for both Position Error and Resolution. For the Position Error, the Zigzag, Zigzag Offset and Square

patterns have poor performance with Zigzag being especially poor further from the model centre on Layer 3-5. Planar and Planar Offset again have the best performance except towards the edge on Layer 1 (targets 1-100). At that point they have the highest Position Error. Planar Opposite and Zigzag Opposite show similar trends and have medium performance over all layers.

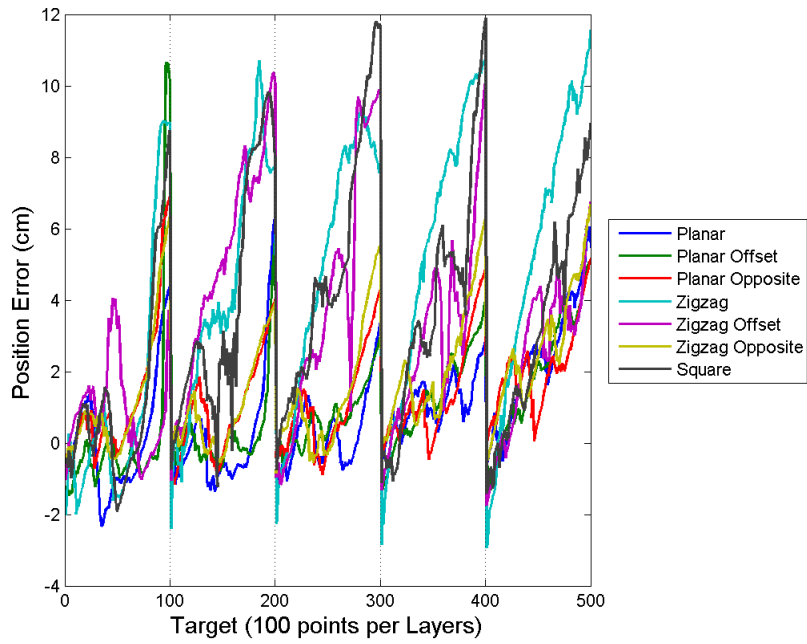
The Planar Opposite and Zigzag Opposite patterns have the highest values for Resolution, indicating poor performance, and are especially poor in the centre of the tank. The Zigzag and Zigzag Offset patterns have the next highest values, followed by the Square pattern. The Planar and Planar Offset patterns show the best performance.

The mean of the absolute values of the GREIT parameter results for each pattern are plotted in Figure 4.11 below. Values are calculated for each of the five target layers. The absolute value step is used primarily for Position Error, which can have both positive and negative values. A positive value indicates that the centre of the reconstructed image is closer to the edge of the model than the true target position, and a negative value indicates the image centre is closer to the centre of the model.

The graph of Position Error vs. Layer shows strong scores for Planar, Planar Offset, Planar Opposite, and Zigzag Opposite. The Zigzag, Zigzag Offset, and Square patterns show much different response with high position error, particularly at Layers 2 and 3.

The graph of Resolution vs. Layer shows a consistent increase in Resolution for all 7 patterns when moving from the centre layer to the outer layer. The Planar and Planar Offset pattern have the best performance with significant separation from the other five patterns. The two Opposite patterns have the highest parameter values. The Zigzag, Zigzag Offset, and Square perform slightly better, particularly at Layer 1.

### Radial Position Error for 8 degree Electrode Placement Error



### Radial Resolution for 8 degree Electrode Placement Error

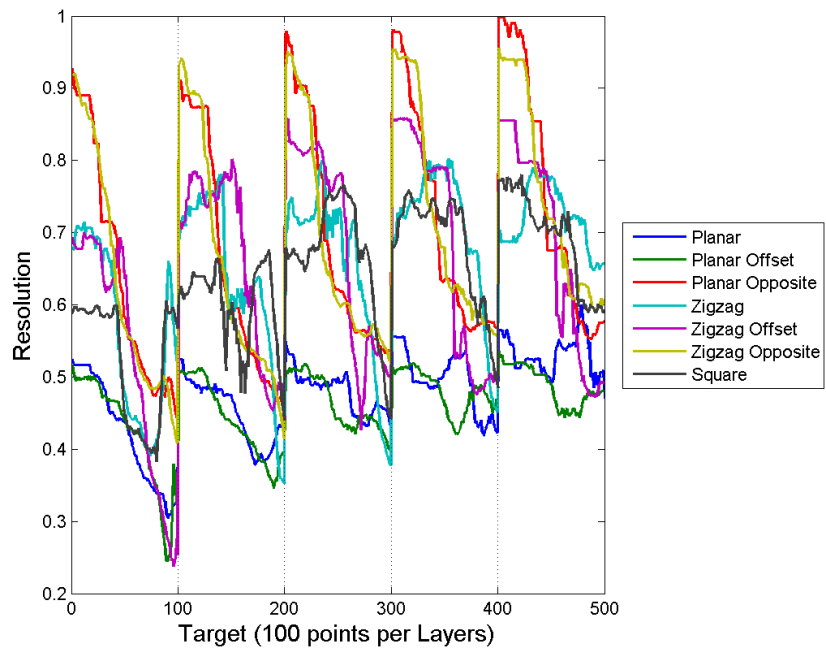
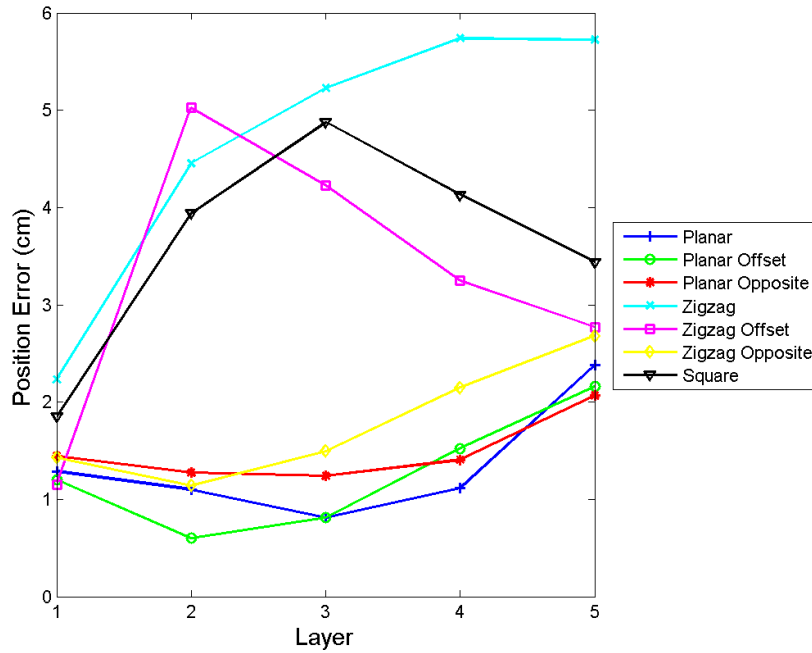


**Figure 4.10** Graphs showing GREIT Parameter results for the 7 measurement patterns when an electrode placement error is introduced. The parameters shown are Position Error (top) and Resolution (bottom), plotted for each target from 1 to 500. There are 100 targets per layer, number from centre to edge starting with the centre layer.

Mean Position Error by layer for 8 degree Placement Error



Mean Resolution by layer for 8 degree Placement Error

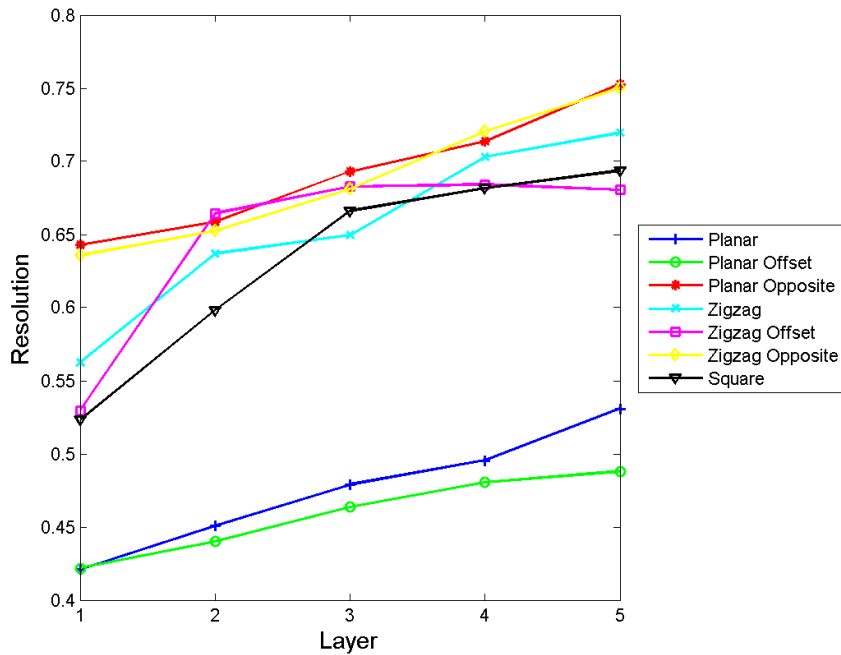


**Figure 4.11** The absolute values of the GREIT Parameters are averaged over each Target layer for the 7 Measurement Patterns. Parameters shown are Position Error (top) and Resolution (bottom) with an 8 degree Electrode Placement Error.

Overall, Planar and Planar Offset patterns have the best performance for Position Error and Resolution when considering Electrode Placement Error. The remaining five patterns show much higher susceptibility to electrode movement. For Position Error, the Electrode Placement Error has the highest impact on the Zigzag, Zigzag Offset, and Square patterns. For Resolution, the Electrode Placement Error has the highest impact on Planar Opposite and Zigzag Opposite, with similar performance between the five parameters towards the edge of the model.

#### *4.5.1.2 Noise Stability*

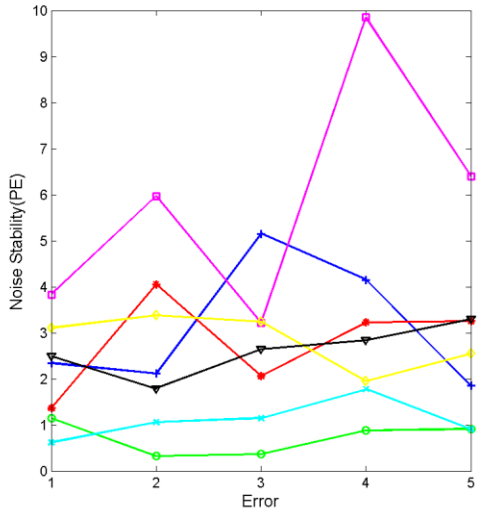
The second set of results looks at pattern stability. The preceding method of analysis does not explore the effect of increased noise on the performance of each pattern. Therefore, a measure of the stability of each measurement pattern is determined. This is done using the Noise Stability measure, described in Section 4.3.2, which gives the average change in GREIT parameter performance over a reconstruction layer due to the addition of noise to the system. The results are examined in order to give a measure of the expected Noise Stability in an experimental measurement system.

The graphs in Figure 4.12 display the stability response of each measurement pattern in relation to Electrode Placement error. The error is a shift of 2 electrodes along the model circumference by 2, 4, 6, 8, and 10°, as shown in Figure 4.7. A higher value indicates poorer stability. A separate graph is produced for each target layer.

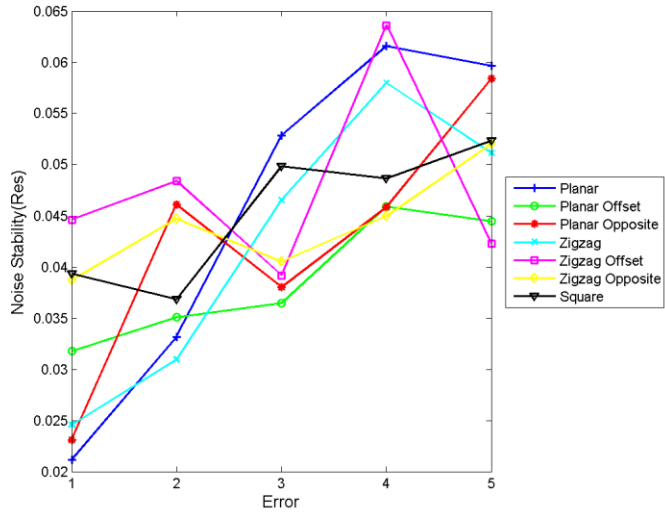
### GREIT Position Error vs. Electrode Placement Error

### GREIT Resolution vs. Electrode Placement Error

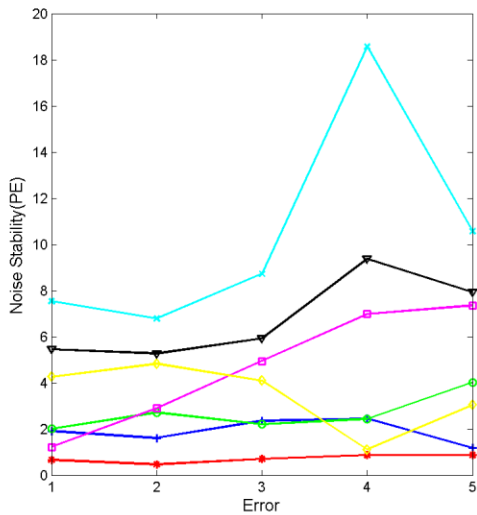
Noise Stability(PE) vs Electrode Placement Error for Layer 1



Noise Stability(Res) vs Electrode Placement Error for Layer 1



Noise Stability(PE) vs Electrode Placement Error for Layer 2



Noise Stability(Res) vs Electrode Placement Error for Layer 2

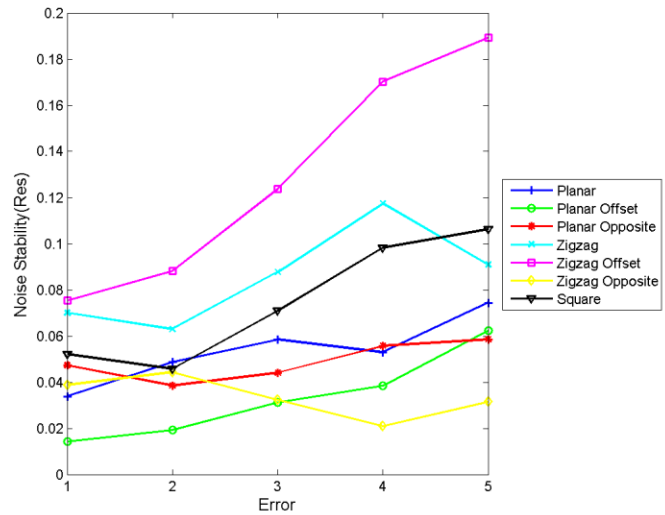
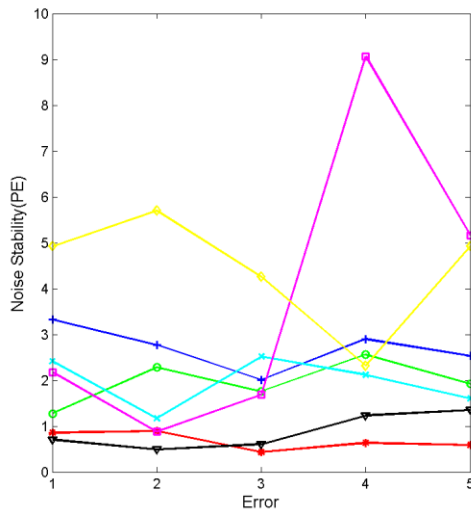
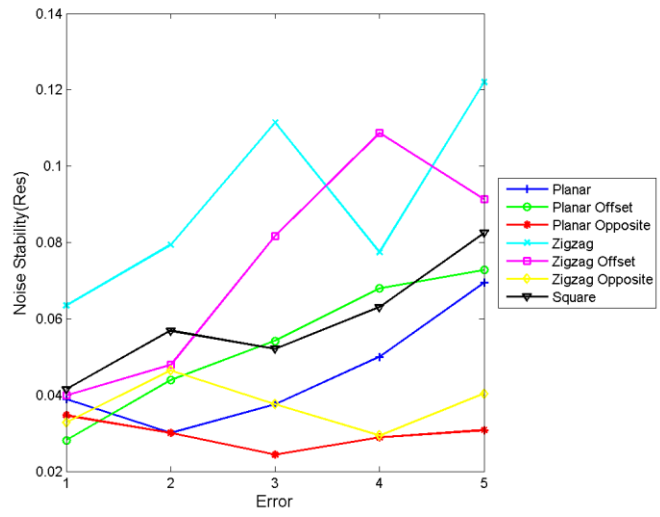


**Figure 4.12** Noise Stability Measure vs Electrode Placement Error for 5 Error Levels. Position Error (left column) and Resolution (right column) are shown for Layers 1-5 in separate graphs. *(continued on next page)*

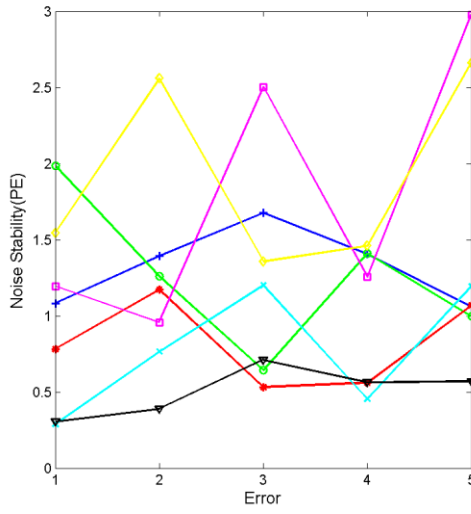
Noise Stability(PE) vs Electrode Placement Error for Layer 3



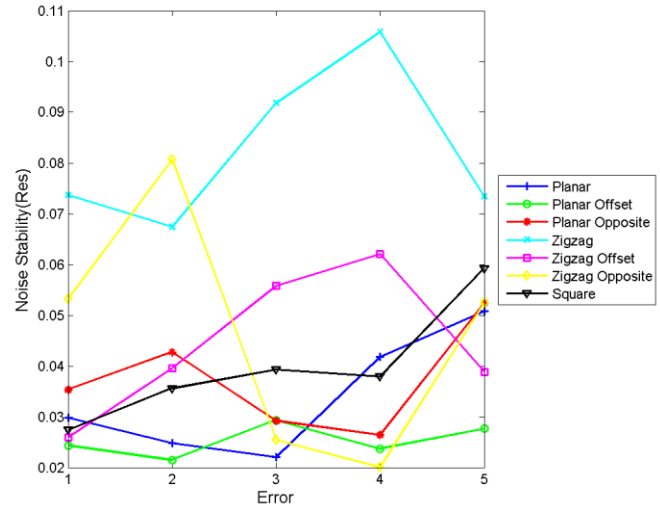
Noise Stability(Res) vs Electrode Placement Error for Layer 3



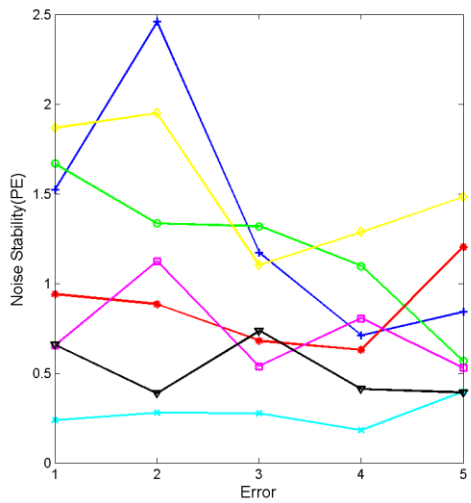
Noise Stability(PE) vs Electrode Placement Error for Layer 4



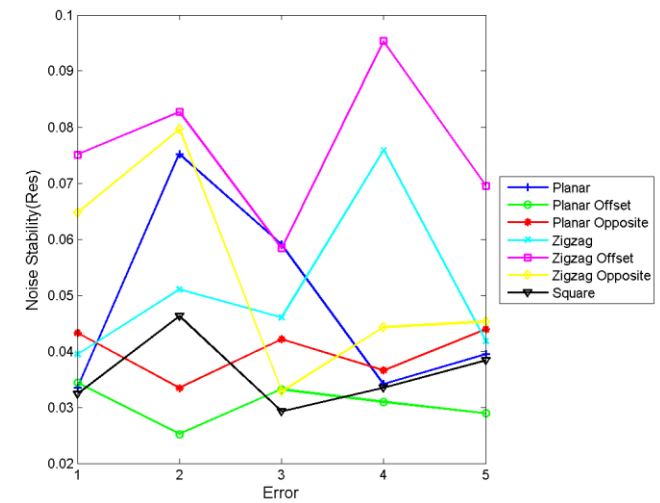
Noise Stability(Res) vs Electrode Placement Error for Layer 4



Noise Stability(PE) vs Electrode Placement Error for Layer 5



Noise Stability(Res) vs Electrode Placement Error for Layer 5



There are several interesting results. All patterns have similar results for Resolution on Layer 1. The results for Layer 2 show the clearest performance separation, ordered Planar Offset, Zigzag Opposite, Planar Opposite, Planar, Square, Zigzag, and Zigzag Offset in descending order of performance. For Layers 2 to 4, the Zigzag and Zigzag Offset patterns show the poorest Resolution stability. The Square, Planar, and Planar Offset patterns have consistently strong Noise Stability.

The Noise Stability results for Position Error are less consistent. The Zigzag Offset pattern has the poorest Noise Stability on Layers 1, 3, and 4. On Layer 2 at the electrode plane, the Zigzag and Square patterns perform very poorly. The Planar Offset, Planar Opposite and Square patterns show the most stable response overall.

Finally, the overall Noise Stability for both Position Error and Resolution decreases as the layer moves away from the centre. The added error has a much greater effect in the regions close to the electrodes.

#### 4.5.2 Electrode Impedance Error

The results described in this section are for the GREIT parameters derived from the Electrode Impedance Error simulation. High contact impedance is introduced at select electrodes in order to add error into the simulated measurements. GREIT parameters are then calculated in order to compare the response of the measurement patterns to the noise.

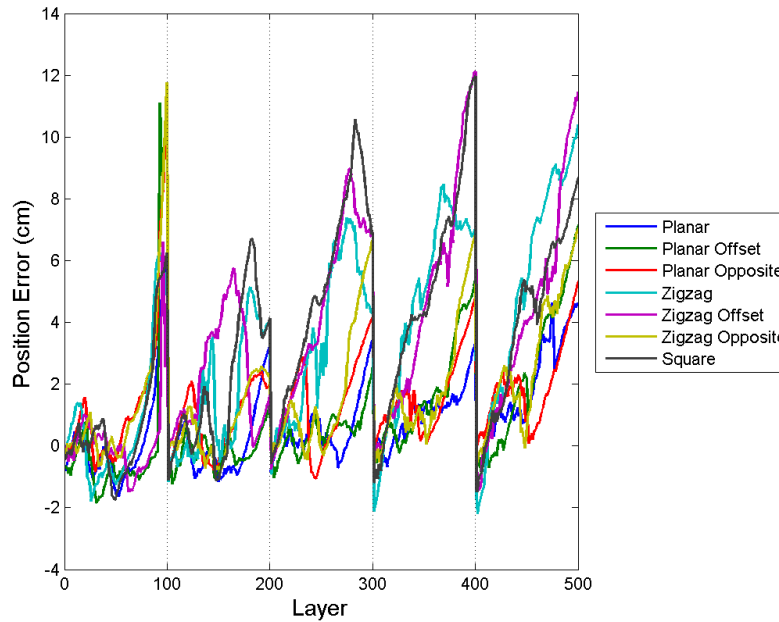
##### 4.5.2.1 GREIT Parameter Performance

Again, Position Error and Resolution are primarily considered. In Figure 4.13 the two parameters are plotted for the 7 patterns. Results are given with 100 radial points per layer (centre to outside) starting with the centre layer. The trends of the measurement patterns are similar to those for Electrode Placement Error in Section 4.5.1.1.

As with the Electrode Placement Error, the Planar Opposite and Zigzag Opposite patterns have the highest GREIT parameter values for Resolution, especially in the centre of the model, and medium performance for Position Error. The Planar and Planar Offset patterns have the best performance for Position Error and Resolution except for at the edge of the model on Layer 1.

For Resolution, the Zigzag, Zigzag Offset and Square patterns have similar performance with the Square pattern performing better in the centre of the model on Layers 1 and 2.

Radial Position Error with added Electrode Impedance Error



Radial Resolution with added Electrode Impedance Error

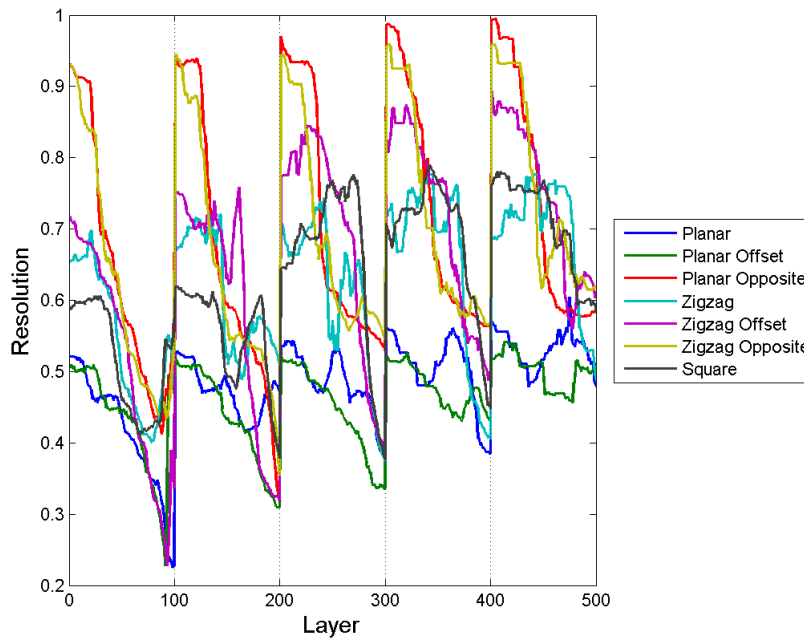


**Figure 4.13** Graphs showing GREIT Parameter results for the 7 measurement patterns with an electrode placement error introduced. The parameters shown are Position Error (top) and Resolution (bottom), plotted for each target from 1 to 500 with 100 targets per layer. Numbering is from centre to edge.

The means of the absolute values of the GREIT parameters are plotted in Figure 4.14 below. The pattern performance for the Position Error and Resolution are similar to the Electrode Placement Error results. For Position Error, the Zigzag, Zigzag Offset and Square patterns perform significantly worse than the other four patterns over Layers 3 to 5. There is no clear separation at Layer 1 and small separation at Layer 2. The Position Error for the Zigzag, Zigzag Offset and Square patterns at the electrode plane on Layer 2 is clearly less affected by Electrode Impedance Error than it is by Electrode Placement Error.

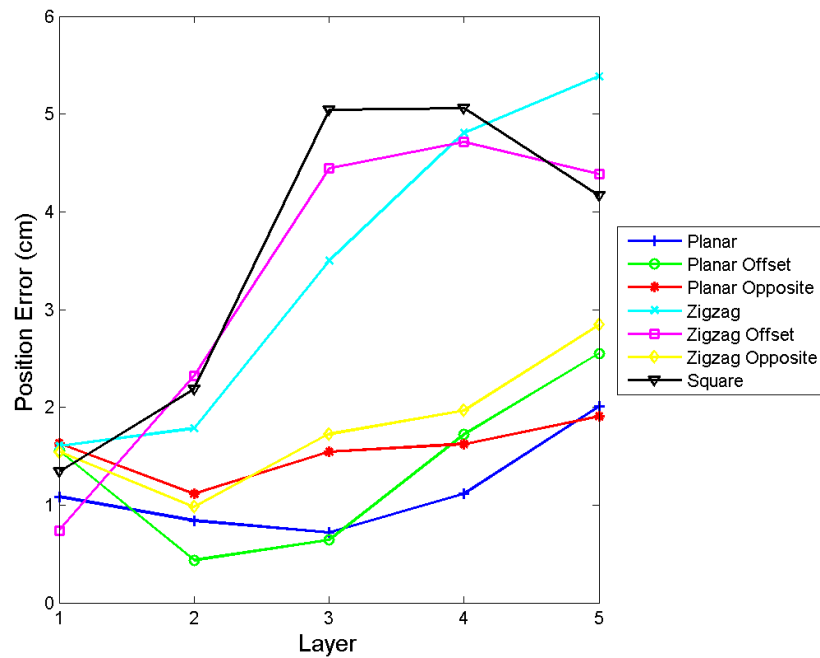
The Resolution results show a clear separation between the Planar and Planar Offset patterns and the remaining 5 patterns with the former two patterns showing much stronger performance. As with the Electrode Placement Error results, the Planar Opposite and Zigzag Opposite patterns perform the worst overall.

#### *4.5.2.2 Noise Stability*

This section looks at the Noise Stability in the GREIT parameters due to the addition of noisy conditions. The graphs in Figure 4.15 show the Noise Stability of each measurement pattern in relation to Impedance error. A higher value indicates poorer stability. The results are examined in order to give a measure of the expected Noise Stability in a real measurement set.

The results shown in Figure 4.15 show very low Noise Stability values which point to very small changes in the GREIT parameters with the addition of impedance error to the model. In general, the Noise Stability value increases as the error is increased. However, the effects of the error are very small, on the order of  $10^{-3}$  for Position Error and  $10^{-4}$  for Resolution, which indicates that in this test the impedance error has little impact on the reconstructed images and does not contribute to the analysis of the performance of the measurement patterns.

Mean Position Error by layer with added Impedance Error



Mean Resolution by layer with added Impedance Error

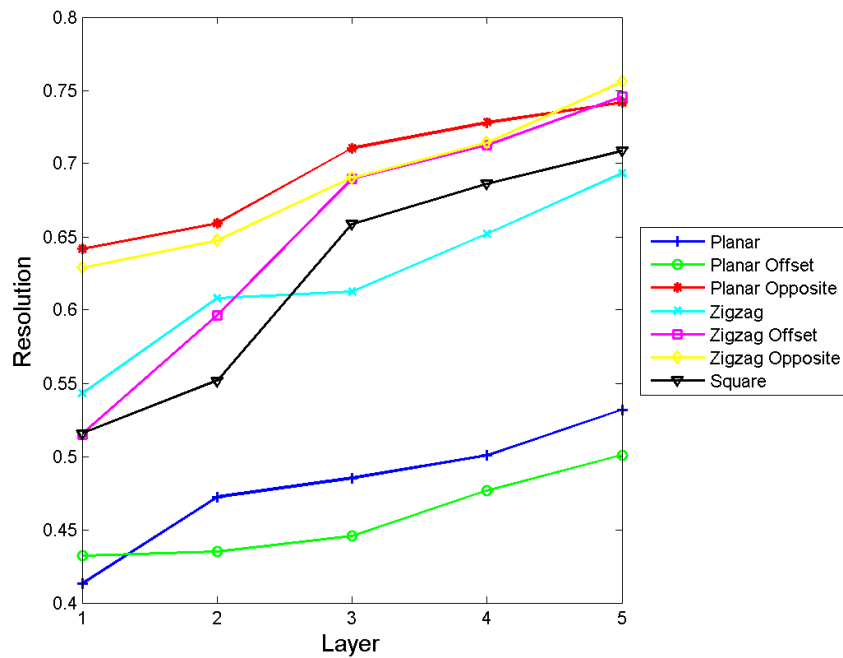


**Figure 4.14** The absolute values of the GREIT Parameters are averaged over each Target layer for the 7 Measurement Patterns. Parameters shown are Position Error (top) and Resolution (bottom) with Impedance Error on 8 electrodes.

GREIT Position Error vs. Electrode Impedance Error

GREIT Resolution vs. Electrode Impedance Error

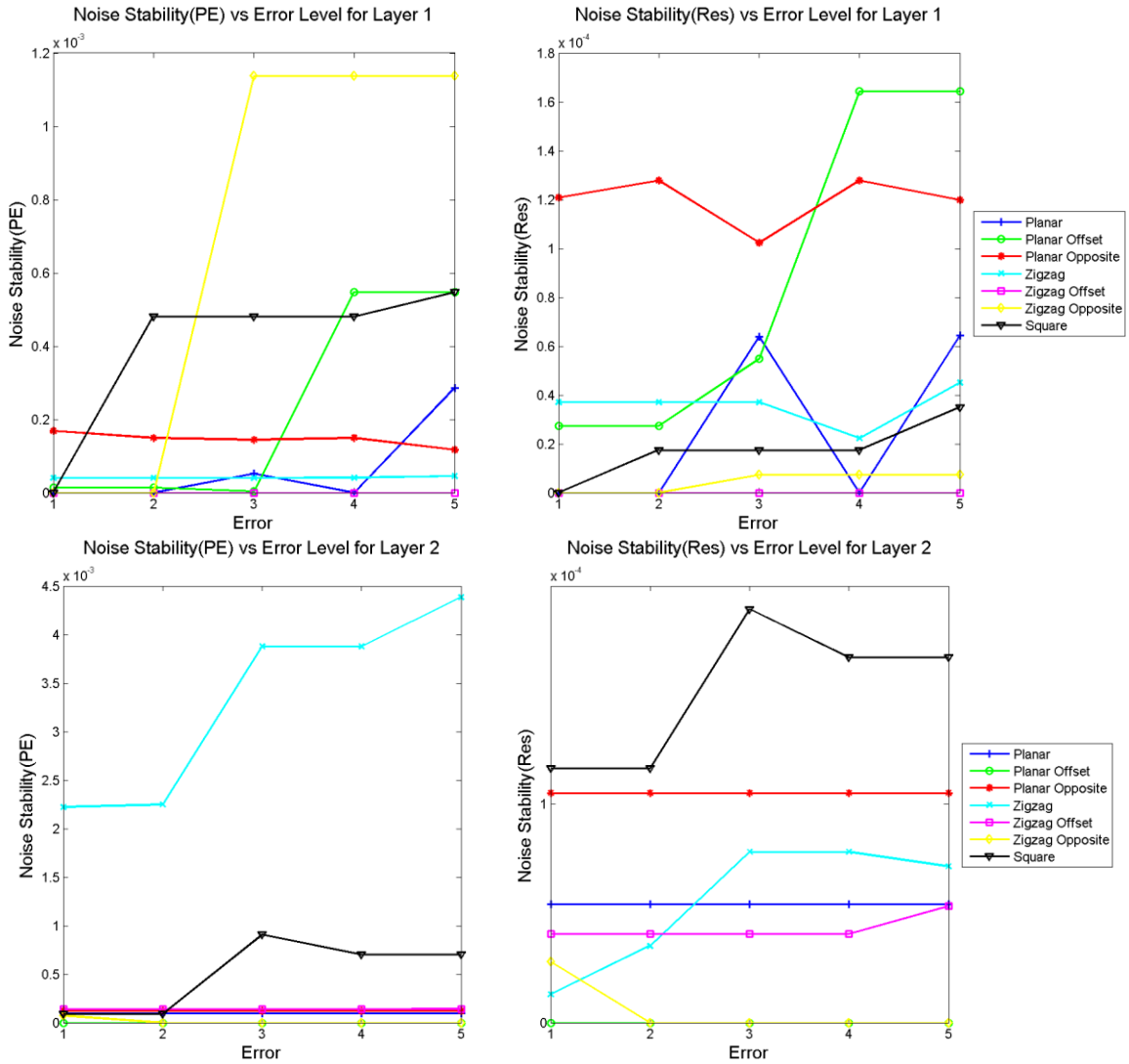
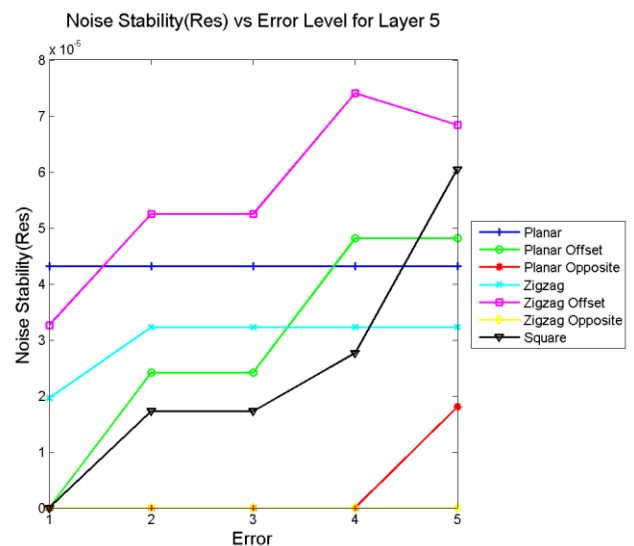
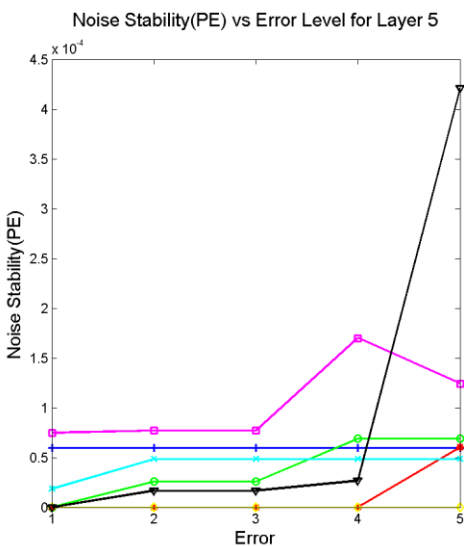
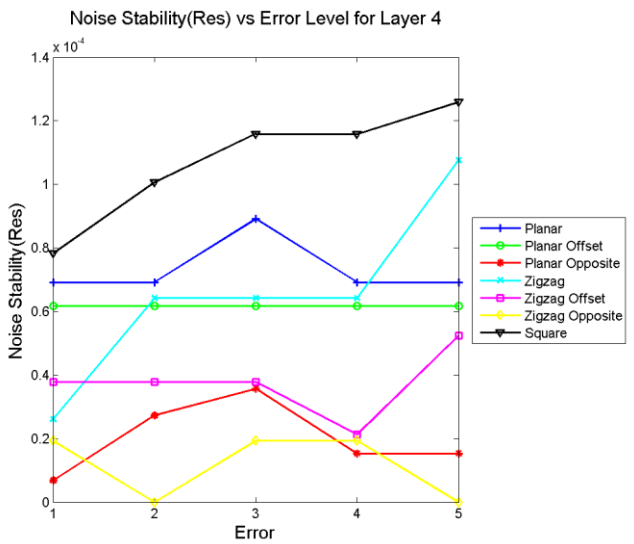
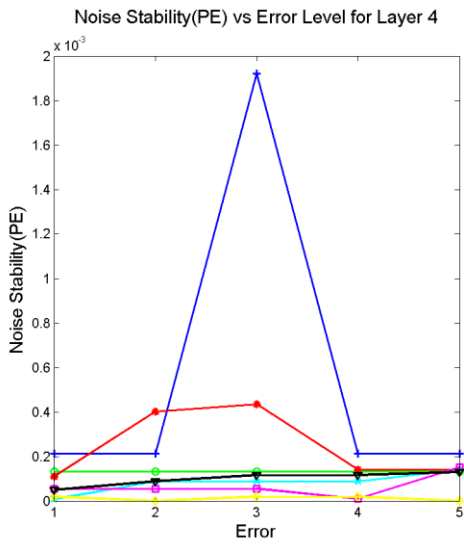
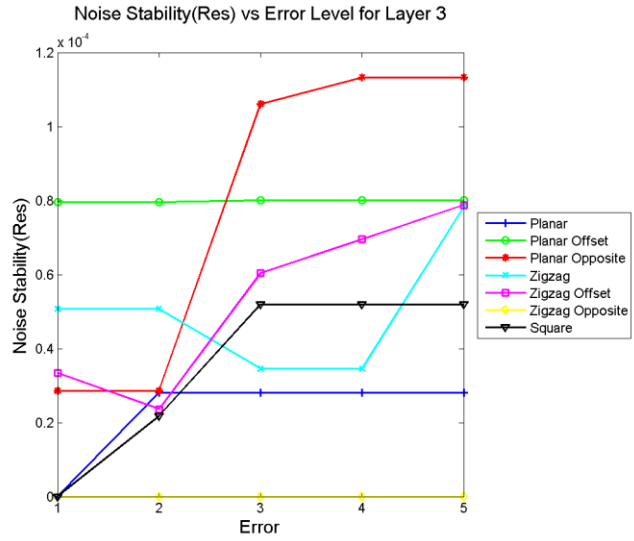
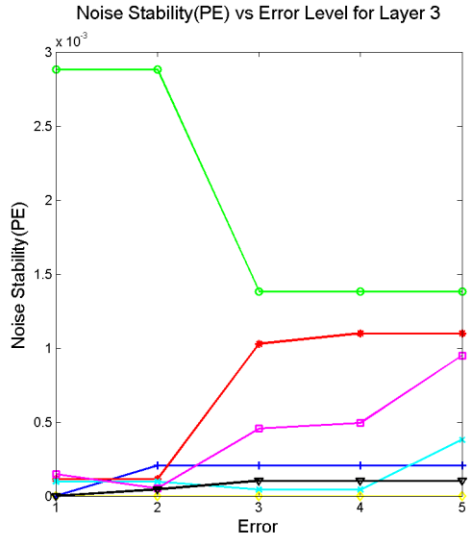


**Figure 4.15** Noise Stability Measure vs Electrode Impedance Error for 5 Error Levels. Position Error (left column) and Resolution (right column) are shown for Layers 1-5 in separate graphs. (continued on next page)



## 4.6 Discussion

The results of the Simulations describe the effects of electrode placement error and electrode impedance error on the performance of the 7 measurement patterns. Performance is analyzed in terms of radial GREIT parameter values across 5 layers, mean GREIT parameter value by layer, and Noise Stability over a range of error. The two key GREIT parameters that are considered most significant are the Position Error and the Resolution.

### 4.6.1 GREIT Parameters

Analysis of Position Error and Resolution shows clear separation in pattern performance over all layers. The patterns can be divided into four groups based on noise response: Planar and Planar Offset, Planar Opposite and Zigzag Opposite, Zigzag and Zigzag Offset, and Square. The Square pattern is quite close in performance to the Zigzag and Zigzag Offset patterns but has distinct behaviour in several cases. These groupings are especially clear in Figure 4.11, which shows clear groupings for both Position Error and Resolution results.

The Planar and Planar Offset patterns clearly are the strongest performers and show the lowest susceptibility to noise. The one area where these two patterns perform poorly is close to the model edge on Layer 1. The Planar Opposite and Zigzag Opposite patterns show medium performance. They have the poorest results for Resolution with very low performance at the centre of the model, but have good results for Position Error.

The Zigzag, Zigzag Offset and Square patterns are especially susceptible to Electrode Placement Error. This is most evident by comparing the graphs of Mean Position Error vs. Layer in Figure 4.11 and Figure 4.14. In both graphs the response of the Planar, Planar Offset, Planar Opposite and Zigzag Opposite patterns is quite similar. However, on Layer 2 the Zigzag, Zigzag Offset and Square pattern see significantly higher Position Error for Electrode Placement Error than for Electrode Impedance Error. The effect can also be seen for Resolution to a smaller degree.

Overall the Zigzag, Zigzag Offset and Square patterns are the weakest performers in terms of GREIT parameters. Square performs better in terms of Position Error, specifically in the centre of

the model. Zigzag and Zigzag Offset are quite similar with Zigzag performing worse further from Layer 1.

In general, the Position Error and Resolution parameters trends display opposite behaviour in the radial direction. For Position Error the error increases significantly when moving towards the edge whereas Resolution results improve when moving towards the edge. There are several exceptions, however. The Planar Offset and Square patterns see a spike in the Resolution parameter towards the edge of the model on Layer 1. In the Z-direction, both Position Error and Resolution see a decrease in quality when moving from Layer 1 to Layer 5 which is expected.

#### 4.6.2 Noise Stability

The results of the Noise Stability (NS) analysis are less straightforward. The expected result is for the NS value to increase with error, corresponding to a decrease in performance, which is generally what is seen in the results. However many cases do not follow this trend, and provide unexpected and inconsistent results.

A comparison of the NS results for Electrode Placement Error shows several interesting trends. For Resolution, pattern performance at Layer 1 is quite uniform with a similar increase in NS for all patterns as error is increased. For the remaining layers, the Planar, Planar Offset and Square patterns remain relatively low while the Zigzag and Zigzag Offset patterns have higher NS with non-linear response to increased error. The Position Error results are less consistent. Zigzag, Zigzag Offset and Square show poor performance on various layers while the remaining patterns are more stable.

The NS results for Electrode Impedance Error are much smaller than for Electrode Placement Error, on the order of  $10^{-3}$  for Position Error and  $10^{-4}$  for Resolution. NS results for Electrode Placement Error were on the order of  $10^1$  for Position Error and  $10^{-1}$  for Resolution. This suggests that the Impedance Error designed in this simulation had very little impact on the measurement. There are several reasons as to why this may be. First, the simulation was run without adding Gaussian noise. The simulation may have been able to generate adequate measurements with fewer electrodes. EIT uses a large number of individual measurements to calculate an image. If several electrodes are providing erroneous data, the remaining measurements may be sufficient

given an ideal system to produce the same result. The results of the electrode impedance error analysis will likely be more relevant if Gaussian noise is added into the system.

Second, the mesh density of the model may have been too low to properly observe the effects of the added impedance error. The model does have higher mesh density at the electrodes but increasing the mesh density throughout the FEM may yield better results.

The results for both Electrode Placement Error and Impedance Error show a consistent increase in NS with increased error. However, with the exception of Layer 1, the overall NS amplitude decreases from Layer 2 to Layer 5. The trends of the results also become more inconsistent in the outer layers. It is clear, therefore, that adding error into the forward model has more of an effect in the centre layers than in the outer layers.

The NS at Layer 1 is consistently lower than at Layer 2 which suggests better Noise Stability at the centre plane of the model than at the electrode planes.

The inconsistencies in behaviour of the results with increased error may be due to the nature of the GREIT parameters. Each parameter represents a measure of a specific aspect of image quality, and is not a complete measure of the system by itself. Therefore an increase in a systematic error in the system may not result in a corresponding linear change in a GREIT parameter.

Since the EIT problem is an ill-posed problem, there are multiple solutions to the problem and the solution is found by including a priori information and desired behaviour. The reconstruction algorithm will therefore also have an effect on the noise performance. In this work, a single algorithm was used and the noise figure was kept constant in order to limit the reconstruction algorithm as a factor in the noise results for different measurement patterns. However, this effect is an important area to explore in future work.

The results appear more random at the outer layers for both Electrode Placement Error and Impedance Error. This may be explained by the fact that the image quality is generally lower here, as shown in analysis of the GREIT parameters and of the mean GREIT parameter vs. Layer. The

effect of an added error on the image quality for a noisy image reconstruction will appear more random than for a cleaner image reconstruction.

This leads to a drawback of the NS parameter. A measurement pattern that gives poorer performance may give a better NS result. Therefore the trend in the Noise Stability should be considered in addition to the amplitude. The desired result is therefore a low amplitude with a smooth rise in NS with increased error. The Planar Opposite and Zigzag Opposite patterns, for example, had very strong Position Error NS results for the Electrode Placement Error test. However, the lack of response to increased error suggests that the Opposite patterns are simply poor performing measurement patterns.

To summarize, the Planar and Planar Opposite show the strongest overall performance. The Planar Opposite and Zigzag Opposite patterns show medium Position Error performance and poor Resolution performance. The Zigzag, Zigzag Offset and Square patterns have poor noise performance and are especially susceptible to Electrode Placement Error. Finally, the Planar, Planar Offset and Square patterns have the lowest, most stable NS results.

## 5 Tank Phantom Experiment

This chapter describes results from an experiment performed using an EIT Tank Phantom apparatus. There are two purposes for the undertaking of this experiment: first, to evaluate the performance of the seven 3D measurement patterns using an experimental apparatus and compare with simulated results; and second, to select the three best-suited patterns to be used for the Human Measurements experiment described in the following chapter.

In the experiment a block is placed in a range of positions within the tank and EIT measurements are made using the 7 measurement patterns. Images are reconstructed and the performance of the patterns is compared using the GREIT parameters.

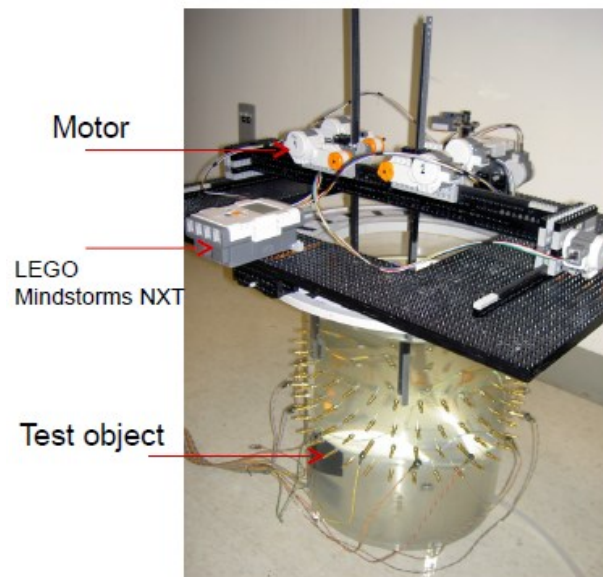


**Figure 5.1** Experimental apparatus consisting of Tank Phantom, Goe-MF II EIT device, and LEGO Robotic 3D Object Positioning system. Image source [35].

### 5.1 Experimental Apparatus

The experimental apparatus consists of a cylindrical tank with a height of 30 cm and diameter of 28 cm. Electrode fittings are installed through the walls of the tank in a series of rings at heights of 13.2, 17.1, 20.3, and 24.2 cm, with 32 electrode fittings per ring. This allows for the leads from the EIT device to be placed in a variety of arrangements. The tank is filled with water with the

salinity set to 4.5 mS. The salinity has been measured using an ECTestr-high 0-19.90 mS salinity device.

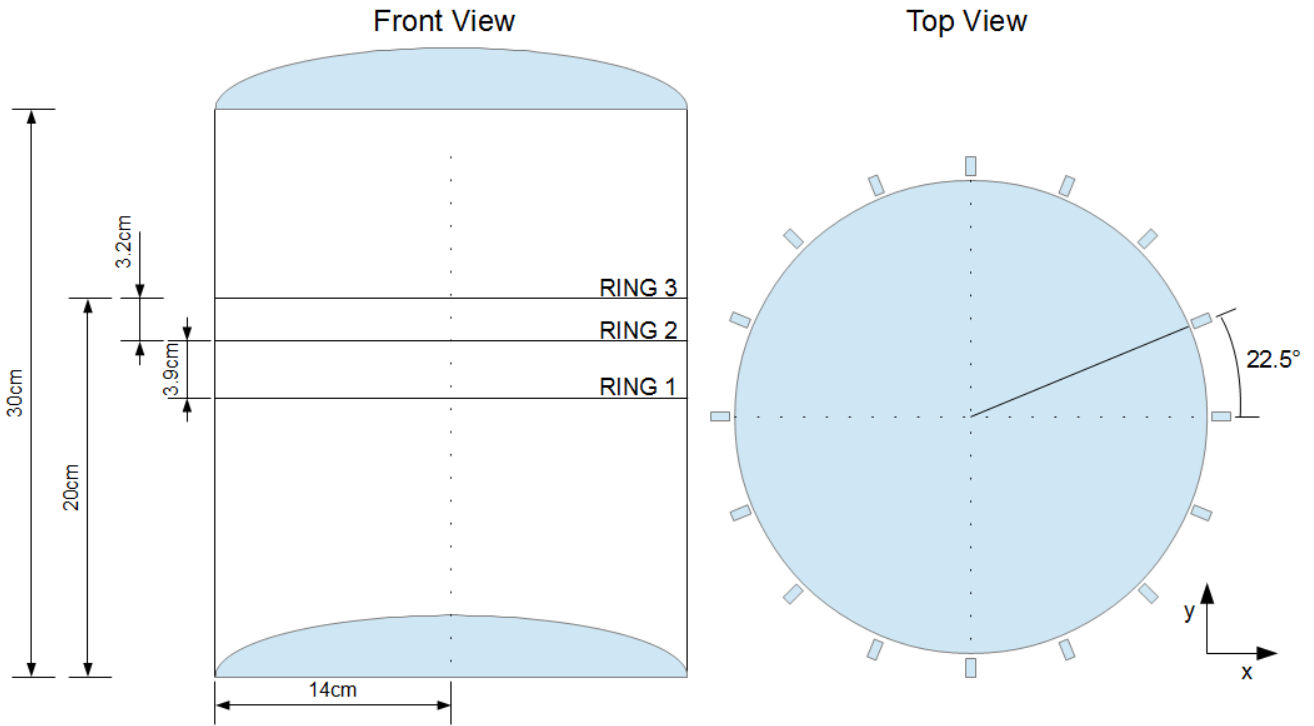


**Figure 5.2** Tank Phantom Dimensions. Rings of electrodes fittings are installed in the wall of the tank to allow for flexibility in measurements. Plane separations of 3.2 cm (rings 2 & 3) and 7.1 cm (rings 1 and 3) are used during this experiment. 32 fittings are installed equidistantly around the ring. This experiment only used 16 electrodes, shown in the Top View of the diagram.

The tank dimensions and electrode arrangements are shown in Figure 5.2. The tank data for this experiment are recorded using the Goe-MF II device. Measurements are taken using the *adjacent* current pattern with the standard 208 electrode pair voltage measurements per EIT frame, corresponding to one image. The cables from the device are snapped onto the fittings of the tank. Measurements are taken with the following settings:

Electrical stimulation frequency:	50 kHz
Effective applied current:	5 mA
Waveform:	sinusoidal
Sampling Rate:	13 frames/second
Number of electrodes:	16 plus 1 ground

A robotic system, shown in Figure 5.1 is used to place a plastic block in specified locations within the tank. The system uses 2 LEGO Mindstorms controllers to control the position of the suspended block. A plastic cube with sides of 4.5 cm is used for the measurements. There is some error associated with this system, as the block does not hang perfectly vertical on its attachment rod. The rod which suspends the block will also have a small influence on the measurements. Based on observing the system an estimate of the position error is 0.8 cm.

## 5.2 Experimental Procedure

This experiment compares image quality for the 7 measurement patterns using a tank phantom apparatus. In the experiment, the plastic block is moved to 15 different positions, which are shown in Figure 5.3. The block position error is estimated to be  $\pm 0.3$  cm. The locations consist of 5 radial positions repeated on 3 levels. In order to reduce noise, a measurement set of 130 EIT frames are recorded for each block position and averaged to produce a single mean EIT frame for each block position. An additional set is recorded and averaged with the block removed from the tank to be used as a reference measurement.

A full measurement set including reference is taken for each of the 7 measurement patterns. The patterns are shown in Figure 4.1 and Figure 4.2. In order to achieve the measurement patterns, the electrodes are manually connected to the tank electrode fittings in the correct positions.

The full measurement protocol is repeated for two different electrode plane separations. The electrode plane separations used are 3.2 cm and 7.1 cm. The first electrode plane separation uses the electrode rings at heights 17.1 cm and 20.3 cm, and the second plane separation uses heights of 13.2 cm and 20.3 cm. For both plane separations, the centre plane where blocks 1-5 are positioned is set halfway between the electrode planes.

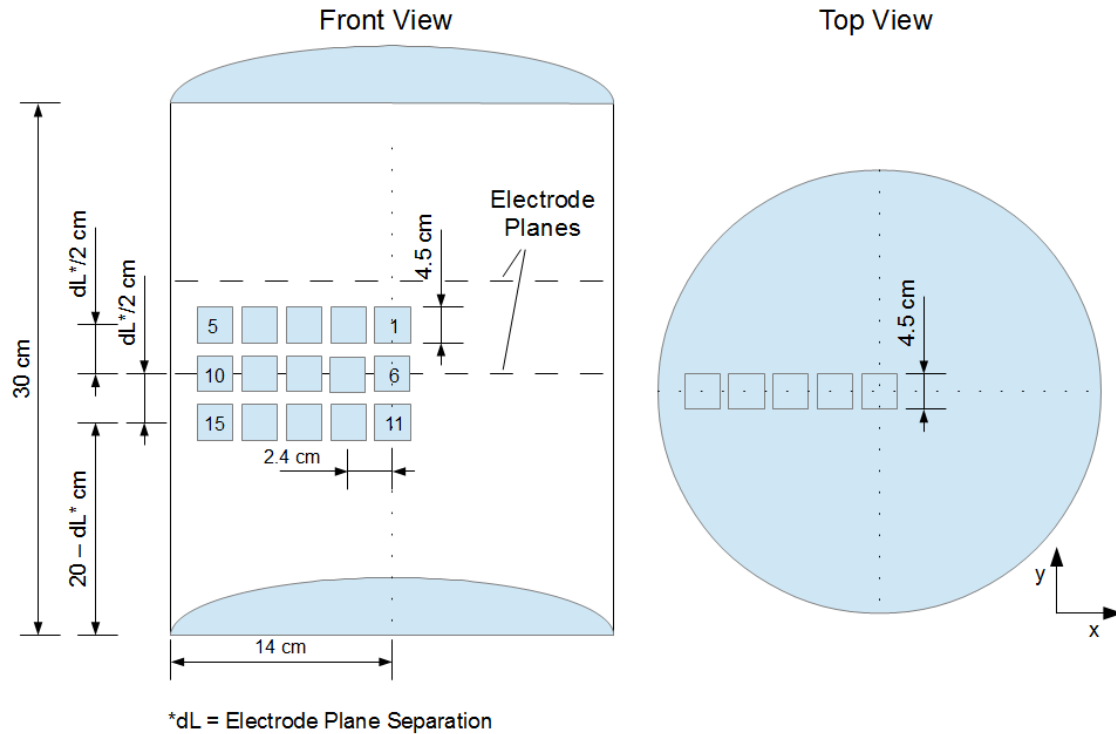


**Figure 5.3** Block Placement Locations. Blocks are placed in 15 positions over 3 levels. The first five blocks are vertically centred midway between the Electrode Planes. Level separation is set at  $dL/2$  cm, where  $dL$  is the distance between the Electrode Planes.

### 5.3 Analysis Method

#### 5.3.1 GREIT Parameters

Images are reconstructed from the measurements using the 3D GREIT algorithm described in Section 4.2.1. A cylindrical FEM is created consisting of approximately 49 000 elements. The FEM matches the physical dimensions of the tank, including the electrode placement and electrode layer separation. Electrode locations in the model are arranged to match the desired measurement pattern. A noise figure of 0.5 is used in the GREIT reconstruction. The block images are reconstructed on 7 levels, spread evenly across the height of the cylinder. The reconstruction levels are set to include the levels of the block positions.

The resulting images are then compared for image quality using the GREIT parameters. First, a target set is simulated matching the block size and positions. Second, for each block position the five GREIT parameters are calculated on each of the 7 reconstruction layers. The results are then

analyzed using the Amplitude, Resolution, and Position Error parameters, as well as the Z-Constraint Score which is described in the following section.

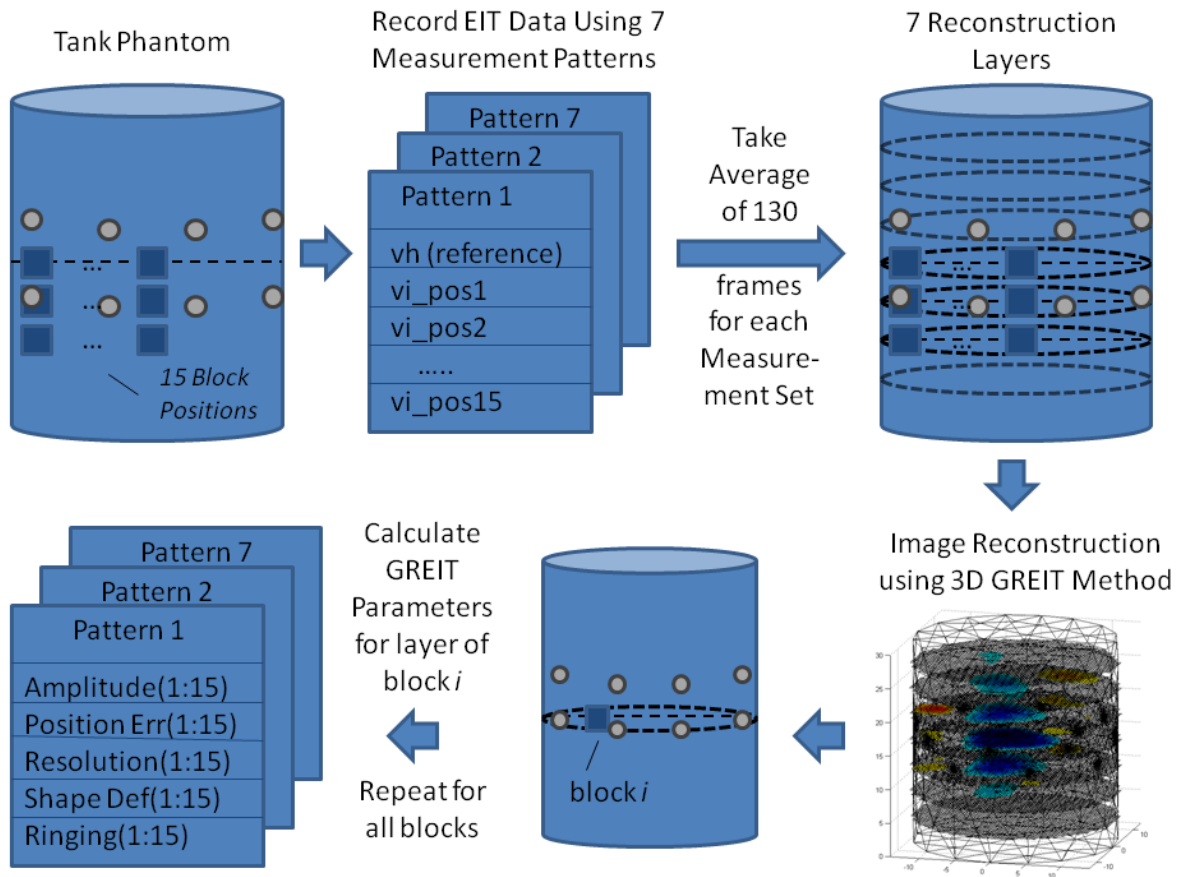


**Figure 5.4** Analysis of 7 measurement patterns using GREIT parameters. EIT measurements are taken for 15 block positions using the 7 measurement patterns. Block images are reconstructed using the 3D GREIT Method. GREIT Parameters are calculated for each block, only for the specific block layer.

### 5.3.2 Z-Constraint Score

A novel parameter has been developed in this thesis to characterize the performance of a measurement pattern in the Z-axis. This parameter provides a measure of the spread of a reconstructed object in the Z direction. The desired behaviour of the parameter is to produce small values close to the original object z-dimension. The score is defined as the distance between the upper and lower points of  $\frac{1}{4}$  Max Amplitude. This is shown in Figure 5.5. The  $\frac{1}{4}$  Max Amplitude refers to the points on the z-axis where the Amplitude first decreases to  $\frac{1}{4}$  of the maximum

Amplitude, moving away from the maximum Amplitude. The Amplitude is interpolated between layers, since there is a limited number of data points. The Z-Constraint Score is then the distance between the two  $\frac{1}{4}$  points.

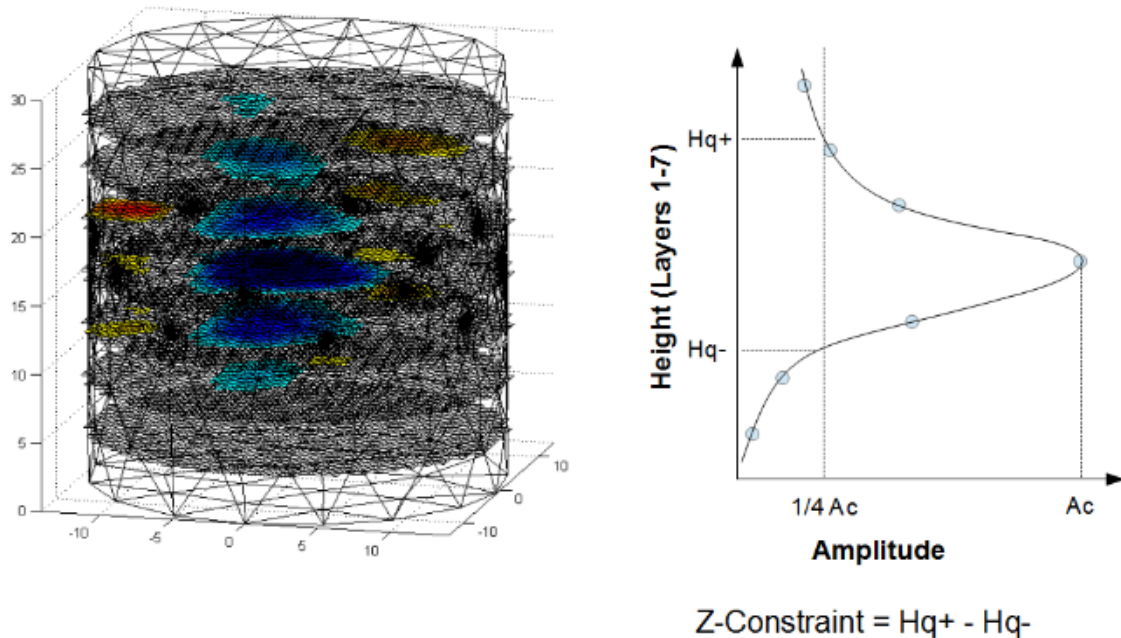


**Figure 5.5** Illustration of Z-Constraint Score. Z-Constraint is defined as the distance between  $Hq+$  and  $Hq-$ , which are the interpolated points where the Amplitude reaches  $\frac{1}{4}$  the maximum value of the Amplitude at the block-centred plane. If the  $\frac{1}{4}$  Amplitude is not met in one or both directions, the tank boundary is used.

## 5.4 Results

In order to analyze the performance of each measurement pattern in reconstructing the object set, three different approaches are taken. First, a qualitative analysis is used to compare the reconstructed images for each measurement pattern. Second, the GREIT parameters are calculated in the 2-D planes of the block position. This gives the pattern performance in the X-Y plane. Finally, the Z-Constraint Score is calculated. This score measures the ability of the pattern to detect the edges of the object in the z direction.

### 5.4.1 Qualitative Analysis

The reconstructed images are shown below in Table 1 and Table 2. The images are reconstructed using the 3D GREIT algorithm with a noise figure of 0.5. Further details are given in Section 5.3.

Table 1 shows the reconstructed images for measurements taken using a plane separation of 3.2 cm, and Table 2 shows the reconstructed images for measurements taken using a plane separation of 7.1 cm. The images for the Planar Opposite and Zigzag Opposite are not shown as the image quality is too poor to be of interest.

There are several interesting trends in the images for a plane separation of 3.2 cm. The Planar and Planar Offset patterns have difficulty discerning the object edges in the z-direction. At the centre of the cylinder, the images stretch the full axis of the cylinder. Close to the edge of the cylinder, the object is compressed to a single plane. Also, there is a spread in the images when the block is close to the edge which greatly degrades the resolution.

The Zigzag pattern shows poor edge detection in the centre as well but resolves the object well towards the cylinder edge. The pattern shows poorer resolution when the block is in the second and third planes.

The Zigzag Offset pattern is qualitatively the strongest performer. It does well to resolve the image in the z-direction, and has consistent resolution radially. However, several artifacts can be seen when the object is on the plane furthest from the centre.

The Square pattern shows decent performance with good resolution in the XY plane, but provides poor resolution in the z-direction. The images also lose their proper shape. As the object moves towards the edge, the object tail leans towards the centre.

Similar trends are seen in the images for a plane separation of 7.1 cm. However, there are significant differences in image quality when compared with results using a 3.2 cm plane separation. The Zigzag, Zigzag Offset, and Square images have significantly lower image quality, while the Planar and Planar Offset show much less difference.

The Zigzag, Zigzag Offset, and Square images see a number of detrimental effects with greater plane separation. For all three patterns there is significant noise around the circumference of the cylinder. The off-plane resolution is also reduced, especially in the centre of the cylinder. The Zigzag and Zigzag Offset patterns see an inversion in positions 6-8 and 11-13, which may be due to the mechanism used to suspend the plastic block. The Zigzag images mostly appear to be

random noise. The Zigzag Offset pattern performs the best of the three and shows the block pattern. However, the resolution is worse, especially in the centre of the cylinder and in the off-plane locations at positions 11-15.

The Planar and Planar Offset patterns are much less affected by greater plane separation. There are some differences in the resolution, especially at the edge of the cylinder where more of a block shape is seen. This may be explained by the fact that most of the measurements in the Planar and Planar Offset patterns are taken between horizontal electrode pairs, whereas the other patterns use a larger percentage of vertical or diagonal electrode pairs. Increasing the plane separation would conceivably have a much greater effect on the patterns with the greater number of vertical electrode pairs.

In the following sections, the results are shown for an electrode plane separation of 3.2 cm. This is due to the detrimental effects that a larger plane separation has on the Zigzag, Zigzag Offset, and Square patterns. Since the plane separation has a much smaller effect on the Planar and Planar Offset patterns, the results for the plane separation of 3.2 cm are considered more appropriate.

**Table 1.** Reconstructed Images of a plastic block suspended in a cylindrical tank with **3.2 cm** electrode plane spacing.

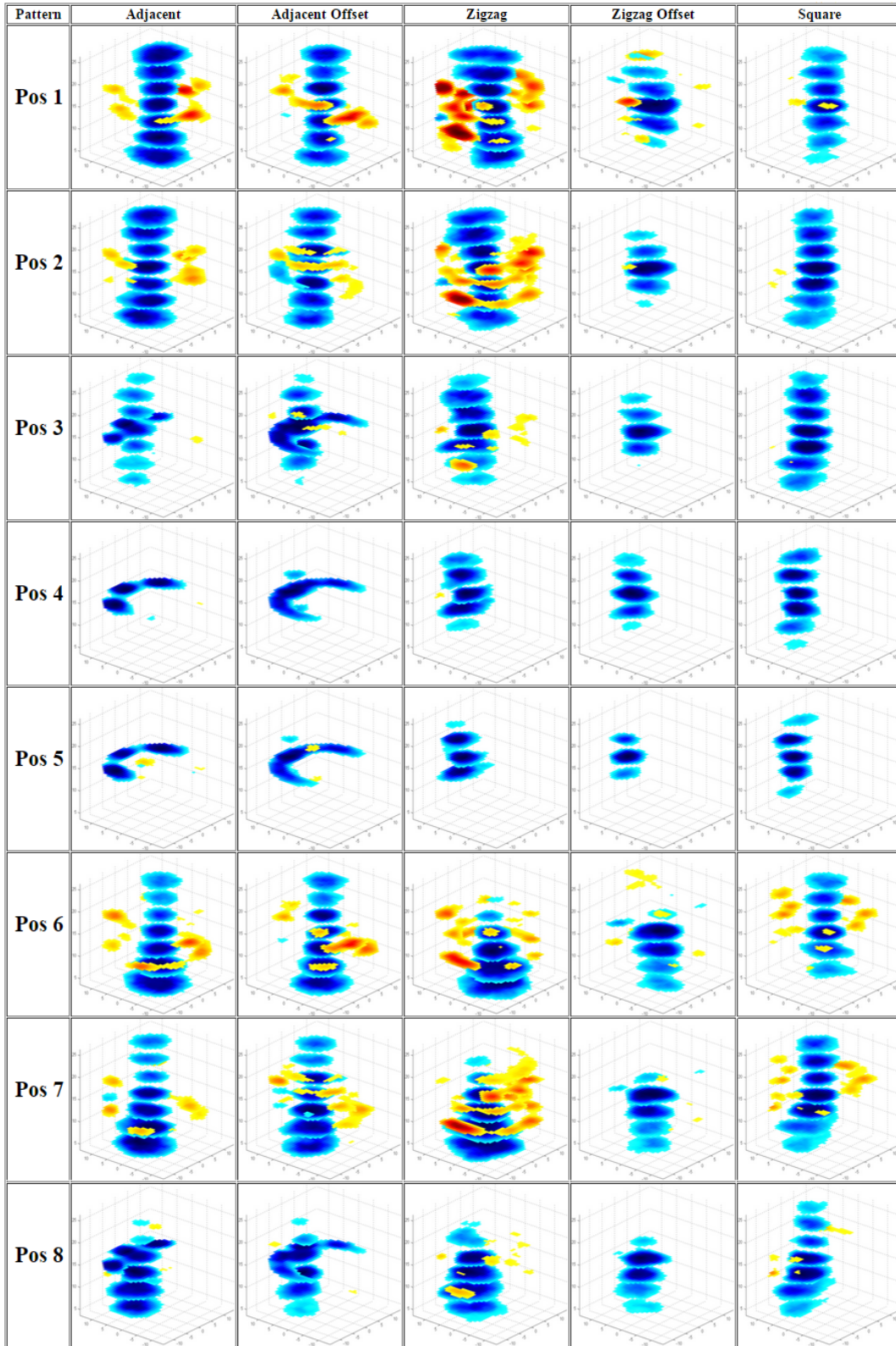


**Table 1.** (continued from previous page.)

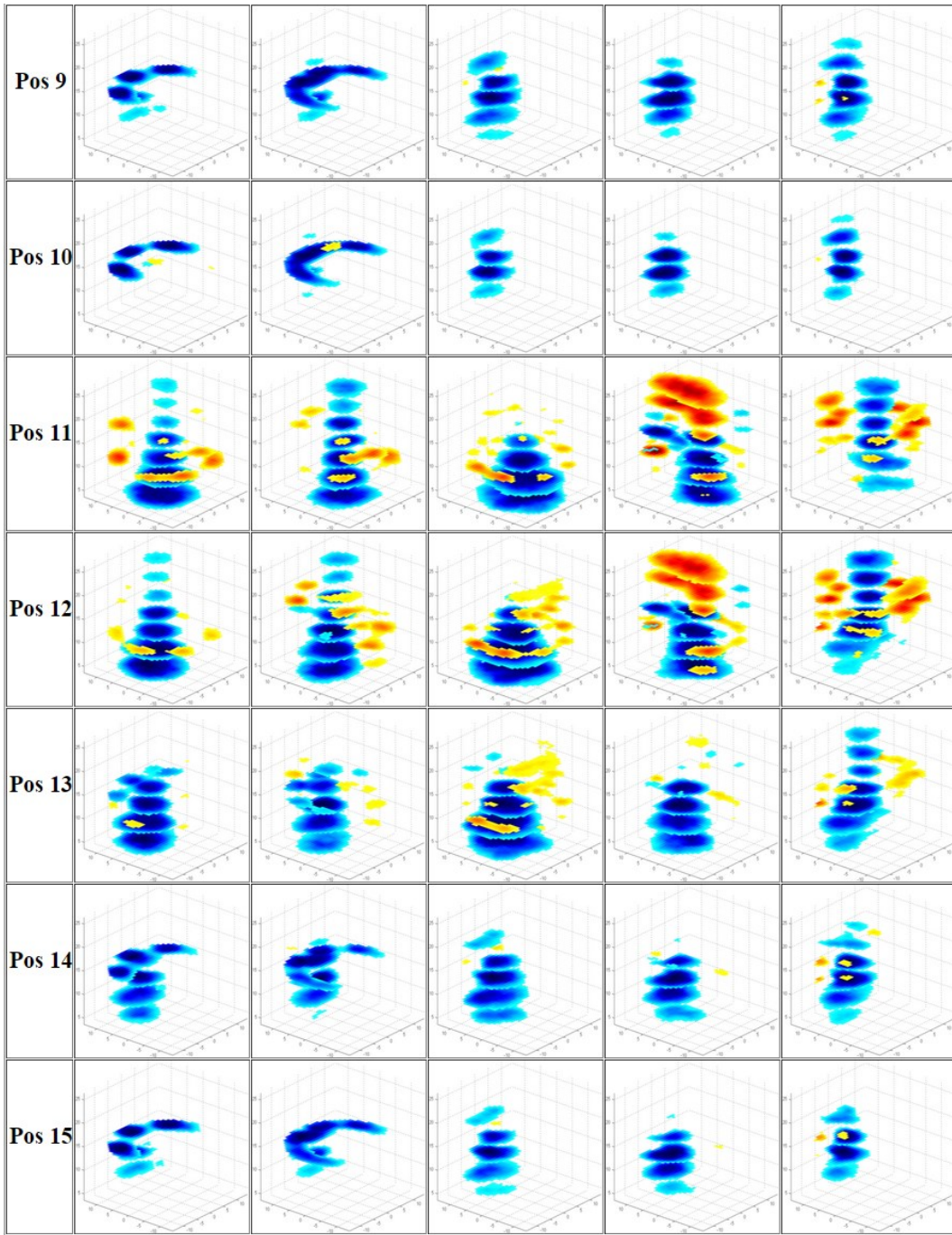


**Table 2.** Reconstructed Images of a plastic block suspended in a cylindrical tank with **7.1 cm** electrode plane spacing.

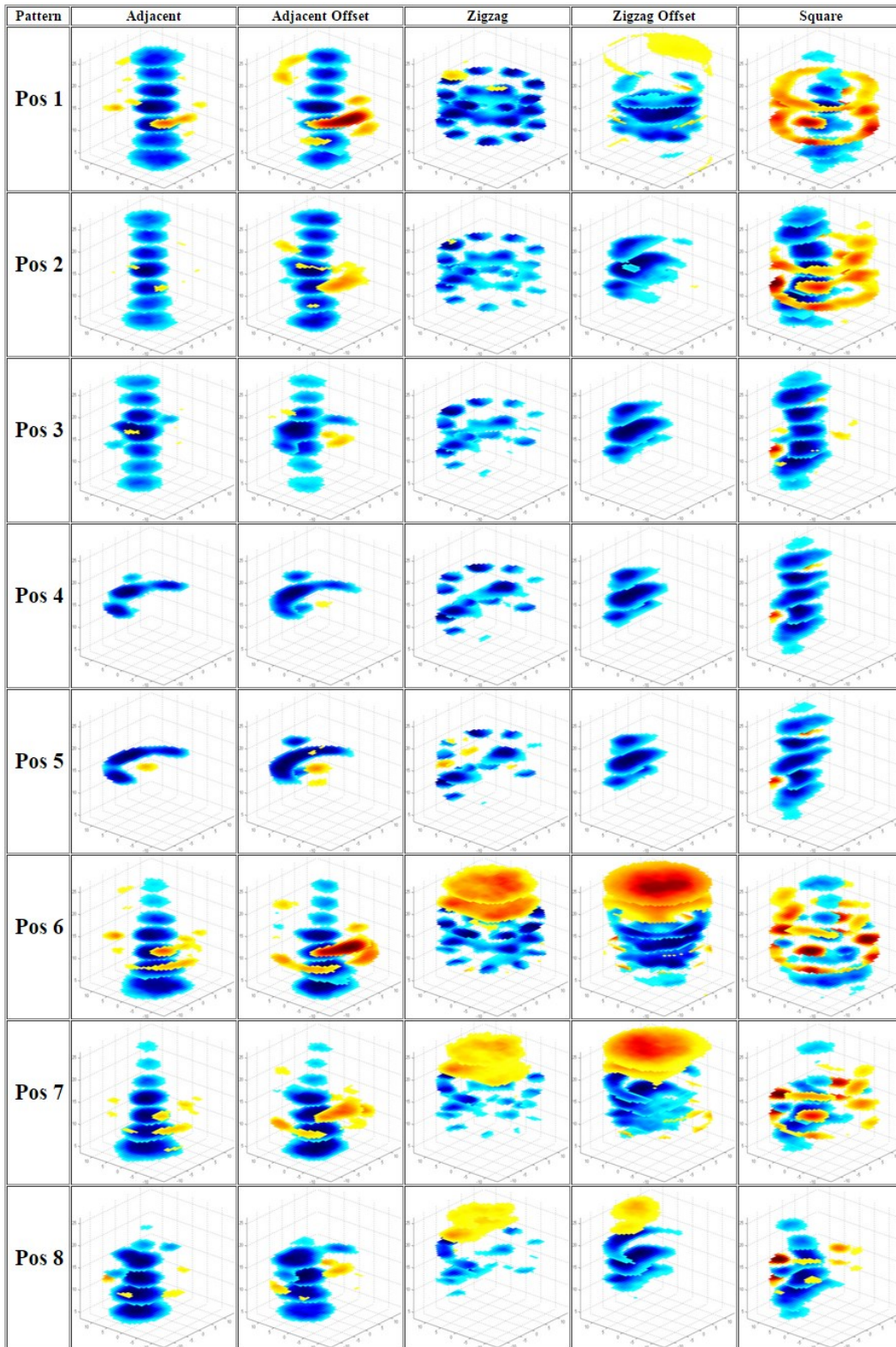
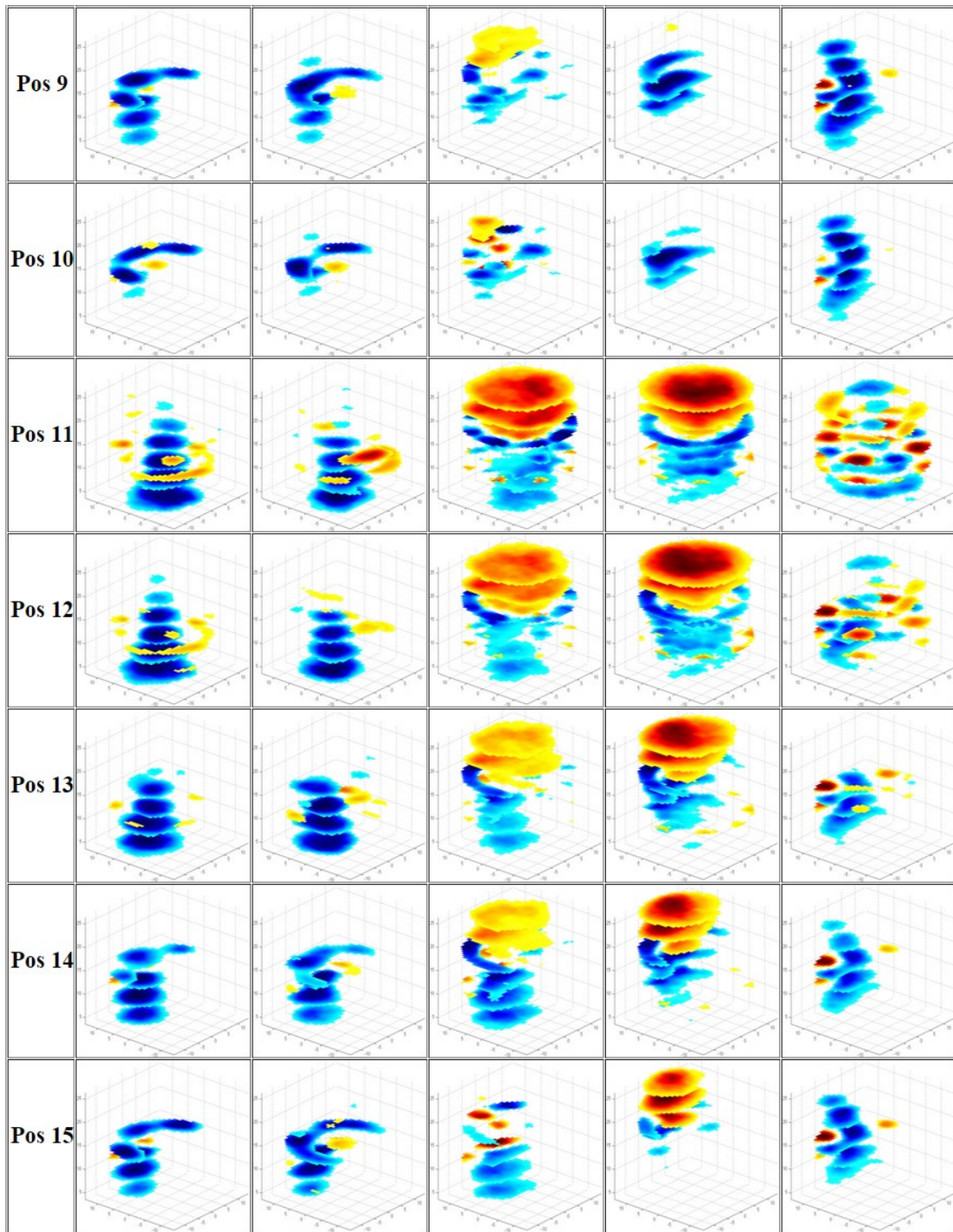
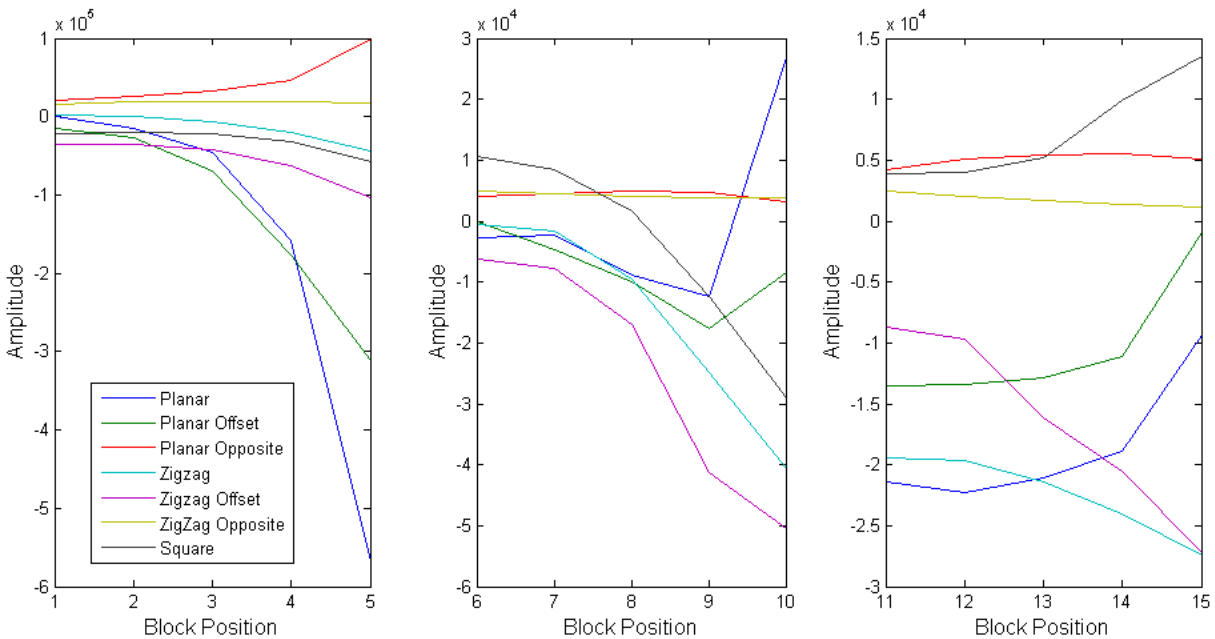


Table 2. (continued from previous page)



### 5.4.2 GREIT Parameters in the X-Y Plane

For the GREIT performance in the X-Y plane, the Amplitude, Resolution, and Position Error are considered most significant, as discussed previously in Section 4.2.1. The three parameters are plotted for each measurement pattern in Figure 5.6, Figure 5.7, and Figure 5.8 below. The results are given for the measurements taken using an electrode plane separation of 3.2 cm. Subplots are divided according to block position height. The parameter for each block position is calculated from the reconstruction layer at the vertical position of the block, as shown in Figure 5.4.



**Figure 5.6** Amplitude vs. Block Positions 1-15. Amplitude value for each block is calculated from the reconstruction layer centered on the vertical position of the block. Position numbering refers to Figure 5.3. Units are in  $\Omega/m$ .

The graphs in Figures 5.6, 5.7, and 5.8 describe the performance of each measurement pattern in the X-Y plane. The Amplitude parameter shows consistent trends, with spread towards the cylinder edge. Optimally, the Amplitude parameter value remains consistent over the radius of the cylinder. The Planar and Planar Offset patterns change more drastically towards the edge, and therefore have poorer Amplitude performance. The Zigzag, Zigzag Offset, and Square patterns are more consistent over the cylinder radius.

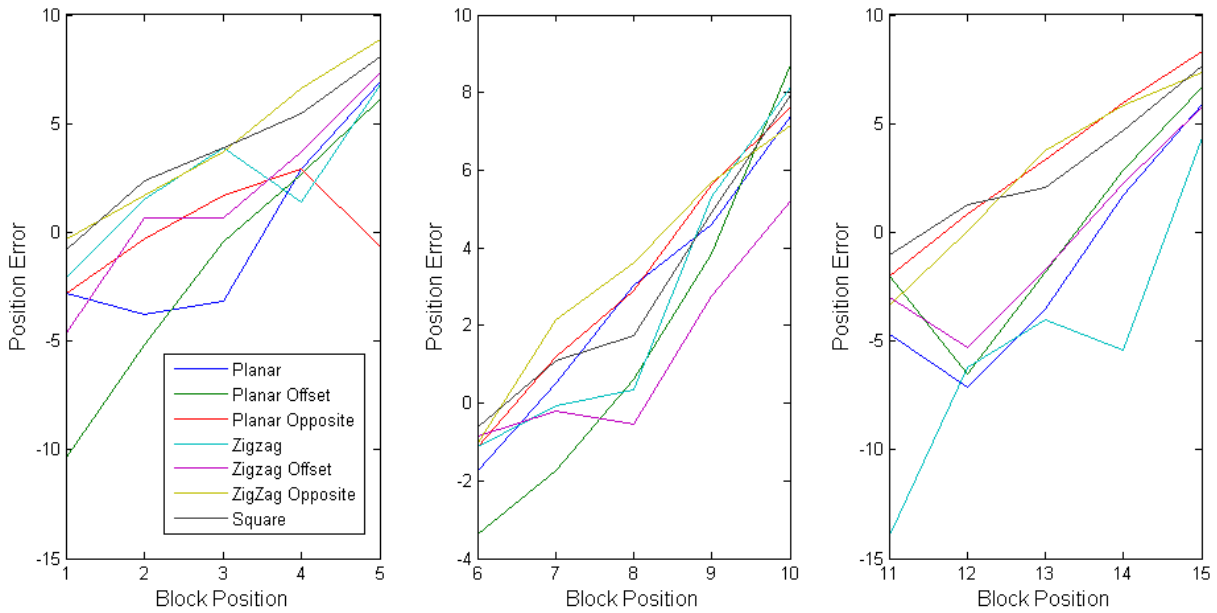


**Figure 5.7** Position Error vs. Block Positions 1-15. Position Error value for each block is calculated from the reconstruction layer centered on the block height. Position numbering refers to Figure 5.3. Units are in cm.

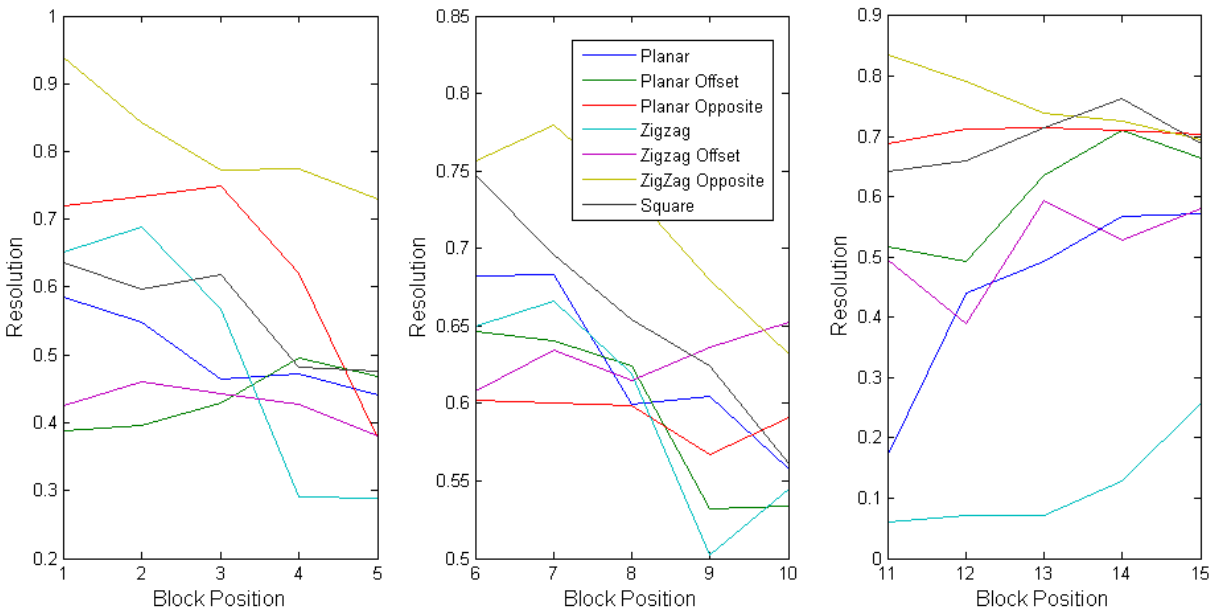


**Figure 5.8** Resolution vs. Block Positions 1-15. Resolution value for each block is calculated from the reconstruction layer centered on the block height. Position numbering refers to Figure 5.3.

The Position Error parameter is fairly consistent in the performance of all 7 patterns. A positive value indicates that the centre of mass of the image is closer to the centre than the true position, and a negative value indicates that it is further towards the edge. The general trend is an initial off-centred position for block positions 1, 6, and 11, followed by a positive trend in the Position Error as the object is moved towards the edge.

The Planar pattern specifically shows a consistent position error for block positions 1-3, suggesting a more stable reconstruction in the centre of the cylinder. The Square and Zigzag Opposite patterns have the lowest error at the centre positions. Zigzag Offset shows the lowest error overall, and Planar and Planar Offset are also strong.

The trends for the Resolution parameter are less clear. The inconsistency of the responses suggests that it is not a reliable deciding factor in separating out the best performing patterns. However, it is clear that the Planar Opposite, Zigzag Opposite, and Square patterns are the poorest performers.

The Zigzag pattern has the best performance for block positions 4-5, 9-10, and 11-15. It performs poorer in the centre regions, however. The Planar pattern is similar, with better performance for block positions 1-3. The Planar Offset and Zigzag Offset patterns perform well with the most consistent radial performance. These two patterns have the strongest performance in the centre regions in block positions 1-3 and 6-7.

#### 5.4.3 Z-Constraint

3D images can add improved object resolution in the Z-axis, as well as improved resolution in the X-Y plane by reducing off-plane influence. The Z-Constraint is an important measure for determining the ability of a measurement pattern to detect the edges of an object in the z direction. The ability of measurement patterns to resolve off-plane objects is an important feature for many 3D EIT applications.

The results for the Z-Constraint score for the image at each block position are shown in Figure 5.9 below. The desired response is a value close to the original block side length of 4.5 cm. The results are given for the measurements taken using an electrode plane separation of 3.2 cm. Only

five patterns are shown, as the Planar Opposite and Zigzag Opposite patterns produced poor quality images. In the first 5 block positions, Zigzag Offset shows the best performance, while Planar and Planar Offset have better results at the edge of the cylinder.

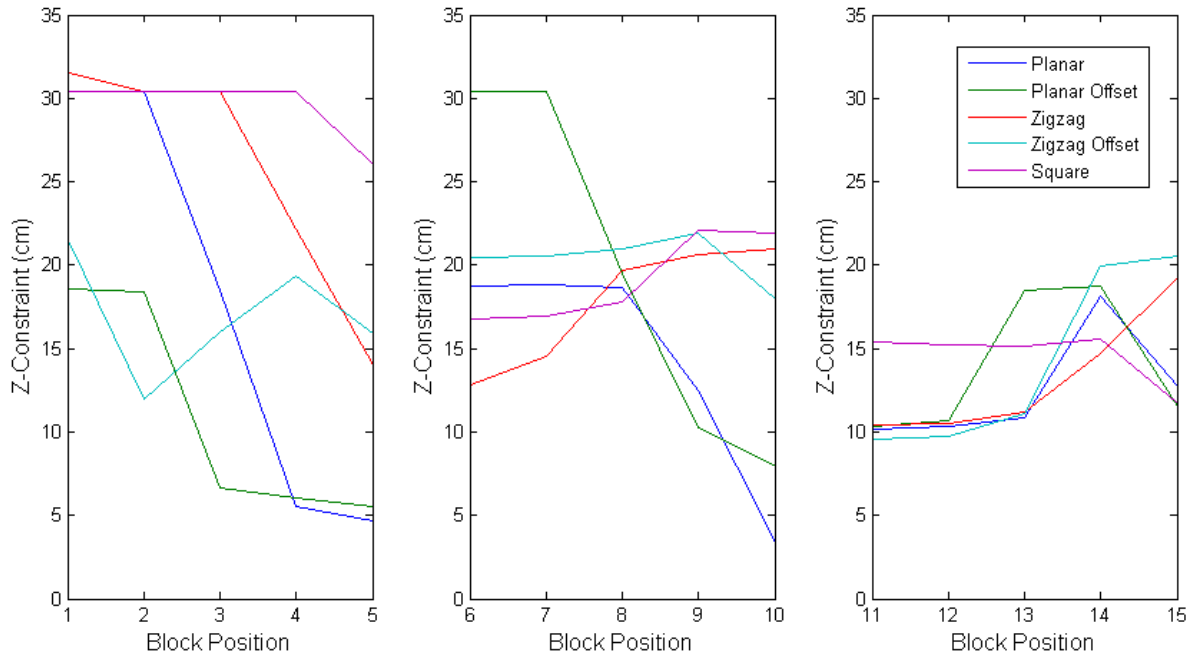


**Figure 5.9** Z-Constraint Score vs. Block Position for the 7 Measurement Patterns. Position numbering refers to Figure 5.3.

In positions 6-10 the patterns have similar performance. The Zigzag and Square patterns perform highest in the centre of the cylinder, while Planar and Planar Offset are again the strongest towards the edges. Finally, performance is similar over the last 11-15 positions, with Square having the poorest performance in the centre positions.

Overall, the Planar and Zigzag Offset patterns have the strongest Z-Constraint performance. Planar has the lowest Z-Constraint score while Zigzag Offset is the most consistent over different regions. The Square pattern shows poor performance overall but is the most uniform across the tank radius.

## 5.5 Discussion

The results from the tests performed in this experiment do not clearly indicate a single best performer, but do separate strong patterns from weaker ones. Certain patterns are shown to be more consistent than others across different tests and parameters. Other patterns are strong in certain areas and weak in others.

Table 3 and Table 4 below summarize the performance of each pattern for the different analysis methods that have been used. A '+' symbol denotes strong results with consistent performance across the image set. A '++' symbol denote significantly stronger performance than the other patterns. A '-' symbol denotes poor, inconsistent, or noisy performance in the specific category. The results in the tables were decided solely by the researcher, and are subject to the bias of the researcher. Less biased results could be obtained by gathering results from multiple 3<sup>rd</sup> party volunteers.

**Table 3.** Qualitative Results for Tank Experiment Images for the 7 Measurement Patterns

Test Parameter	Planar	Planar Offset	Planar Opposite	Zigzag	Zigzag Offset	Zigzag Opposite	Square
XY Resolution	+	+	-	-	+	-	++
XY Res at Edge	-	-	-	+	+	-	+
Z Resolution	-	-	-	+	++	-	-
Noise Artifacts	+	+	-	-	-	-	+

**Table 4.** Quantitative Results of GREIT Parameter Performance for Tank Experiment Images

Test Parameter	Planar	Planar Offset	Planar Opposite	Zigzag	Zigzag Offset	Zigzag Opposite	Square
Amplitude	-	-	-	+	+	-	+
Position Error	++	+	-	-	++	-	-
Resolution	+	+	-	++	+	-	-
Z-Constraint	++	+	NA	+	++	NA	-

The results shown in Table 3 and Table 4 show a range of performances by the 7 measurement patterns for the different analysis parameters. The Planar Opposite and Zigzag Opposite patterns are clearly the poorest performers. The Square pattern has marginally better performance, but does poorly in the quantitative tests. One positive for this pattern is the consistency in performance over the XY plane for most of the tests.

The remaining patterns show strong performance in multiple categories. Zigzag Offset stands out as the strongest pattern, while Planar, Zigzag, and Planar Offset also perform well.

#### 5.5.1 Tank Phantom Results vs. Simulations Results

There are several noteworthy observations to be made when comparing the results from the Tank Phantom experiment to the results from the simulations done in Chapter 4.

The Planar and Planar Offset patterns have large radial fluctuations in most of the Tank Phantom results, including Amplitude and Z-Constraint. Both patterns have low performance in the centre and high performance closer to the edge. In the Simulation results, the Planar and Planar Offset patterns show a spike in the radial Position Error at the centre layer for the Electrode Placement Error test, but otherwise the radial performance is as good as or better than other patterns.

The Zigzag, Zigzag Offset, and Square patterns tend to have better radial consistency in the Tank Phantom results. In the simulations, this was not always true. In Figure 4.10 Figure 4.13, the Zigzag and Zigzag Offset patterns show high Position Error towards the edge. Square shows similar performance to Zigzag and Zigzag Offset with better performance at the layer centre. The Square pattern also shows good performance in the Noise Stability results.

The reason for these discrepancies is not clear. As mentioned above, the Planar and Planar Offset patterns show a spreading effect close to the edge of the cylinder. This could in part account for the difference in performance trends.

One trend that is consistent for both Simulations and Tank Phantom results is the poor performance of the Planar Opposite and Zigzag Opposite patterns. This trend is likely due to the larger separation between both stimulation and measurement electrodes resulting in very small

measurements, which would decrease the signal-to-noise ratio. These results agree with conclusions made in [8] that the Opposite patterns are especially susceptible to noise.

Overall, the Simulations and Tank Phantom tests indicate that the Planar and Planar Offset are the strongest patterns, Zigzag and Zigzag Offset are the next strongest, Square is a weaker but stable performer, and Planar Opposite and Zigzag Opposite are the poorest performers.

### 5.5.2 Pattern Selection for Human Measurements

The results from the Simulations and Tank Phantom experiments are used to select the measurement patterns that will be used in the Human Measurement experiment described in Chapter 6. The following patterns have been selected:

- Planar
- Zigzag Offset
- Square

The reconstructed images from the Tank Phantom experiment highlight the similarities in the performance of certain patterns. The Planar and Planar Offset patterns produce similar images with similar strengths and weakness for both quantitative and qualitative parameters. The Zigzag and Zigzag Offset patterns are similarly close in their performance trends, and the Square pattern falls somewhere between the two groups.

In general, the 7 patterns can be split into four groups. The groupings are best illustrated in Figure 4.10 and Figure 4.13 in the graphs of Resolution vs. Target Position. The two 'Opposite' patterns are consistently the worst performers. The Zigzag, Zigzag Offset patterns are the next best, then Square, and then Planar and Planar Offset have the highest performance. This ordering is not present in all results but the patterns consistently separate into the 4 specific groups, as evident in the reconstructed image shown in Table 1 and 2. This suggests that the 'Aligned' and 'Offset' electrode nature are less significant than the electrode placement pattern.

Instead, the pattern groupings can be described by the ratio of horizontal to vertical electrode pairs in the stimulation pattern. The horizontal to vertical ratio clearly has a strong influence on performance in the simulation and tank phantom experiment results and it is expected that

similar effects will be seen in *in vivo* results. The Planar and Planar Offset patterns are largely horizontal measurements. The Square pattern is half horizontal and half vertical. The Zigzag and Zigzag Offset patterns are a mix of vertical and diagonal pairs, which have a greater number of vertical pairs than horizontal pairs.

When selecting the best patterns for the Human Measurements experiment, the goal is to gain insight into the performance trends of EIT measurement patterns on real human data. The similarities between the 'Aligned' and 'Offset pairs suggests that there will be little gained in comparing them in a human test. However, there may be more apparent differences in the performance of different pattern groupings. Therefore, one pattern is selected from each group.

The Zigzag and Zigzag Offset patterns show similar performance in the Simulations. The Zigzag Offset is selected over Zigzag as the strongest performer in the Tank Phantom experiment.

The Planar pattern is selected over Planar Offset in order to provide a non-offset pattern to compare with the Zigzag Offset pattern. Planar and Planar Offset have strengths and weaknesses between them. In simulations, Planar is shown to be more susceptible to noise at the cylinder edge. However, in the Tank Phantom experiment it has more consistent Position Error performance at the cylinder centre.

Finally, the Square pattern is selected as the sole member of the third group. The Square pattern has poorer overall performance in the Simulations and Tank Phantom experiment, but shows better performance consistency over the radius of the cylinder. The inclusion of this pattern rather than Planar Offset or Zigzag will increase the variety of results in the Human Measurements experiment and help to determine which performance parameters are most important when producing EIT lung images humans.

## 6 Human Measurements

### 6.1 Motivations

This chapter describes a trial of healthy human subjects where EIT and spirometry measurements are recorded during a breathing protocol in four different postures. Three EIT measurement patterns are tested and compared. The goals of this experiment are threefold:

1. Compare 3D EIT image content to spirometry lung volume measurements.
2. Observe gravitational effects on lung mechanics using reconstructed 3D EIT images, in order to underscore the value of 3D images.
3. Test performance of different EIT measurement patterns in an *in vivo* trial using results from spirometry-EIT lung volume comparisons and gravitational effects in 3D EIT images. Results will be compared with Simulations and Tank experimental results.

The main advantages of the 3D EIT approach is that it has the potential to capture regional lung activity inhomogeneities in a volume, while reducing off-plane affects thereby improving resolution. Previous sections have illustrated this advantage using simulations and tank phantom experiments. However, in order to analyze 3D EIT data recorded on human subjects, a different type of test must be used to show the ability to observe regional inhomogeneities and off-plane effects.

In the Background chapter, several papers are discussed which explore regional differences in lung mechanics when posture [30] or gravitational force [28] are changed. The results of these studies indicate that there is a gravitational effect that can be seen in transverse thoracic 2D EIT images. The study described in [30] specifically records 2D EIT measurements at several different chest heights, and observes different behaviours in different regions. A 3D image has the potential to capture this effect in a single image.

The experiment in this chapter uses different postures to alter the angle at which the gravitational force acts on the lungs. This change will theoretically alter the lung mechanics of a subject such that the lung region seeing the highest volume change shifts vertically from one posture to another. In the standing position, the dependent region, or region with the highest

gravitational force, is in the lower lungs towards the abdomen. In the decline position, the dependent region should move towards the upper lung regions.

This chapter attempts to first determine the accuracy with which 3D EIT can measure lung volume change measurements. The next step is to analyze the 3D images to observe the vertical gravitational effects on the lung activity. A successful observation of these effects would support 3D EIT as a relevant and useful lung imaging approach. Finally, the results will be analyzed in terms of the three measurement protocols in order to determine the most suitable 3D EIT measurement protocol for observing regional inhomogeneities.

## 6.2 Experimental Method

This trial was performed using healthy human subjects. Eight subjects were used in the study. Ethics approval was obtained from Carleton University to undergo this trial under Project #100712. All subjects signed a Letter of Consent which permits the anonymous storage and publishing of the gathered data. Exclusion criteria for subjects included any vascular or respiratory medical conditions, as well as habitual smoking. Subjects were male between the ages of 24 and 45.

In this experiment, each subject performed a breathing protocol, described in Figure 6.5, for 60 seconds while 3D EIT measurements and spirometry measurements were simultaneously recorded with the subject positioned in four different postures. Figure 6.1 shows a breakdown of the procedure. The measurements for each posture were repeated using three different EIT measurement patterns: **Planar**, **Zigzag Offset**, and **Square**. These patterns were selected based on the results of the Simulation and Tank Phantom experiments. EIT data were acquired by placing 16 electrodes around the upper torso against the skin, as shown in Figure 6.2 and Figure 6.3. Measurements were then taken using the Goe-MF II EIT device and the iWorx-214 Spirometer.

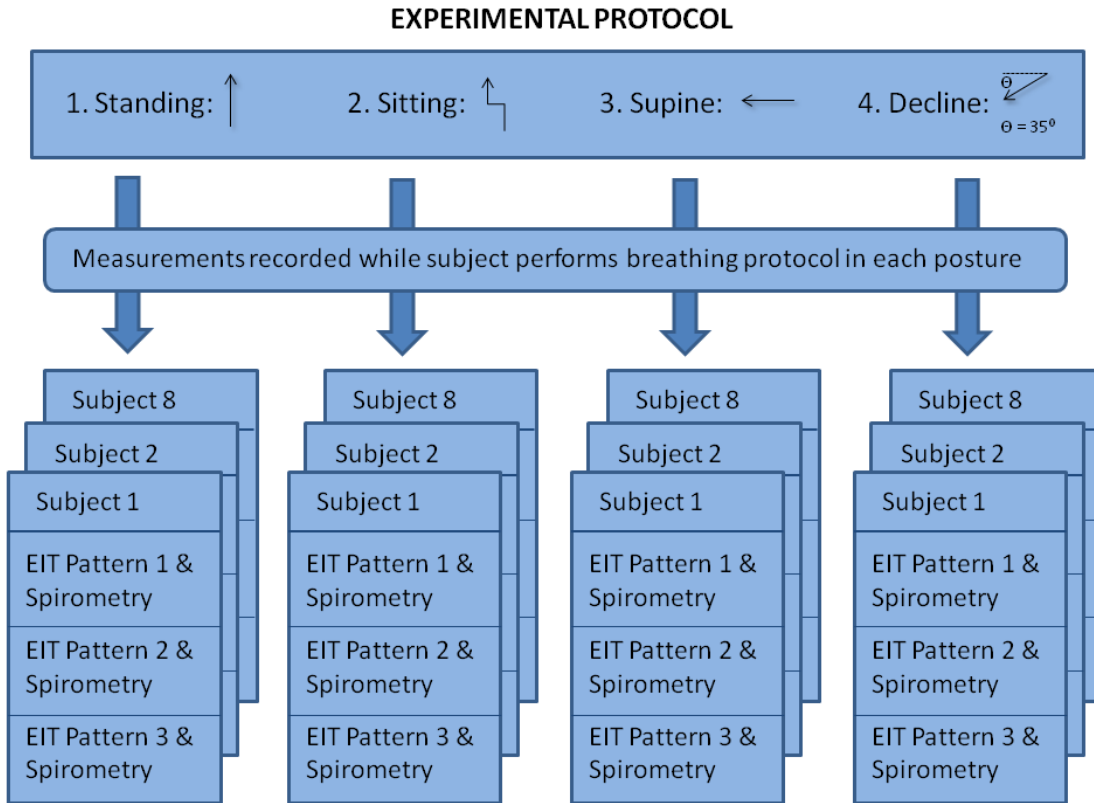


**Figure 6.1** Experimental Protocol for Human Measurements Experiment. Subjects complete a breathing protocol while EIT and Spirometry measurements are recorded. The process is performed with the subject in four different postures. For each posture, the protocol is repeated using 3 different 3D EIT Measurement patterns: *Planar*, *Zigzag Offset*, and *Square*.

Electrodes were placed on the subject in 2 rings. The lower ring was placed 4 cm above the base of the sternum and the second ring was placed 4 cm above the first ring. The 8 electrodes in each ring were placed equidistant around the thorax as shown in Figure 6.2. The front-facing electrodes, which are electrode 3 and 11 for the Planar pattern, were placed at the horizontal centre of the chest and electrode as shown in Figure 6.4. The rear-facing electrodes, which are electrodes 7 and 15 for the Planar pattern, were placed on the centre of the back on the spine. For the offset pattern, the upper ring electrodes were shifted clockwise by half the inter-electrode distance, as shown in Figure 6.3. A ground electrode was placed under the ribcage on the front right side.

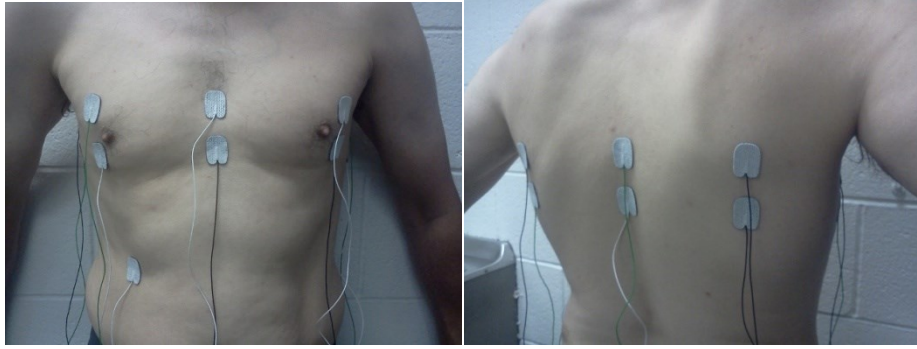


**Figure 6.2** EIT Electrode Placement on male subject. Pattern shown is the *Aligned 2* layer 16 electrode pattern with ground.

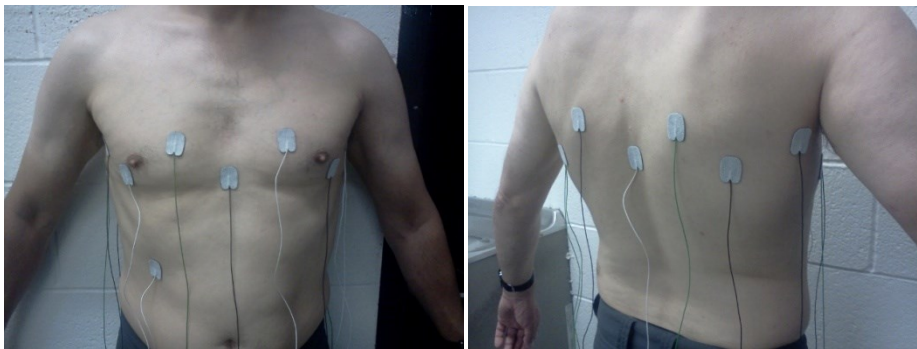
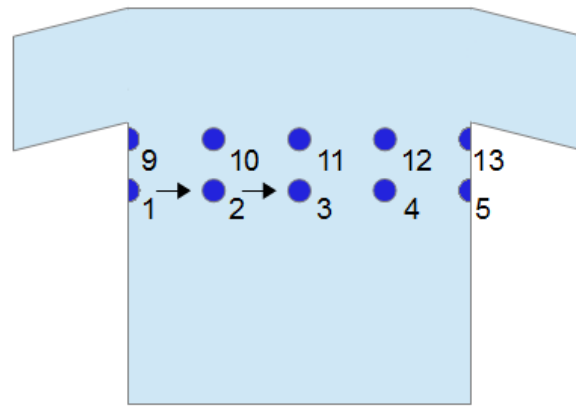


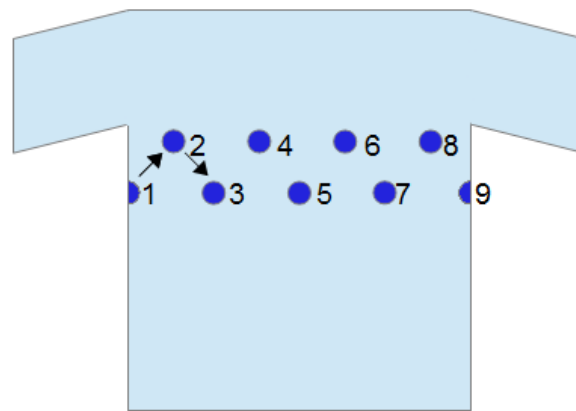
**Figure 6.3** EIT Electrode Placement on male subject. Pattern shown is the *Offset 2* layer 16 electrode pattern with an additional ground electrode placed below the ribcage.

The breathing protocol that was followed during the measurements had a duration of 60 seconds. The subject started with two tidal breaths beginning with inhalation, and then performed vital capacity (VC) breathing for the remainder of the 60 seconds at their own pace. This is shown below in Figure 6.5. Tidal breathing is the normal shallow breaths taken by an individual at rest. During the subsequent period of VC breathing, the subject inhaled as completely as possible and then exhaled as completely as possible. The tidal breathing is used to synchronize the EIT and spirometry signals during analysis, as well as to give the subject time to get comfortable before starting the VC breathing.

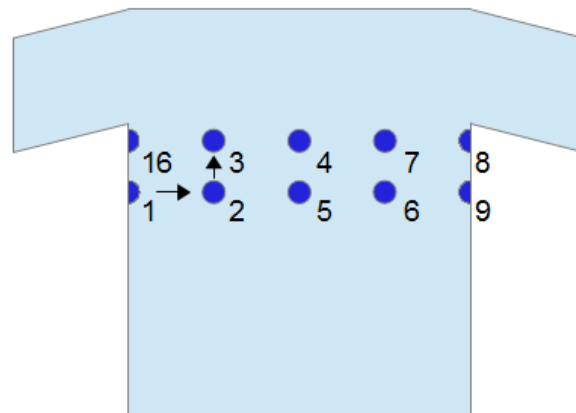
The subject performed the breathing protocol in four different postures, as shown in Figure 6.1. The four postures were **standing**, **sitting**, **supine (lying)**, and **decline**. The declination for the decline posture was set to 35 degrees, and was achieved using a decline workout bench. The postures



PLANAR



ZIGZAG OFFSET



SQUARE

**Figure 6.4** Electrode positioning and numbering electrodes attached to torso for the Planar, Zigzag Offset, and Square 3D EIT Measurement patterns.

were selected in order to vary the gravitational influence on lung mechanics in the vertical direction.

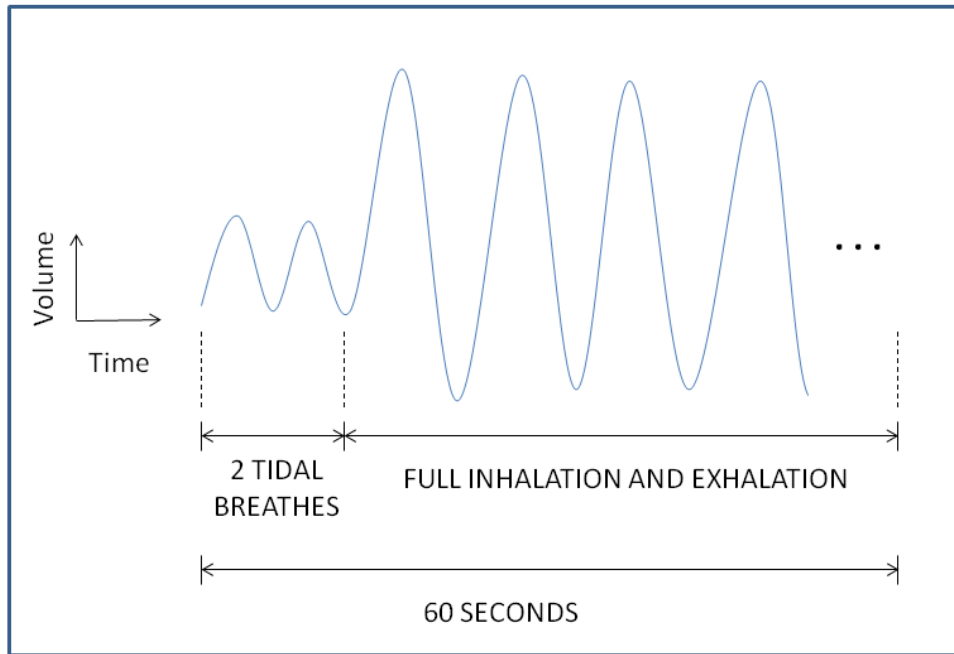


**Figure 6.5** Breathing Protocol during which EIT and Spirometry measurements are recorded.

The spirometry measurements were acquired using the iWorx-214 physiological data acquisition system. The system uses the software *LabScribe 2* to display and capture the data. The iworx-214 system captures pressure measurements and converts them into change in volume, and provides both values as outputs. The data acquisition rate was set to 200 samples/second.

The EIT measurements were taken using the Goe-MF II device with identical settings as those in Section 5.1. The device is run using the software *SCIEITv8*. The software has a built-in feature which displays the average impedance seen at each electrode. This feature was used during the trial to detect electrodes with higher than normal impedance. The common causes for high impedance were that an electrode was out of position or had become partially or fully detached from the skin.

## 6.3 Analysis Method

### 6.3.1 Spirometry vs. EIT

The data from the healthy human trial are analyzed in several ways. The first approach is to compare the global EIT amplitude value to the spirometry volume measurements. The goal is to determine the accuracy with which EIT is able to measure lung volume changes by comparing it to lung volume change measurements from a spirometer.

In order to compare the EIT images to the spirometry data, each data set is reconstructed using the 3D GREIT method, described in Chapter 3, to generate a time series image set. The reconstruction method uses difference imaging, where image reconstruction is based on the change in conductivity between a data measurement and a reference measurement. This differs from absolute imaging, where image reconstruction is based on a single measurement. The reference image for each data set is calculated by averaging 5% of the images which have the lowest total pixel amplitude. These images represent the average measurement while the subject is exhaling. The resulting difference images then represent increase in volume from residual volume (complete exhalation).

A global amplitude signal is calculated from each time series image set. This is done by calculating the sum of the pixel values in each image of the image set, resulting in a time series vector. The global amplitude signal is then compared to the spirometry lung volume measurement.

#### 6.3.1.1 Correlation and Root Mean Square Error

The EIT data are first compared to the spirometry data by calculating the correlation between the two measurement sets. The correlation represents the interdependence between the two measurements and provides a means of determining the ability of the 3D EIT images to describe changes in lung volume. The correlation coefficient for the adjusted spirometry data and the EIT global amplitude data is calculated using MatLAB's *corrcoef* function. The data are then averaged over all subjects for each position and for each EIT measurement pattern.

The EIT data are then compared to the spirometry data by calculating the Root Mean Square Error (RMSE) between the measurement sets. This gives an estimate of the error in the EIT signal

in capturing the lung volume change in comparison with the spirometry method. The data are again averaged over all subjects for each position and for each EIT measurement pattern.

### *6.3.1.2 Spirometry Signal Conditioning*

In order to compare the two measurements, some signal conditioning is required. The data acquisition rates for the EIT device and the spirometer are different by a factor of  $\sim 16$ . A peak-matching algorithm is used to align the spirometry and EIT signals and to select a spirometry data point to correspond with each EIT measurement. The selection rate is approximately 1 in 16 spirometry measurements. Finally, the data representing the two tidal breaths are dropped so that only the VC breaths are used in the calculations.

The spirometry data show significant drift during the breathing protocol. The source of spirometry drift may be due to a number of factors. First, if the subject does not form a perfect seal on the spirometer mouthpiece, escaping air will not be measured and will lead to errors in the measurements. However, drift was still seen during testing when a good seal was ensured. Another possible source of drift is a problem with calibration of the sensor in the spirometer. Additionally, there is an integration function to convert the data from the raw pressure values to the volume values. An offset in the pressure data would cause drift in the volume data.

An example of the drift correction process is shown in Figure 6.6. The original spirometry volume data is shown as the solid blue line. The sinusoidal nature of the volume changes can be seen. A 6<sup>th</sup> order polynomial curve is fit to the spirometry data. The polynomial curve is then subtracted from the spirometry data in order to remove the drift. The adjusted spirometry trend is shown in the dotted blue line. The trend is now zeroed and retains the sinusoidal nature. The drift correction process will be a source of error in the Correlation and RMSE results due to imperfect approximation of the polynomial line to the drift.

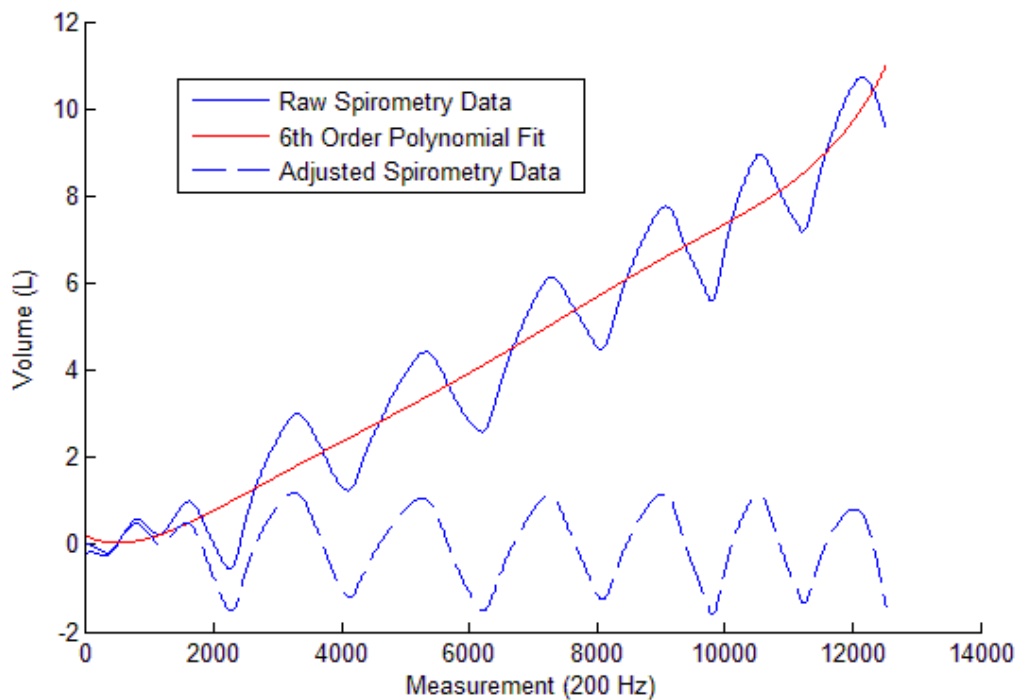


**Figure 6.6** A graph showing a 6<sup>th</sup> order polynomial line (solid red line) fit to the raw spirometry data (solid blue line). The polynomial line is subtracted from the raw data to remove drift, which result in the adjusted spirometry data (dashed blue line). Measurements are recorded at 200 Hz.

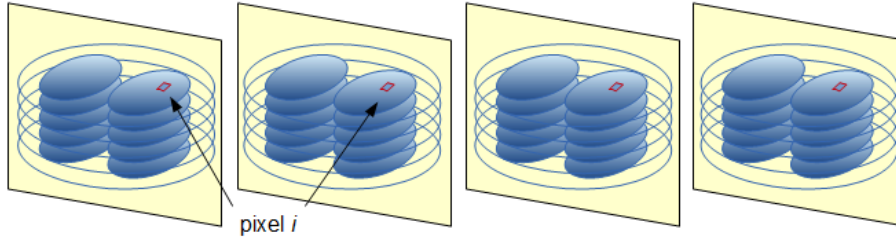
### 6.3.2 Vertical Regional Thoracic Effects

The next goal of this chapter is to quantify gravitational effects in the 3D EIT images. The ability of 3D EIT to capture regional inhomogeneities in a volume sets it apart from 2D EIT. The 3D EIT images are analyzed by layer in order to observe changes in lung activity in the vertical direction in response to change in posture.

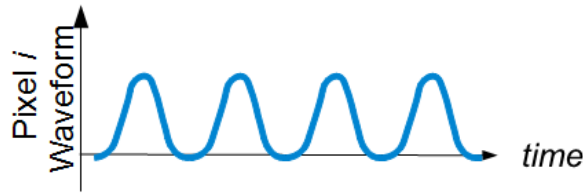
#### 6.3.2.1 Functional Electrical Impedance Tomography Images

The images are analyzed by creating functional EIT (fEIT) images. This approach is adapted from the method used by I. Frerichs in [28] to analyze EIT recordings for gravitational effects. The steps used in this work to generate fEIT images are shown in Figure 6.7. An fEIT images is useful in that it is a single image which represents a specific feature of the lung mechanics during breathing protocol.

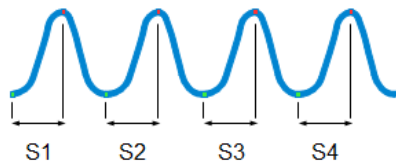
### 1. Reconstruct EIT Dataset using 3D GREIT Method



### 2. Time series vector for each pixel $i$



### 3. Segmentation by Inhalation



### 4. Feature Calculation

Features are calculated for each segment and averaged.

1. Amplitude Difference  $f1 = \Delta Amp$
2. 3<sup>rd</sup> Order Polynomial Line Fit  $[f2 \ f3 \ f4] =$  polynomial coefficients  $[a0, a1, a2]$

### 5. fEIT Images

An image is produced for each feature using the feature value of each pixel.

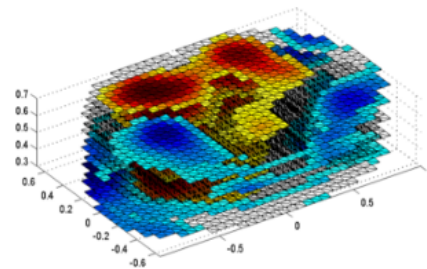


**Figure 6.7** Steps to produce functional EIT (fEIT) images from a time series data set. The data are reconstructed using the 3D GREIT method. Each pixel time series vector is segmented by inhalation, and four features are extracted from each segment and averaged. The first is the Amplitude Difference and the following three are the coefficients of a 3<sup>rd</sup> order polynomial fit to the segment line. Finally, 4 fEIT images are produced, one for each feature, using the feature values for each pixel.

For each EIT image set, features are extracted specifically from the inhalation curves in each image set. The inhalation curves are determined by segmenting the global amplitude signal, as described in Section 6.3.1, of the EIT image set. The maximum and minimum peaks in the signal correspond with full inhalation and full exhalation respectively. The inhalation segment is selected as the data from a minimum to a maximum point in the global amplitude signal.

Figure 6.8 shows an example of this process with real data. The two initial tidal breaths are removed from the data set. Occasionally, segments considered to have low quality are also discarded. This was generally due to large drift in the spirometry signal which could not be sufficiently removed by the drift correction process.

Once the inhalation curves are segmented are selected, four features are calculated for each pixel over the inhalation curve. The change in amplitude during inhalation for each individual pixel is taken as the first feature. A third order polynomial is then fit to the inhalation curve of each pixel, and the coefficients are taken as an additional three features. The average feature value is then calculated over all inhalation segments for each pixel.

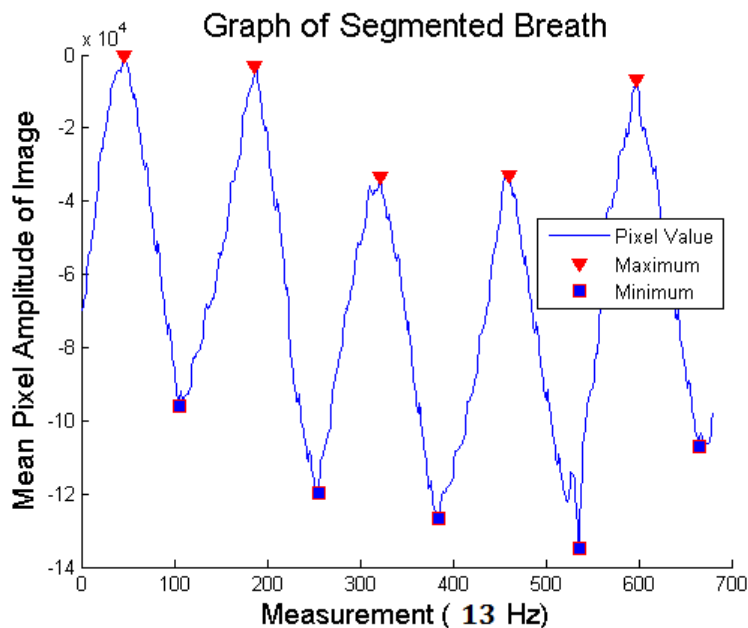


**Figure 6.8** A graph of the mean of the pixel amplitude from an EIT image set. The segment from a minimum (blue) to a maximum (red) represents one inhalation. The two initial tidal breaths have been removed, as well as data following the final peak. Measurements are taken at 13 Hz.

The average feature value for each pixel is then used to produce an fEIT image. This results in a total of four fEIT images, each representing a feature which in turn describes an aspect of lung function. Figure 6.9 shows an example of four fEIT images generated from a measurement set taken with a subject in the *sitting* posture using the *Planar* measurement pattern.

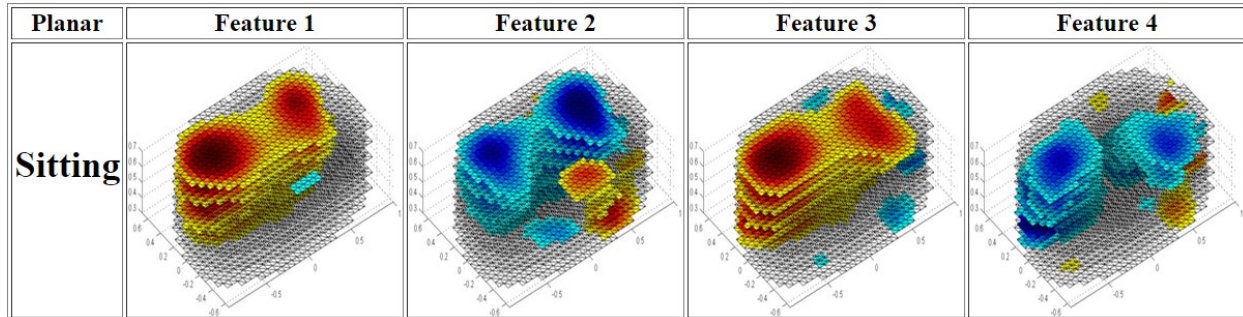


**Figure 6.9** A set of four *functional EIT* (fEIT) images from a measurement set representing features  $f_1$ ,  $f_2$ ,  $f_3$ , and  $f_4$ . The subject is in the *sitting* posture with measurements taken using the *Planar* measurement pattern.

The process results in four fEIT images representing different aspect of the lung mechanics for a given posture and measurement pattern. The images can then be directly analyzed layer by layer in order to determine the presence of vertical gravitational effects.

### 6.3.2.2 *fEIT Analysis Method*

The functional EIT images are analyzed to determine whether vertical gravitational effects can be observed in 3D EIT images with the subject in different postures. The anticipated effect is for there to be a vertical shift in the region of highest lung activity. The change in posture from standing to sitting to lying to decline causes a change in the direction of the gravitational force, which shifts region of higher activity. While standing, a subject will have greater activity in the lower lung regions. In the decline position, a shift in activity towards the upper lung regions is expected.

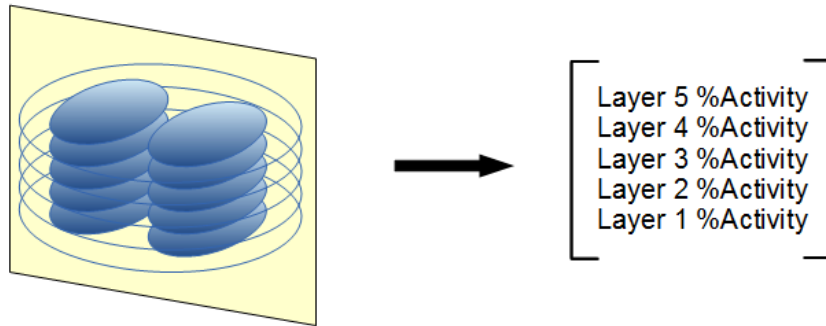
In order to analyze the lung fEIT images for vertical gravitational effects, a novel parameter termed %Activity is calculated. This parameter represents the total pixel amplitude for each layer of the fEIT image and is given by the following equation:

$$\%Activity_i = 100 \times Nq_{max_i} / \sum Nq_{max} \quad (17)$$

where  $Nq_{max_i}$  is the number of pixels on a given layer  $i$  that are greater or equal to than  $\frac{1}{4}$  the maximum pixel value of the image. The value is then normalized by dividing  $Nq_{max_i}$  by  $\sum Nq_{max}$  which is the total number of pixels in the image greater or equal to the  $\frac{1}{4}$  maximum pixel value. Therefore,  $\%Activity_i$  gives the percentage of feature activity occurring at a given layer  $i$ .

For each subject and measurement pattern, the %Activity of each fEIT image is plotted vs the reconstruction layer, as shown in Figure 6.10. A plot is produced for each posture. The slope of the trend in each plot is calculated. The slope gives a rough estimate of the activity trend across the layers of the image. Finally, the slopes are averaged for all subjects for each measurement pattern and posture.

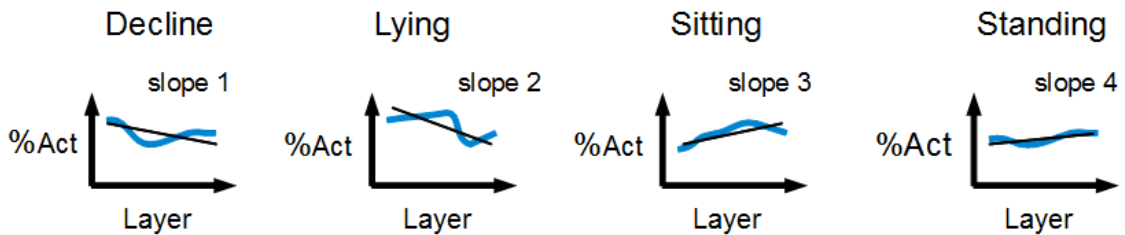
### 1. Calculate % Activity of each layer



$$\% \text{ Activity} = \frac{Nq_{\max_i}}{\sum Nq_{\max}}$$

where  $Nq_{\max_i}$  is the number of pixels on layer  $i$  greater than  $1/4$  the maximum pixel value of the image.

### 2. Calculate slope of %Activity vs. Layer for each Posture for a given subject and measurement pattern



### 3. Plot Slope vs. Posture

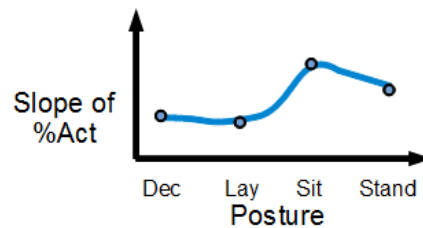


**Figure 6.10** Steps involved in fEIT analysis method of vertical gravitational effects. First, the %Activity is calculated for each layer. Second, the slope of the %Activity vs. Layer plot is calculated for each posture. Third, the slopes are plotted against Posture to illustrate the change in lung behaviour due to posture.

## 6.4 Results

### 6.4.1 Correlation

The results for the Global EIT Amplitude-Spirometry Correlation analysis are shown in Figure 6.11. The trends indicate a strong correlation for most measurement sets. Only Subject 3 and Subject 7 have correlations lower than 0.75. The overall strong correlation between the two data sets indicates that the 3D EIT images are capable of measuring changes in lung volume.

It should be noted as well that there are no results for Subject 3 in the decline posture, as the equipment was not available at the time of measurement. There are also several low quality spirometry data sets. Several measurements for Subject 7 have very high drift and a higher order polynomial (~12) is used to retrieve some useable results. The spirometry data for Subject 7 - Zigzag Offset - decline and for Subject 5 – Planar – sitting are unusable and have been withheld from the results.

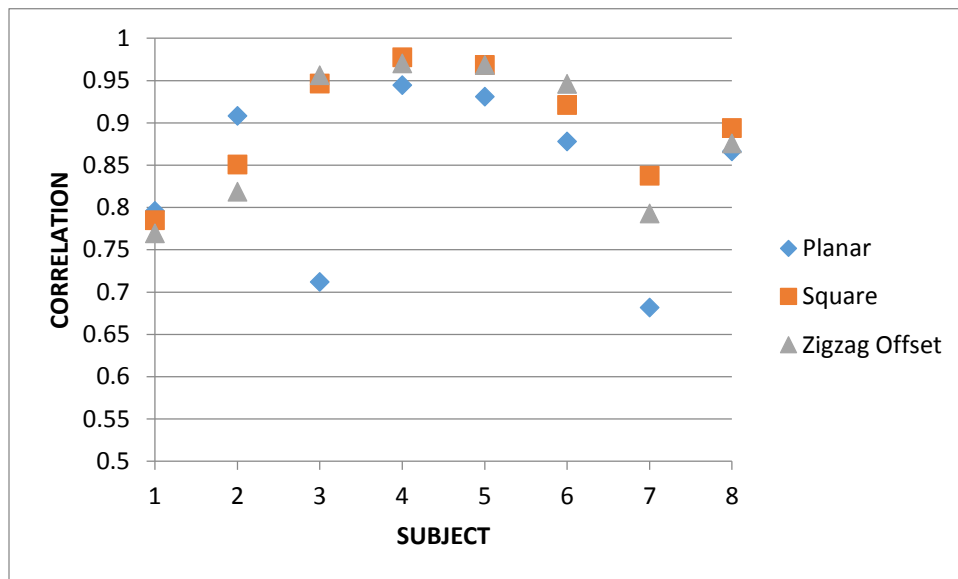


**Figure 6.11** The correlation between Global EIT Amplitude and Spirometry Lung Volume for each subject averaged across all 4 postures. Average correlation for all subjects is shown in the table for each measurement pattern.

The results are summarized by pattern in Table 5 and present some differentiation in pattern performance. The Planar pattern has the lowest correlation at 0.84, while the Square and Zigzag Offset patterns are quite similar at 0.898 and 0.887 respectively. The Planar pattern also has the

highest standard deviation, suggesting a lower reliability than the other patterns. However, the difference in correlation between the patterns is not statistically significant.

**Table 5.** Summary of Correlation results by pattern.

Parameter	Planar	Zigzag Offset	Square
Mean Pattern Correlation	0.840	0.887	0.898
Std. Dev.	0.139	0.110	0.088

#### 6.4.2 Root Mean Square Error

The next method of comparing the Global EIT Amplitude to the Spirometry Volume is to calculate the Root Mean Square Error (RMSE) between the signals. The normalized results are shown in Figure 6.12, and the results for each pattern are summarized in Table 6. Similar to the correlation results, there is a wide range of RMSE values from subject to subject. In most cases, the difference in the results for each pattern is quite small. The Planar pattern again has the poorest performance but the results are not significant.

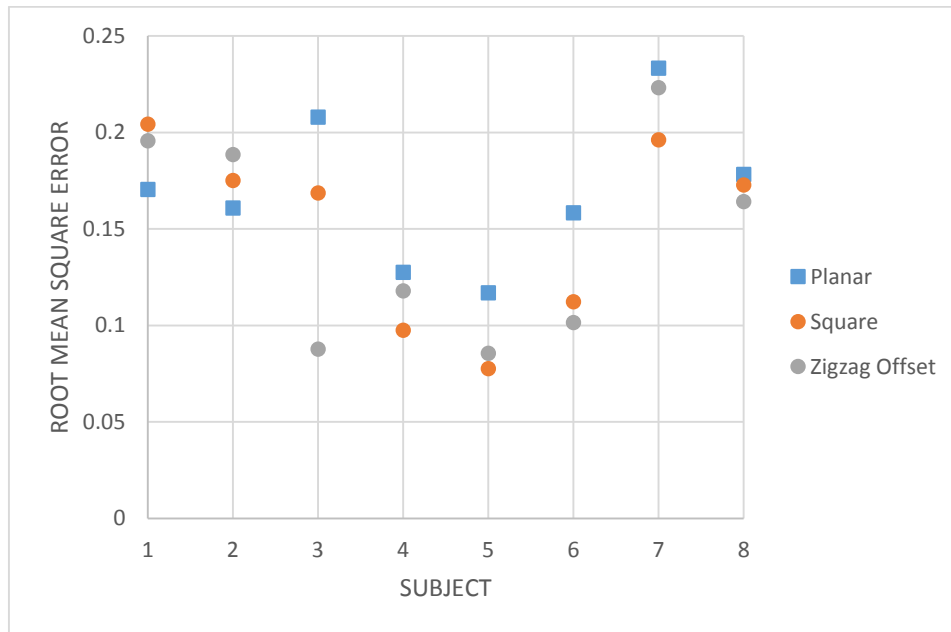


**Figure 6.12** Root Mean Squared Error of Spirometry Lung Volume vs. Global EIT Amplitude for each subject averaged across all 4 postures. Average RMSE for all subjects is shown in the table.

**Table 6.** Summary of RMSE results by measurement pattern.

<b>SUMMARY</b>	<b>Planar</b>	<b>Zigzag Offset</b>	<b>Square</b>
Average Pattern RMSE	0.169	0.150	0.145
Std. Dev.	0.038	0.048	0.054

### 6.4.3 Vertical Gravity

For each subject, measurement pattern, and posture, 4 fEIT images are generated. The full set of fEIT images is included in Appendix A. In order to analyze the images, two basic approaches are taken. First, a qualitative approach is taken to summarize differences in performance by fEIT image type, measurement pattern, and posture for the 8 subjects. Second, the fEIT images are analyzed by layer to quantify changes in vertical lung activity.

#### 6.4.3.1 Functional EIT Images

The set of fEIT images for each subject consists of 4 fEIT images for each measurement pattern and each posture, corresponding to the 4 features that have been used to generate the images. This gives a total of 36 images per subject. For each fEIT image type, the images are grouped by measurement pattern.

The fEIT images provide a much improved representation of the characteristics of the breathing trends. The time series measurements of the subject breathing produced a set of around 780 images. This is a large set to analyze. Many of the image sets also consist of individual images with poorly defined lung regions. However, an fEIT image provides a spatial summary of temporal behaviour. A single fEIT image is able to represent a feature of the time series data set, and the lung behaviour becomes much simpler to interpret and understand.

The difference between the raw time series EIT images and the fEIT images can be quite large. Figure 6.13 shows a set of images taken from a subject in the Standing posture using the Planar measurement pattern. In the first set, every 10<sup>th</sup> image from a full inhalation and exhalation is displayed and represent one full VC breathing cycle. There is a consistent shift from a positive column on the right side of the image to a negative column on the left side during inhalation,

such that when one column is decreasing the other is increasing, and the reverse behaviour is shown during exhalation. However, the individual images do not show a well-defined lung region.

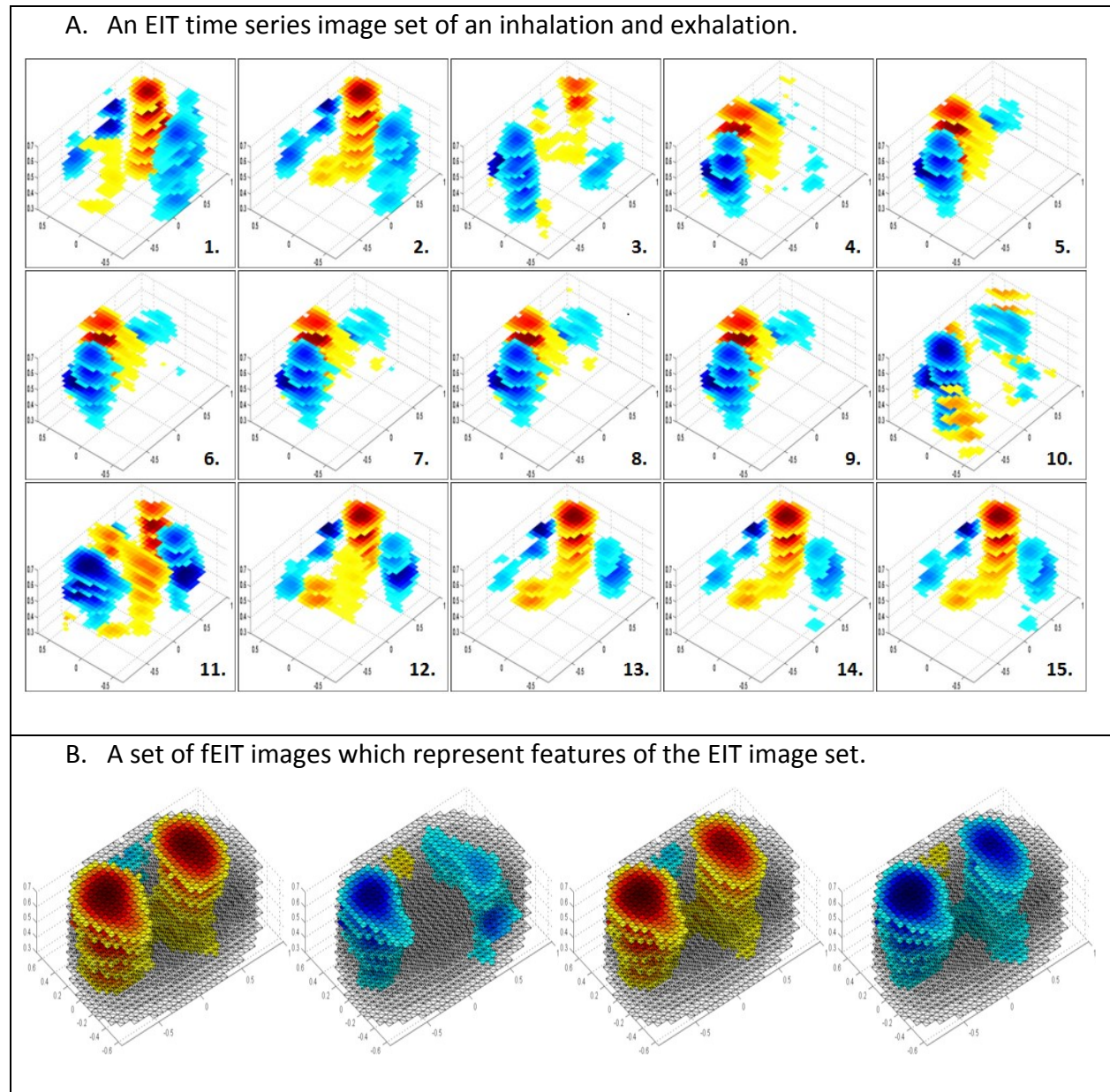


**Figure 6.13** The two image sets are taken from Subject 8 with the Planar measurement pattern in the Standing posture. The two sets illustrate the differences between raw EIT time series images and fEIT images which describe features of the times series image pixels. The first set of images shows every 10<sup>th</sup> image in a set of reconstructed images over one vital capacity breath. The second set of images represents four fEIT images generated using the four inhalation features described in Section 6.3.2.1.

The second set of images are the fEIT images generated from features  $f_1$ ,  $f_2$ ,  $f_3$ , and  $f_4$ . All four images do a good job of defining two lung columns. The image for  $f_2$  shows a smaller right lung column. This aspect derives from the action of the raw EIT images and the nature of  $f_2$ . Since the second feature is the first coefficient of the 3<sup>rd</sup> order polynomial fit,  $a_0$ , the value represents a base constant for a given pixel. The strong left column and weak right column is due to the difference in actual amplitude between the regions in any given EIT image. However, the fEIT images show that the change in pixel value in both regions is actually very similar.

The discrepancy between the left and right columns in the raw EIT images likely arises from the calculation of the reference measurement. The reconstruction method uses difference imaging in order to produce the images. This involves a homogeneous measurement (reference measurement) and a set of inhomogeneous measurements. For measurements on human subjects it is impossible to establish a homogenous measurement as the reference since the conductivity of the thorax is not homogenous. Instead, the reference can be taken as an initial state and the inhomogeneous measurements then represent changes from that state.

There are several different ways to establish a reference measurement for human measurements. A single image can be used, but this will be subject to system noise. A series of images can be averaged, but it is difficult for a subject to remain still enough to keep the noise level low. The approach taken here is to average a set of measurements closest to the minimum EIT average signal, and use that as the reference. The reference is then the conductivity of the thorax at residual capacity and the inhomogeneous measurements represent changes in lung volume with respect to that state. This approach is still susceptible to noise and likely causes poor lung region definition in the raw EIT image sets.

The four fEIT images for each pattern and posture generally show either a strongly positive (red) or strongly negative (blue) response in the lung regions. This is a result of the polarity of the EIT measurement. For the analysis that is done in this work, it is not important whether the fEIT image amplitude is largely positive or negative. Instead it is the defining of the active lung region and the observation of changes in the active lung region due to posture that are most relevant.

For a qualitative analysis, there are three questions that are most interesting. First, does the image present a reasonable lung region? Second, are the left and right lung regions distinguishable? Third, is the result consistent for all postures? The first two questions are used to give a score to each fEIT image. The scores are shown in Table 7-10 below. A score of 2 is given to an image with a clear central lung region. A score of 1 is given to an image with a possible lung region that is not central. A score of 0 is given to an image with no discernable lung region. The results in the tables were decided solely by the researcher, and are subject to the bias of the researcher. Less biased results could be obtained by gathering results from multiple 3<sup>rd</sup> party volunteers.

The qualitative results from the fEIT image set show that the Planar pattern produces high quality images but also has the highest rate of failure. The Zigzag Offset and Square patterns have high rates of success in capturing the lung regions. However, the Planar images that are of high quality have the most visible left-right lung column separation.

The four features used to generate the fEIT images produce a mix of results in terms of image quality. The overall lung region shape from feature to feature is similar. The pattern of Planar images having well-distinguished columns and Zigzag Offset and Square images being blobby but very consistent is seen in each feature. In many cases the four fEIT images for a given pattern and posture are very similar, especially between Feature 3 and Feature 4. However, there are also cases where one feature captures a quality lung region while another produces a poor image. This suggests that no single feature is able to adequately capture lung behaviour.

Feature 3 and Feature 4 provide largely similar images, with Feature 3 giving better quality. Feature 1 and Feature 3 are also quite similar in many images, but the lung regions are often shifted between the features. Feature 2 has the lowest quality overall, but there are instances where it is able to produce an image while the other features do not.

Overall, Feature 3 gives the highest quality images. Feature 3 shows the best results for the Square pattern with Features 1 and 4 being similar, and Feature 1 gives the best quality for the Zigzag Offset pattern. Feature 3 is the strongest pattern for the Planar pattern. For all features the Planar patterns sees much lower image quality than the other two patterns.

The decline posture has the poorest image quality in terms of posture. This is likely due to additional noise added to the system due to experimental process of taking the decline measurement. The subject has to climb onto the decline bench and lay back. With 17 cables attached to the subject, this is a difficult task. There were multiple occasions where an electrode became shifted out of place or detached. This may explain the lower rate of success of this posture.

**Table 7.** Qualitative Results of fEIT Images for Feature 1

Feature 1	Planar pattern				Zigzag Offset pattern				Square pattern			
	DEC	LIE	SIT	STAND	DEC	LIE	SIT	STAND	DEC	LIE	SIT	STAND
Sbj 01	2	2	2	2	2	2	2	2	2	2	2	2
Sbj 02	2	2	0	0	1	2	2	2	2	2	2	2
Sbj 03	0	0	2	NA	2	2	2	NA	2	2	1	NA
Sbj 04	2	0	0	0	1	2	2	2	2	2	2	2
Sbj 05	2	2	2	2	2	2	2	2	2	2	2	2
Sbj 06	0	0	0	0	2	2	2	2	2	2	2	2
Sbj 07	1	1	2	2	2	2	2	2	2	2	2	2
Sbj 08	2	2	2	0	2	2	2	2	2	2	0	0

**Table 8.** Qualitative Results of fEIT Images for Feature 2.

Feature 2	Planar pattern				Zigzag Offset pattern				Square pattern			
	DEC	LIE	SIT	STAND	DEC	LIE	SIT	STAND	DEC	LIE	SIT	STAND
Sbj 01	0	2	0	2	0	2	2	1	0	2	2	0
Sbj 02	2	2	2	2	1	2	2	1	2	2	2	2
Sbj 03	0	0	2	NA	2	2	2	NA	2	2	2	NA
Sbj 04	2	1	1	0	2	2	2	2	2	2	2	1
Sbj 05	2	2	0	1	0	0	1	2	2	0	2	1
Sbj 06	0	0	1	1	0	2	0	2	2	2	2	2
Sbj 07	0	0	0	2	2	2	2	2	2	2	2	2
Sbj 08	2	2	1	1	2	2	2	2	2	2	2	2

**Table 9.** Qualitative Results of fEIT Images for Feature 3.

Feature 3	Planar pattern				Zigzag Offset pattern				Square pattern			
	Dec	Lie	Sit	Stand	Dec	Lie	Sit	Stand	Dec	Lie	Sit	Stand
Sbj 01	2	2	0	2	2	0	2	2	2	2	2	2
Sbj 02	1	2	2	2	1	2	2	0	2	2	2	2
Sbj 03	2	1	2	NA	2	2	2	NA	2	2	1	NA
Sbj 04	0	2	1	1	1	2	1	2	2	2	2	2
Sbj 05	2	2	2	2	2	2	2	2	2	2	2	2
Sbj 06	2	1	1	2	2	2	2	2	2	2	2	0
Sbj 07	2	1	2	2	1	1	2	2	2	2	2	2
Sbj 08	2	2	2	1	2	2	1	1	2	2	2	2

**Table 10.** Qualitative Results of fEIT Images for Feature 4.

Feature 4	Planar pattern				Zigzag Offset pattern				Square pattern			
	DEC	LIE	SIT	STAND	DEC	LIE	SIT	STAND	DEC	LIE	SIT	STAND
Sbj 01	2	2	1	2	2	1	0	2	1	2	2	2
Sbj 02	0	2	2	2	1	2	2	1	2	2	2	2
Sbj 03	1	1	2	NA	2	2	2	NA	2	2	2	NA
Sbj 04	0	2	0	1	1	1	2	2	2	2	1	2
Sbj 05	2	2	2	2	2	2	2	1	2	1	2	2
Sbj 06	1	1	2	2	2	2	2	2	2	2	2	2
Sbj 07	1	0	1	0	2	2	1	1	1	1	2	2
Sbj 08	2	2	0	1	2	2	2	2	2	2	2	2

#### 6.4.3.2 Vertical Gravitational Effects using fEIT Images

The fEIT images described above are used to analyze the EIT data for vertical gravitational effects due to change in posture. The fEIT images are very useful for the task since they consist of one image of 5 layers which describe the lung behaviour during the breathing protocol. In order to observe changes in lung mechanics due to posture, the %Activity is calculated for each layer, which is the number of pixels in a layer which are greater or equal to  $\frac{1}{4}$  the maximum pixel amplitude in the image. This number is divided by the total number of pixels above the  $\frac{1}{4}$  maximum in the image to give a normalized value for each layer. The %Activity value then represents the size of the active region on each layer.

The expected result of imaging a subject's breathing in different postures is that the region of highest lung activity will shift. As the force of gravity shifts in orientation, the lung mechanics will be altered. It is expected that while standing, the most active region is in the lower lung region. When the subject moves to a decline posture, the lung activity will shift upwards.

In order to detect this shift, a linear line is fit to the %Activity vs. Image Layer data. The slope of the line is then plotted vs. posture for each feature and measurement pattern. Figure 6.14 shows the results of this process. The results for all subjects are plotted in each graph.

There is a lot of variability in the results for all three measurement patterns. The Square pattern shows the most consistent behaviour between subjects, and the Planar pattern is also quite consistent. The results for the Zigzag Offset pattern are very non-uniform between subjects. There is no clear trend in any of the images.

The results from the plots are averaged over all subjects and plotted in Figure 6.15 below. The results confirm that the Planar and Square patterns have much lower error in the trends than the Zigzag Offset pattern. The Planar results have lower error than the Square results. The line trends in general have a slight downward slope.

A paired t-test is used to analyze the statistical significance of the variation in %Activity slope when in different postures. This paired t-test uses the null-hypothesis that the %Activity slope results for all subjects for two different postures are from the same parent distribution, and determines whether the null-hypothesis can be rejected given a significance level of 5%. The t-test is performed by comparing the %Activity slope results each of the decline, supine, and sitting posture results to the standing posture. Results are calculated for each of the 4 fEIT images.

Results are shown in Table 11 below. The results are considered statistically significant when less than 0.05. Out of the 36 tests, only 5 results show significance. For the Planar pattern, the %Activity slope results for the decline posture was statistically different than that of the standing posture for features 1 and 2. The %Activity slope results for the supine (lay) posture was statistically different for feature 1. The Zigzag Offset pattern show statistically significant differences in %Activity slope for feature 4 for both decline vs. standing and supine vs. standing. The Square pattern does not show any statistically significant results.

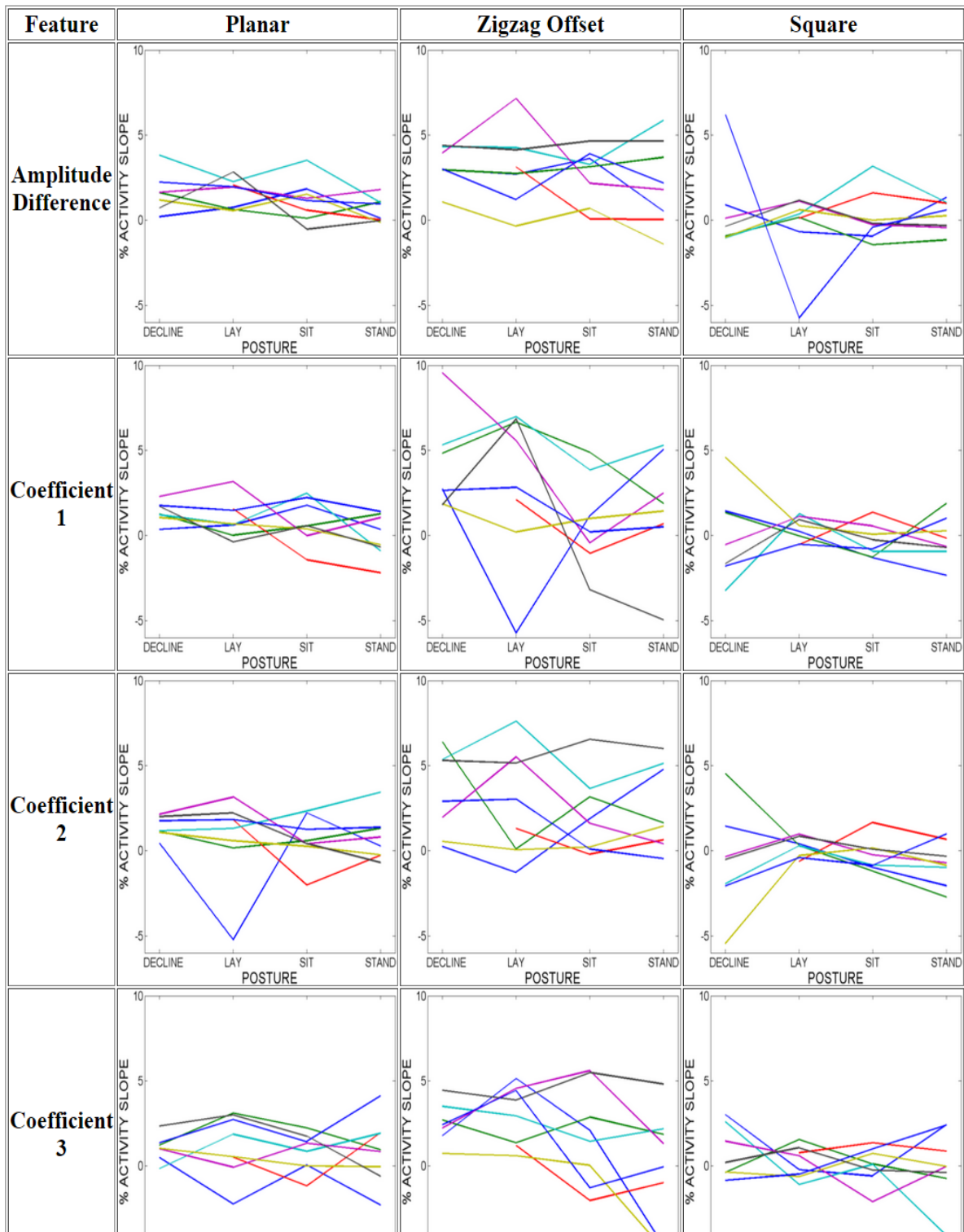


**Figure 6.14** A set of graphs of %Activity Layer Slope vs. Posture for all 8 subjects. Postures include decline, supine (lay), sitting, and standing. The slope of the %Activity vs. Image Layer is calculated for each posture and plotted for all subjects. Results are shown for the Planar, Zigzag Offset, and Square patterns and for all four features.

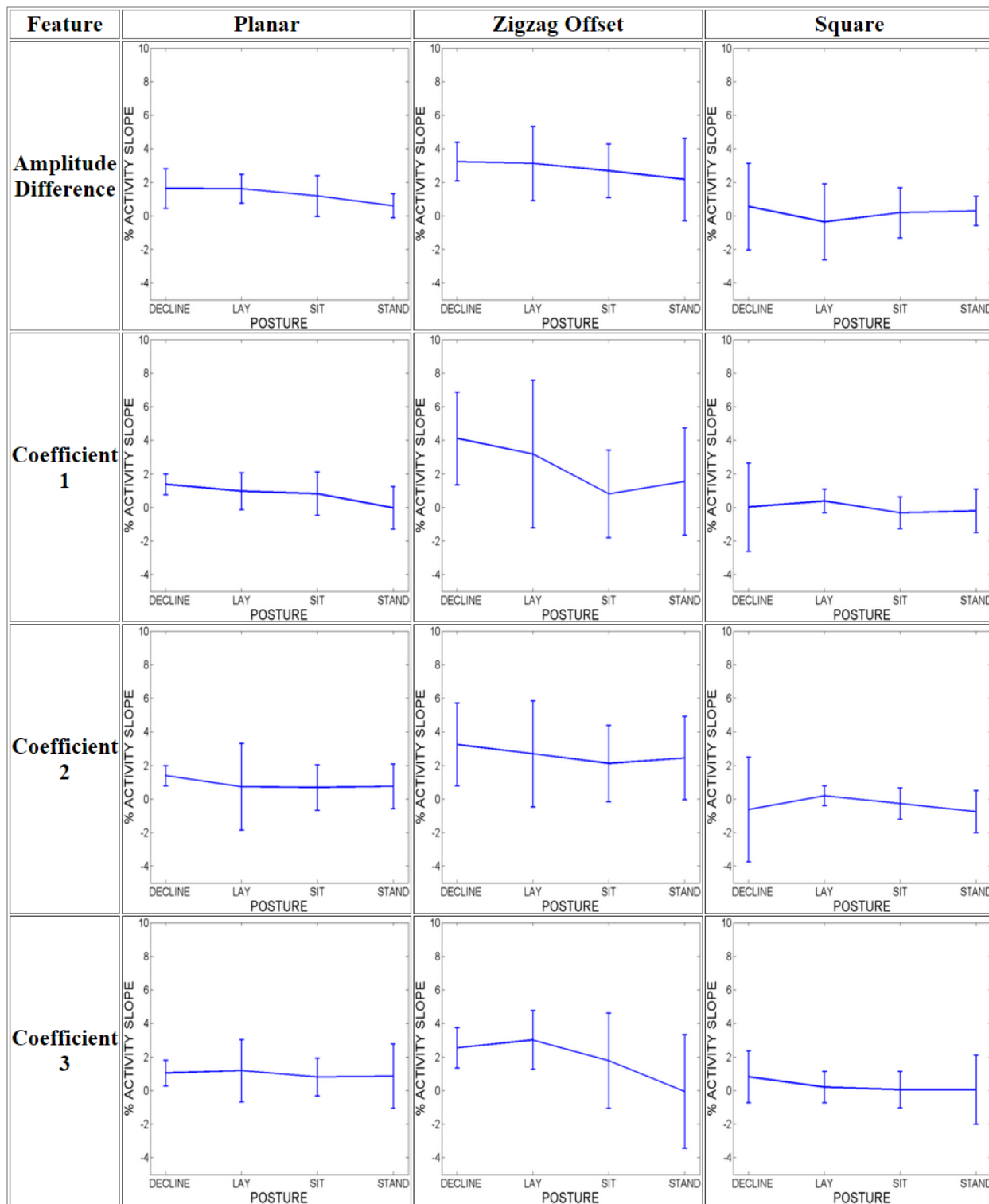


**Figure 6.15** A set of graphs of %Activity Layer Slope vs. Posture averaged over all 8 subjects. Posture includes decline, supine (lay), sitting, and standing. The trends are averaged from the results in Figure 6.14. Results are shown for the Planar, Zigzag Offset, and Square patterns and for all four features.

**Table 11.** The p-value results of paired t-test comparing %Activity slope values between postures. The significance is set to 5%.

p-values fEIT Feature	Planar			Zigzag Offset			Square		
	Decline vs. Stand	Lay vs. Stand	Sit vs. Stand	Decline vs. Stand	Lay vs. Stand	Sit vs. Stand	Decline vs. Stand	Lay vs. Stand	Sit vs. Stand
Amplitude Difference	<b>0.045</b>	<b>0.028</b>	0.234	0.266	0.302	0.435	0.708	0.509	0.830
Coefficient 1	<b>0.027</b>	0.105	0.123	0.114	0.487	0.390	0.834	0.365	0.844
Coefficient 2	0.431	0.982	0.879	0.654	0.849	0.566	0.834	0.141	0.237
Coefficient 3	0.692	0.612	0.953	<b>0.046</b>	<b>0.045</b>	0.136	0.466	0.855	0.996

## 6.5 Discussion

### 6.5.1 Spirometry vs. EIT

The purpose of the correlation analysis of the spirometry and EIT measurements is to verify that the 3D EIT measurements are producing a valid measure of the change in lung volume. This fact needs to be established for the following results to be valid. The results of the correlation test indicate that the EIT total lung volume is shown to correlate well with global lung volume spirometry measurements. The correlation is consistently above 80%, with the exception of Subjects 1 and 3. Subject 3 has especially low quality signals and can be considered an anomaly. The results therefore indicate that the 3D EIT measurements provide a valid representation of the change in global lung volume.

There are several sources of error that contribute to decrease in correlation. First, some error will arise due to the mismatch in timing between the spirometry device and the Goe-MF II EIT system. This could lead to small offsets in the timing of the measurements and reduce the quality. Second, the spirometer showed significant drift in lung volume which had to be corrected. This step may add significant error into the system.

There is a large difference in the RMSE results between subjects. This suggests a high variability in the experimental protocol such as the application of electrodes. It may also be related to subject physiology. The EIT experimental protocol should be improved to reduce this error.

There are no consistent trends in the results between different measurement patterns. Planar in general has a lower correlation and higher RMSE. However, the difference is negligible. There is little impact on the measurement of global lung volume by the selection of the measurement pattern.

### 6.5.2 Functional EIT Images

The generation of fEIT images is a useful way to analyze time series EIT data. The approach offers a concise way of summarizing temporal data over a spatial region, rather than directly analyzing time series data. The image can then be used to classify active and non-active regions in the lungs according to various features of the time series data. The behaviour is generally not obvious from directly observing the raw EIT images.

The fEIT images produced from the subject measurements provide very useful information. It is clear from the images that the 3D EIT approach is effective in detecting the lung region. This combined with the fact that there is good correlation between the spirometry and global EIT amplitude supports the idea that 3D EIT can provide useful information about lung function. However, the images also make clear that the technique is not at a stage where lung regions can be consistently and accurately defined.

The differences in the shape of the lungs produced by different measurement patterns is significant. The Planar pattern, when the quality is high, produces lung images with distinct columns for the left and right lungs. The Zigzag Offset and Square patterns tend to produce images showing a single central lung region with very little distinction between the left and right regions. However they are much more consistent in producing clear lung regions than the Planar pattern.

The difference in lung shape is likely due to the number of vertical and horizontal measurements involved in the respective measurements patterns. The electrode pairs in the Planar pattern are

primarily horizontal, with one diagonal pair involving a vertical measurement. The Zigzag Offset consists of diagonal electrode pairs, and the Square pattern is half horizontal and half vertical pairs. The Zigzag Offset and Square patterns likely lose some resolution in the XY plane and gain resolution in the Z direction.

The four fEIT images provide varied results between them. For many measurements the resulting images are quite similar. In others, one image may produce a well-defined lung region while another produces noise with no discernable lung region. This is an effect of using the coefficients of a fitted polynomial as features. Ideally, the coefficients represent unique aspects of lung function. These would be initial amplitude for F2, rate of amplitude increase for F3, and change in the rate of amplitude increase for F4. These features along with change in amplitude (F1) are all linked quite closely in terms of the dynamics of the lung system. It would potentially be useful as future work to look to combine the four fEIT images into a single image with a weighted summation or similar process.

### 6.5.3 Vertical Gravitational Effects

Analysis of the change in %Activity in the fEIT images with respect to posture shows some interesting results. The trends in Figure 6.15 provide a summary of the shift in %Activity on the 5 layers along with the error in the results for the 8 subjects. The results of this analysis indicate potential gravitational effects, as the general trend in the layer slope decreases when moving from decline to standing. A paired t-test was used to determine whether there was statistical significance in the %Activity slope results between each of the decline, supine, and sitting posture and the standing posture. Four results were found to be statistically significant: for the Planar pattern, decline vs. standing for fEIT features 1 and 2, and supine vs. standing for fEIT feature 1; and for the Zigzag Offset pattern, decline vs. standing and supine vs. standing for fEIT feature 4.

These results indicate that 3D EIT is capable of measuring vertical gravitational effects on lung mechanics due to change in posture. However, the method that has been used shows inconsistent results. Features 1 and 2 provided significant results for the Planar pattern while feature 4 provided significant results for the Zigzag Offset pattern. This inconsistency requires further investigation into the relationship between the selected feature and pattern

performance. There are a number of factors that may lead to the inconsistencies, including the small number of subjects, limitations in the analysis method, and error due to the experimental method and the EIT data collection.

In the slope analysis of the lung activity, a straight line is fit to the %Activity vs. Layer data for each posture. This means that a positive slope indicates higher activity in the upper lung region (towards layer 5) and a negative slope indicates higher activity in the lower lung region (towards layer 1). When the slope is plotted against Posture, a decrease in slope indicates a shift of the %Activity from the lower lung region to the upper lung region. This is a simplistic approach, as the %Activity trend is generally not smooth across the layers. This could be causing some of the high error seen between subjects. One advantage of the approach is that it captures a shift or movement in lung volume change across the layers rather than an absolute change in a given layer. Another advantage is that the shift in %Activity can be summarized in a single plot. Averaging the results over a number of subjects helps to normalize the trend.

The error levels in the plots reveal several points concerning the pattern performance. The Planar pattern and Square pattern have the lowest error. The high quality Planar images have the best resolution of the left and right lung columns. However, as mentioned in Section 6.5.2, the Planar pattern also has the highest occurrence low quality fEIT images. This suggests that while the Planar pattern produces images with the highest resolution in the XY plane, it is more susceptible to noise than the other patterns. This is an unexpected result, as the Planar and Planar Offset patterns had the best noise performance in the Simulations chapter. This does agree with the lower score of the Planar pattern in the Correlation and RSME tests in Sections 6.4.1 and 6.4.2.

The Square pattern can be considered to be the most stable measurement pattern. The pattern shows high consistency in the %Activity analysis between subjects. The pattern also has a high success rate of producing quality images with well-defined central lung regions. This agrees with results from the previous sections. In the Simulations chapter, the Square pattern showed the best noise performance after the Planar and Planar Offset patterns. In the Tank chapter the Square pattern produced medium quality images but is the most consistent across the X-Y plane.

However, the weaker planar and vertical resolution likely contributes to the absence of statistically significant results when comparing %Activity slope to posture.

The Zigzag Offset pattern shows the highest error in the %Activity slope results. This agrees with the results of the Simulations chapter. The pattern also shows the largest decrease in slope from decline to standing. This may be connected with the strong Z-Constraint performance from the Tank chapter. The Planar, Planar Offset, and Square patterns produced images with long vertical tails. The Zigzag and Zigzag Offset patterns were much better at detecting an edge in the Z direction. The strong Z-Constraint performance likely leads to the significant results in the %Activity slope vs. posture statistical test.

There are several differences in the performance of the patterns in terms of the simulations, tank phantom experiment, and human measurements experiment. The Planar pattern for example showed excellent noise performance in the simulations tests. However, the pattern performed the poorest in the correlation and RMSE analysis when compared to spirometer lung volume, and also showed the lowest rate of success of producing well-defined lung regions in the fEIT images. This discrepancy shows illustrations the necessity of performing real data acquisition. The sources of error increases when moving from simulations to tank phantom to human measurements. The simulations are extremely useful in characterizing specific aspects of pattern performance in a controlled test. However, images from human subjects may not reflect the simulation results since there will be additional sources of noise. Additionally, there will always be a degree of error in attempting to simulate a real set of measurements. In other words, each stage is significant and in each test there are many aspects of experimental design to consider when attempting to produce meaningful results.

Future work on this topic should include exploring ways to improve upon the performance of the patterns, especially the Planar and Zigzag Offset patterns. Improvements can be made to the reconstruction method, to the electrode placement strategy, and to noise reduction. An analysis of the stimulation and measurement electrode pair spacing in the measurement protocol would also be useful to explore the effects on quality. Work has already been done previously in this area by Y. Mamatjan [9].

The fact that the electrode pattern has such a large impact on the shape of the lung region suggests that there is room for improvement in the XY resolution of this 3D imaging approach. The difference in the shape of the lung regions between the Planar pattern and the Zigzag Offset and Square patterns suggest that the ratio of vertical to horizontal measurements has a strong effect on resolution in the XY plane. A pattern which has a vertical-horizontal ratio somewhere between the Planar pattern (15 out of 16 horizontal) and the Zigzag Offset and Square patterns (50-50 ratio) may improve the results.

## 7 Conclusion

This thesis has three main objectives relating to 3D EIT. First, to examine different measurement patterns and determine the best-suited pattern for 3D imaging of regional inhomogeneities in the lungs. Second, to verify the ability of 3D EIT images to measure global lung volume changes by comparing results with spirometry lung volume measurements. Third, to capture regional inhomogeneities in the lungs by recording EIT on human subjects in the standing, sitting, supine, and decline postures.

The body of work includes a characterization of the 3D GREIT method, a simulations chapter, a tank phantom experiment chapter, and a human measurements chapter. The 3D GREIT method is a new 3D EIT reconstruction approach used in this thesis. The goals of the Simulations and Tank Phantom chapters are to characterize the performance of the 7 selected 3D EIT measurement patterns under various controlled conditions. The three most suitable patterns are then selected to be used in the *in vivo* trial in the Human Measurements chapter. This last chapter describes the results of EIT measurements taken on healthy human subjects with the aim of achieving the three goals of the thesis.

In the Simulations chapter, several tests are performed to characterize the noise performance of the 7 measurement patterns under various conditions. The performance is analyzed using the five GREIT parameters and a proposed Noise Stability measure. Both metrics are used to evaluate each measurement protocol against Electrode Placement error and Electrode Impedance error.

The results of the tests indicate that the measurement pattern has a significant effect on noise performance. Aligned and Offset patterns perform similarly for most tests. The patterns are grouped as follows: Planar and Planar Offset; Zigzag and Zigzag Offset; Square; and Planar Opposite and Zigzag Opposite. The last group has very poor performance in most tests. Of the remaining groups, Planar and Planar Offset have the best noise performance. Square is the next strongest performer, followed by Zigzag and Zigzag Offset.

In general, the simulations show several useful trends. There is an overall increase in Position Error and an improvement in Resolution when moving towards the edges of the model. The seven

patterns had similar performance on the centre plane, and saw a decrease in performance to varying degrees of Position Error and Resolution when moving away from the centre. Also, increasing the noise levels in a simulation has a stronger effect on the central regions than the outer layers.

In the Tank chapter a phantom tank experiment is performed in which 3D EIT measurements are taken of a plastic block in 15 positions. The process is repeated for all 7 patterns. The resulting images are reconstructed using the 3D GREIT method and are analyzed using the GREIT parameters and a novel Z-Constraint parameter.

The patterns again separate into groups with similar results. The Planar Opposite and Zigzag Opposite patterns show very poor performance in all tests, which is similar to the Simulations results, and are discarded as unsuitable measurement patterns. The Planar and Planar Offset patterns have high resolution in the XY plane but see a spreading effect when the block is close to the edge. This effect is opposite to the results of the Simulations chapter where the Planar and Planar Offset see better performance than the other patterns.

In order to characterize the performance of the measurement patterns along the z-axis, the Z-Constraint score has been developed. This parameter is a means of measuring how well the edges of a reconstructed object are defined along the z-axis. The reconstructed images show that the Planar, Planar Offset, and Square patterns see a significant tailing effect in the Z direction. However, when the  $\frac{1}{4}$  maximum point is used to define an edge, the results for the different patterns are closer. The Planar and Zigzag Offset patterns have the strongest performance in the Z-Constraint analysis. The Planar pattern has very good Z-Constraint towards the edge of the tank than at the centre while the Zigzag Offset pattern is fairly uniform across the tank radius. The Square pattern is the most uniform over the tank radius although it has low overall scores.

A difference in electrode plane spacing is shown to have a significant impact on some patterns. The Zigzag, Zigzag Offset, and Square patterns have lower resolution when the spacing is increased. The effect is much smaller on the Planar and Planar Offset results.

The groupings of the results of the patterns suggest that the image quality in a multiplane electrode arrangement is significantly affected by the orientation of the electrode pairs. The Planar and Planar Offset patterns consist mostly of horizontal electrode pairs in the stimulation and measurement protocol. The Square pattern consists of half horizontal and half vertical electrode pairs. The Zigzag pattern consists of half diagonal and half vertical pairs while the Zigzag Offset pattern consists of only diagonal pairs. The number of vertical, diagonal, and horizontal electrode pairs clearly has a strong effect on different aspects of the image quality, with the Planar and Planar Offset patterns excelling in some tests and the Zigzag and Zigzag Offset patterns excelling in others. This fact suggests that there may be patterns with ratios between the Planar and Zigzag patterns that may improve overall results.

The results of the Simulation and Tank chapters are used to select three suitable patterns to be used in the Human Measurements experiment. The Planar, Zigzag Offset, and Square patterns are selected. The Square pattern does not have the best overall performance but has consistent radial performance. Furthermore, the Planar Offset or Zigzag patterns are not selected because they share similar traits to other two selected patterns and would duplicate the results. Rather than verify that the patterns would have similar results, the Square pattern has been selected in order to increase the diversity of the results.

The purpose of the Human Measurements chapter is to achieve the goals of the thesis: to establish the ability of 3D EIT to capture global lung volume change; to use 3D EIT to observe vertical gravitational effects on regional lung activity due to change in posture; and to use the results to compare the performance of the 3D measurement patterns.

The results of comparing the EIT and spirometry data indicate a strong correlation between global amplitude in EIT and lung volume change in spirometry. The correlation is above 80% in most cases, and the RMSE remains below 2.5%. The significant drift apparent in the spirometry data adds a degree of error into the correlation and RMSE analysis, and results could be potentially be improved by adjusting the experimental methodology. Unlike the spirometry measurements, the EIT data are very stable over time, which is a useful feature for capturing lung volume change.

Overall the results show that the 3D EIT is able to capture meaningful data and is suitable for measuring lung mechanics.

The next step in the analysis compares the ability of the Planar, Zigzag Offset, and Square measurement patterns to capture regional lung inhomogeneities in a volume. 3D EIT offers the potential to increase the information provided by 2D EIT imaging by adding vertical resolution to the image. The approach can also improve resolution in the X-Y plane by reducing off-plane effects of surrounding tissues, as demonstrated in Section 3.2.2.

Regional lung inhomogeneities often arise due to serious medical conditions. This study uses healthy subjects, so regional lung inhomogeneity is introduced while recording EIT with the subject in different postures. By having the subjects perform a breathing protocol in the standing, sitting, supine, and decline postures the gravitational effect on the lungs is varied in the vertical direction. The ability of 3D EIT to detect vertical change in lung mechanics would support its usefulness as a tool to measure regional inhomogeneities.

The EIT data are reconstructed to form time series EIT image sets. The image sets do not consistently present clearly defined lung regions for any of the patterns. Therefore, a set of functional EIT (fEIT) images are calculated based on the features of the inhalation curve. The resulting images present well-defined active lung regions for most cases. The poor results of the EIT images may be due to the method used to calculate the reference measurement. Future experimental protocols should be designed to capture a better reference image.

The Square and Zigzag Offset patterns have high success rates at defining lung regions. The Planar pattern on the other hand has mixed results. The success rate for the Planar pattern is much lower than for the other patterns. However, the Planar images that are of higher quality have much better lung region definition than the images of the other two patterns. The Planar pattern is able to discern two well-defined lung columns whereas the other two patterns image one central region with little distinction between the left and right lung columns. This is again likely due to the higher number of horizontal electrode pairs in the Planar pattern.

The results from the vertical activity analysis of the lung images provide encouraging signs in the ability to detect differences in regional lung behaviour. There is a consistent downward trend in the slope of the %Activity scores across the different reconstruction layers when moving from the decline posture to the standing posture. This indicates a shift in lung activity from the upper lung region towards the lower lung region when moving from decline to standing. This is the expected result according to the gravitational influence.

A paired t-test is used to determine the statistical significance of changes in the %Activity slope due to change in posture by comparing the results for the decline, supine, and sitting postures to the standing posture. Results indicate that the decline and supine postures produced significant changes in %Activity slope for both the Planar and Zigzag Offset patterns. For the Planar pattern, the decline results are significant for feature 1 and 2 fEIT images and the supine results are significant for the feature 1 fEIT image. For the Zigzag Offset pattern, the decline and supine results are significant for the feature 4 fEIT image.

The inconsistency in the results for the different features suggests that the methodology of this experiment requires further refinement. In order to improve on the results several steps can be taken, including reducing noise in the measurements, improving electrode placement accuracy, and improving the reconstruction algorithm.

Overall, the Planar and Zigzag Offset patterns have the strongest performance. Although they excel in different areas for most of the tests that have been performed. The Planar pattern has lower change in %Activity slope but also lower error than the Zigzag Offset pattern. While the Zigzag Offset pattern has higher error in the %Activity slope, it is able to show more consistently a well-defined lung region in the fEIT images.

The Planar pattern produces images with the most well-defined lung region, but fails to do so consistently. The Simulations chapter indicates that the pattern is quite resilient to noise. The Tank chapter shows that the pattern is less vulnerable to layer separation error. However, the *in vivo* results clearly show a vulnerability to noise.

The strong performance of the Planar pattern and the Zigzag Offset pattern can be discussed in light of the horizontal to vertical electrode pair ratio. Again, the Planar pattern uses primarily only horizontal pairs, while the Zigzag Offset pattern uses only diagonal pairs. Since the Planar pattern has strong resolution in the XY plane but is susceptible to noise, and the Zigzag Offset pattern shows good Z-Constraint but lower resolution and noise performance, it can be postulated that results can be improved if the measurement pattern has a horizontal to vertical electrode pair ratio between 16:1 and 1:1.

In summary, the three goals of the thesis have been achieved to varying degrees of success. First, the Planar and Zigzag Offset patterns have been identified as patterns capable of measuring regional inhomogeneities with 3D spatial resolution. The patterns have performed quite differently in the tests performed throughout this work which that a better pattern may be found with features of both of these patterns. Second, the 3D EIT approach has been shown to be a suitable measurement technique for lung mechanics with reasonably accurate measurement of change in lung volume when compared with spirometry measurements.

Finally, the analysis of the %Activity vs. Posture data indicates that there are detectable gravitational effects that arise due to posture, although the results are inconsistent. Both Planar and Zigzag Offset showed statistically significant differences in the %Activity slope between the decline and standing posture and the supine standing posture. The approach is promising but steps need to be taken in future work in order to improve the measurement of regional lung inhomogeneities using 3D EIT.

## 7.1 Future Work

The work completed in this thesis indicates that 3D EIT has the potential to provide important and useful information on lung mechanics. However, there are clear areas that require further development. Future work will include the following:

1. Explore additional variations in measurement patterns. This may include the measurement pattern, as well as varying the separation between the stimulation and measurement electrodes. The results of this thesis suggest that a pattern consisting of a

horizontal to vertical electrode pair ratio between the Planar and Zigzag Offset patterns may provide the best results.

2. Improve raw 3D EIT images to properly display lung images in real time. This will involve several steps. First, improving the protocol for establishing the reference measurement. Second, improving accuracy of electrode placement during the measurement protocol and in the forward model. Third, applying a time-averaging technique to EIT time series measurement frames.
3. Improvements to 3D GREIT method. The immediate aspect to improve is to allow for control of the weighting on each layer. This will give lower focus on outer layers and may improve resolution towards the centre.
4. Apply pattern classification techniques to the identification of active lung regions. This has already been attempted in work done by C. Gómez-Laberge [36] and has strong potential in EIT image analysis.
5. Explore the effect of feature selection on fEIT images, specifically in terms of vertical gravitational effects due to posture changes. Select a single most useful fEIT feature or develop a single summary fEIT image comprised of multiple features.
6. Investigate the effects of 3D reconstruction algorithms and algorithm parameters on simulated error results presented in Chapter 4. Determine whether inconsistent noise performance in simulations is an effect of reconstruction algorithm.

## References

- [1] D. Holder, *Electrical Impedance Tomography: Methods, History, and Applications*, Bristol, UK: IOP Publishing Ltd., 2005.
- [2] E. Teschner and M. Imhoff, "Electrical Impedance Tomography: The realization of regional ventilation monitoring," [Online]. Available: [http://www.draeger.com/sites/assets/PublishingImages/Generic/UK/Booklets/rsp\\_eit\\_booklet\\_9066788\\_en.pdf](http://www.draeger.com/sites/assets/PublishingImages/Generic/UK/Booklets/rsp_eit_booklet_9066788_en.pdf). [Accessed 24 03 2014].
- [3] A. Adler, M. B. Amato, J. H. Arnold, R. Bayford, M. Bodenstern, S. H. Bohm, B. H. Brown, I. Frerichs, O. Stenqvist, N. Weiler and G. K. Wolf, "Whither lung EIT: Where are we, where do we need to go, and what do we need to do to get there?," *Physiol Meas*, vol. 33, pp. 679-694, 2012.
- [4] G. K. Wolf, C. Gomez-Laberge, J. N. Kheir, D. Zurakowski, B. Walsh, A. Adler and J. H. Arnold, "Reversal of dependent lung collapse predicts response to lung recruitment in children with early acute lung injury.," *Pediatric Critical Care Medicine*, vol. 13, no. 5, pp. 509-515, 2012.
- [5] Z. Zhao, R. Fischer, I. Frerichs, U. Muller-Lisse and K. Moller, "Regional ventilation in cystic fibrosis is measured by electrical impedance tomography.," *Journal of Cystic Fibrosis*, vol. 11, pp. 412-418, 2012.
- [6] A. Adler, "Modeling EIT current flow in a human thorax model," EIDORS, 03 11 2010. [Online]. Available: <http://eidors3d.sourceforge.net/tutorial/netgen/extrusion/thoraxmdl.shtml>. [Accessed 11 04 2015].
- [7] A. Adler, P. Gaggero and Y. Maimaitjiang, "Adjacent Stimulation and Measurement Patterns Considered Harmful," *Physiol Meas*, vol. 32, no. 7, pp. 731-744, 2010.
- [8] B. Graham and A. Adler, "Electrode Placement Configurations for 3D EIT," *Physiol Meas*, vol. 28, no. 7, pp. S29-44, 2007.
- [9] Y. Mamatjan, S. Ahn, T. Oh and A. Adler, "Optimized electrode positions and stimulation patterns in head EIT," in *Canadian Medical and Biological Engineering Society (CMBEC 35)*, Halifax, 2012.
- [10] A. Adler, J. H. Arnold, R. Bayford, A. Borsic, B. Brown, P. Dixon, T. J. C. Faes, I. Frerichs, H. Gagnon, Y. Garber, B. Grychtol, G. Hahn, W. R. B. Lionheart, A. Malik, R. P. Patterson and J. Stocks, "GREIT: a unified approach to 2D linear EIT reconstruction of lung images," *Physiol Meas*, vol. 30, no. 6, pp. S35-55, 2009.

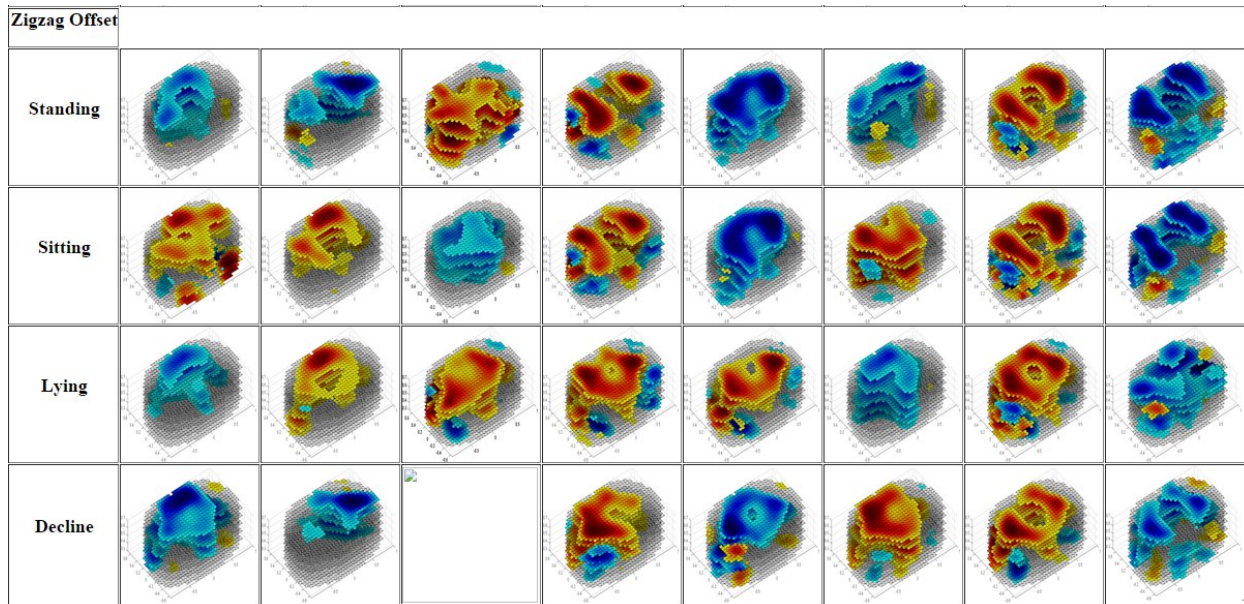
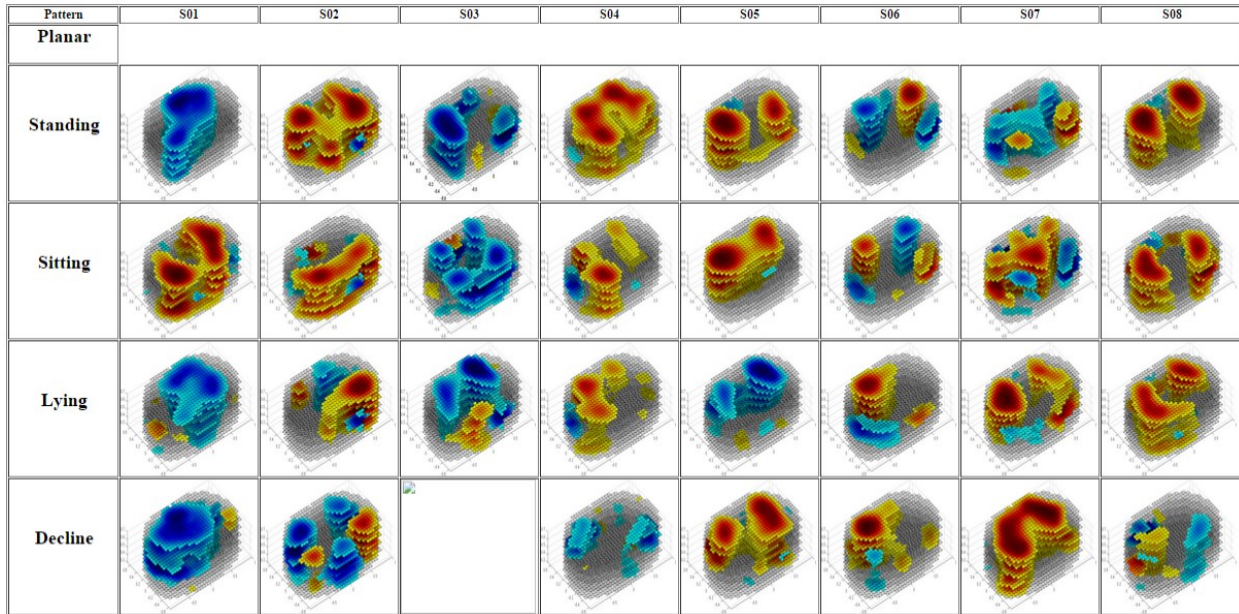
- [11] A. Adler, "Electrical Impedance Tomography: advances in Image Reconstruction," in *EIT Workshop*, Haarlem, Netherlands, 2006.
- [12] B. H. Brown, "Electrical impedance tomography (EIT): a review," *Journal of Medical Engineering and Technology*, vol. 27, no. 3, pp. 97-108, 2003.
- [13] A. Adler, P. Gaggero and Y. Maimaitijiang, "Distinguishability in EIT using a hypothesis-testing model," *Journal of Physics: Conference Series*, vol. 224, no. 1, 2010.
- [14] B. Graham and A. Adler, "A nodal jacobian inverse solver for reduced complexity EIT reconstructions," *International Journal of Information and Systems Sciences*, vol. 2, no. 4, pp. 453-468, 2006.
- [15] P. Metherall, D. C. Barber, R. H. Smallwood and B. H. Brown, "Three-dimensional electrical impedance tomography," *Nature*, vol. 380, pp. 509-512, 1996.
- [16] N. Polydorides and W. R. B. Lionheart, "A Matlab toolkit for three-dimensional electrical impedance tomography: a contribution to the Electrical Impedance and Diffuse Optical Reconstruction Software project," *Measurement Science and Technology*, vol. 13, pp. 1871-1883, 2002.
- [17] D. R. Stephenson, J. L. Davidson, W. R. H. Lionheart, B. D. Grieve and T. A. York, "Comparison of 3D Image Reconstruction Techniques using Real Electrical Impedance Measurement Data," in *4th World Congress on Industrial Process Tomography*, Aizu, Japan, 2005.
- [18] B. Graham and A. Adler, "Electrode Placement Strategies for EIT," in *World Congress on Medical Physics and Biomedical Engineering 2006*, Seoul, Korea, 2006.
- [19] Y. Mamatjan, D. GURSOY and A. Adler, "Electrode positions and current patterns for 3D EIT," in *Proceedings of 12th international conference in electrical impedance tomography (EIT 2011)*, Bath, 2011.
- [20] Dräger Medical GmbH, "Electrical Impedance Tomography," [Online]. Available: [http://www.draeger.com/sites/assets/PublishingImages/Generic/UK/Case%20Studies/rs\\_p\\_eit\\_br\\_9050980\\_en.pdf](http://www.draeger.com/sites/assets/PublishingImages/Generic/UK/Case%20Studies/rs_p_eit_br_9050980_en.pdf). [Accessed 08 04 2005].
- [21] S. Leonhardt, "EIT, Progress in perfusion imaging with," in *EIT2014*, Gananoque, CAN, 2014.
- [22] A. P. Bagshaw, A. D. Liston, R. H. Bayford, A. Tizzard, A. P. Gibson, A. T. Tidswell, M. K. Sparkes, H. Dehghani, C. D. Binnie and D. S. Holder, "Electrical impedance tomography of human brain function using reconstruction algorithms based on the finite element method," *NeuroImage*, vol. 20, no. 2, pp. 752-764, 2003.

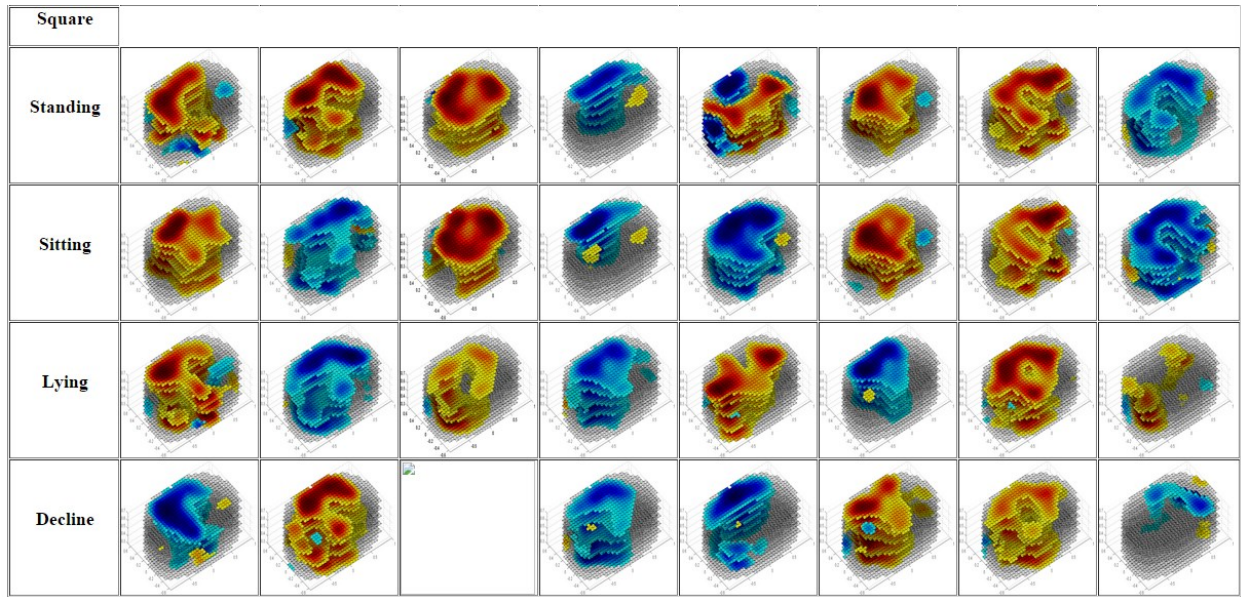
- [23] T. Tidswell, A. Gibson, R. H. Bayford and D. S. Holder, "Three-dimensional electrical impedance tomograph of human brain activity," *NeuroImage*, vol. 13, pp. 283-294, 2001.
- [24] Y. Mamatjan, S. Ahn, T. Oh and A. Adler, "Optimized electrode positions and stimulation patterns in head EIT," in *Canadian Medical and Biological Engineering Society (CMBEC 35)*, Halifax, 2012.
- [25] V. Cherepenin, A. Karpov, A. Korjenevsky, V. Kornienko, A. Mazaletskaia, D. Mazourov and D. Meister, "A 3D electrical impedance tomography (EIT) system for breast cancer detection," *Physiological Measurement*, vol. 22, pp. 9-18, 2001.
- [26] D. D. Pak, N. I. Rozhkova, M. N. Kireeva, M. V. Ermoshchenkova, A. A. Nazarov, D. K. Fomin and N. A. Rubtsova, "Diagnosis of breast cancer using electrical impedance tomography," *Biomedical Engineering*, vol. 46, no. 4, pp. 154-157, 2012.
- [27] M. Assenheimer, O. Laver-Moskovitz, D. Malonek, D. Manor, U. Nahaliel, R. Nitzan and A. Saad, "The T-SCAN technology: electrical impedance as a diagnostic tool for breast cancer detection," *Physiological Measurements*, vol. 22, pp. 1-8, 2001.
- [28] I. Frerichs, T. Dudykevych, J. Hinz, M. Bodenstern, G. Hahn and G. Hellige, "Gravity effects on regional lung ventilation determined by functional EIT during parabolic flights," *Journal of Applied Physiology*, vol. 91, no. 1, pp. 39-50, 2001.
- [29] S. Nebuya, M. Noshiro, A. Yonemoto, S. Tateno, B. H. Brown, R. H. Smallwood and P. Milnes, "Study of the optimum level of electrode placement for the evaluation of absolute lung resistivity with the Mk3.5 EIT system," *Physiol Meas*, vol. 27, pp. S129-S137, 2006.
- [30] M. Noshiro, K. Ebihara, E. Sato, S. Nebuya and B. H. Brown, "Effects of body position on lung density estimated from EIT data," in *International Conference on Electrical Bioimpedance*, 2010.
- [31] J. Wagenaar, B. Grychtol and A. Adler, "An Approach to Extend GREIT Image Reconstruction to 3D," in *EIT2014*, Gananoque, 2014.
- [32] Y. Asfaw and A. Adler, "Automatic detection of detached and erroneous electrodes in electrical impedance tomography.," *Physiol Meas*, vol. 26, no. 2, pp. 175-183, 2005.
- [33] B. H. Blott, G. J. Daniell and S. Meeson, "Electrical impedance tomography with compensation for electrode positioning variations," *Phys. Med. Biol.*, vol. 43, pp. 1731-1739, 1998.

- [34] A. Lozano, J. Rosell and R. Pallás-Areny, "Errors in prolonged electrical impedance measurements due to electrode repositioning and postural changes," *Physiol Meas*, vol. 16, pp. 121-130, 1995.
- [35] A. Adler, B. Grychtol, P. Gaggero, J. Justiz, V. Koch and Y. Mamatjan, "Data Quality in EIT," in *ICEBI2013*, Heilbad Heiligenstadt, 2013.
- [36] C. Gomez-Laberge, M. J. Hogan, G. Elke, N. Weiler, I. Frerichs and A. Adler, "Data-driven classification of ventilated lung tissues using electrical impedance tomography.," *Physiol Meas*, vol. 32, no. 7, pp. 903-915, 2001.

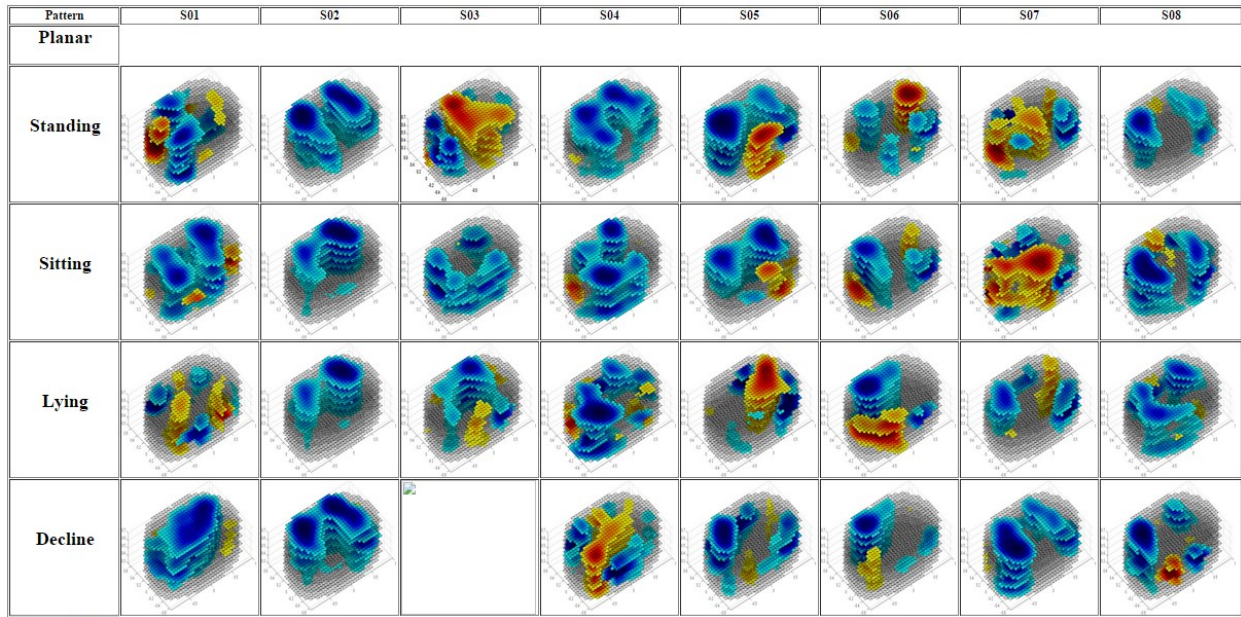
# Appendix A

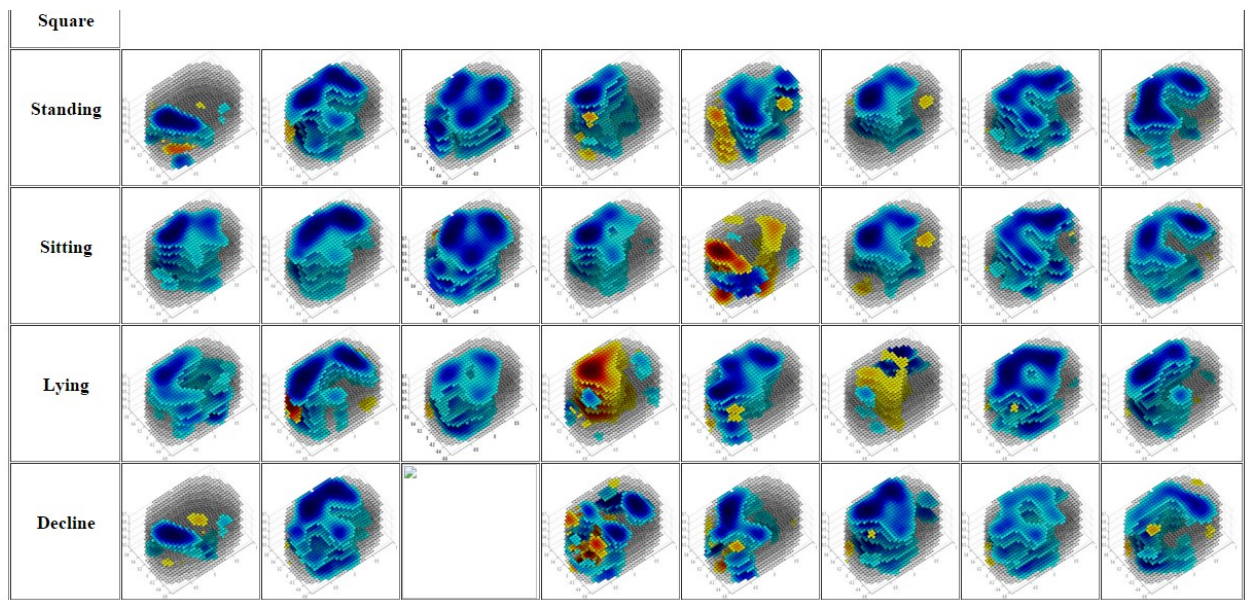
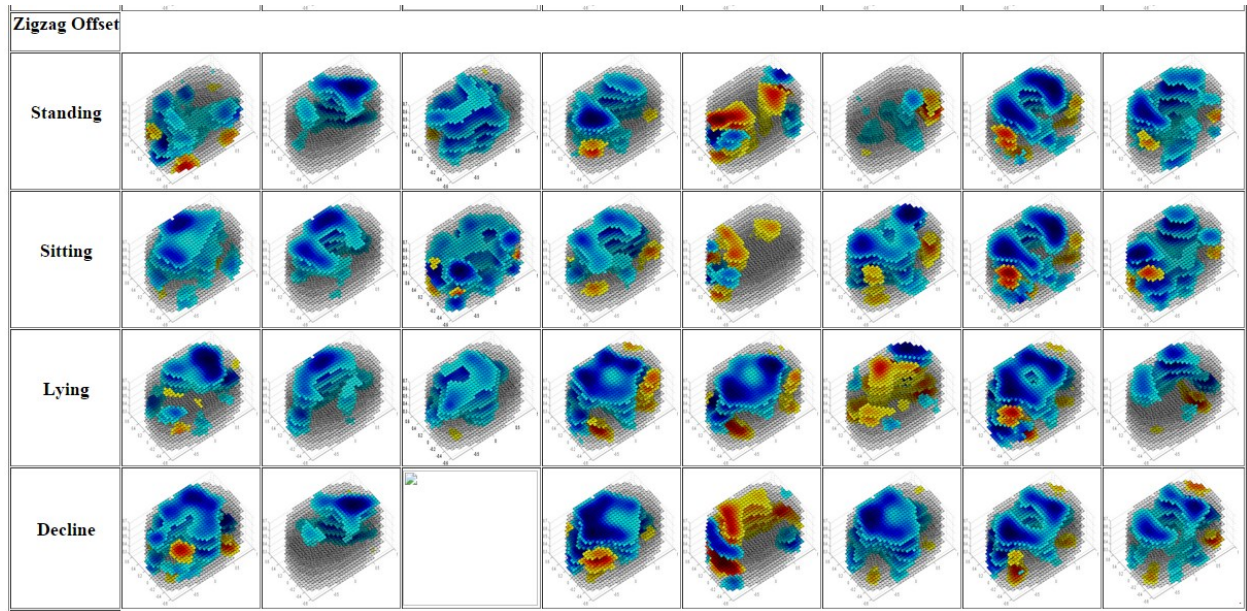
Function EIT Image 1: Amplitude Difference



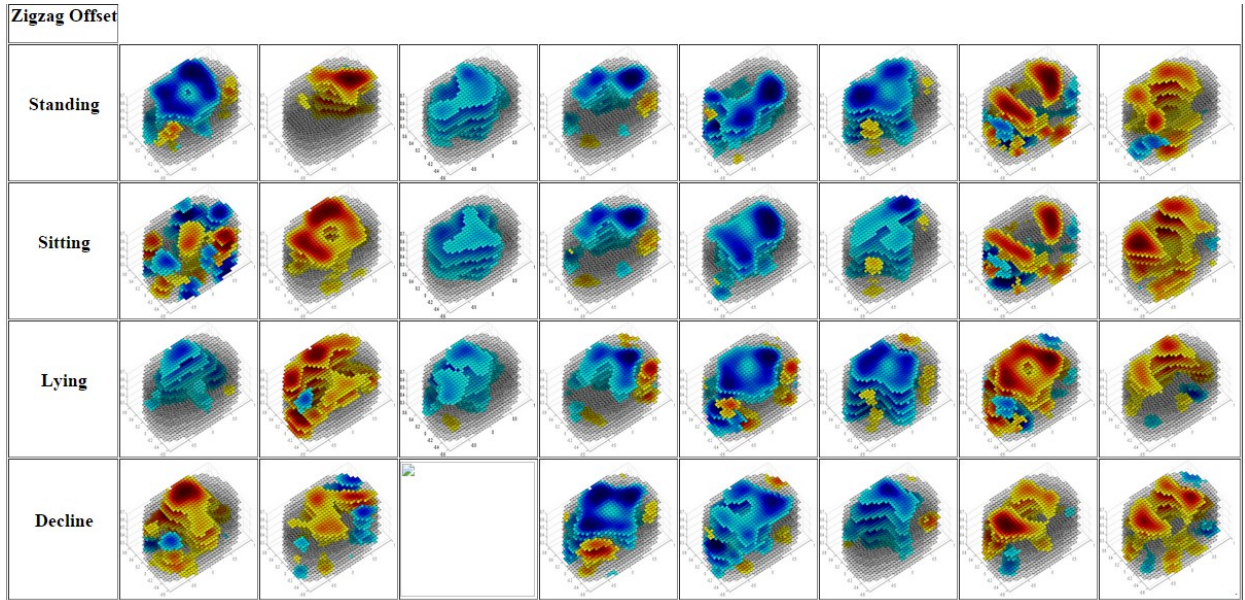
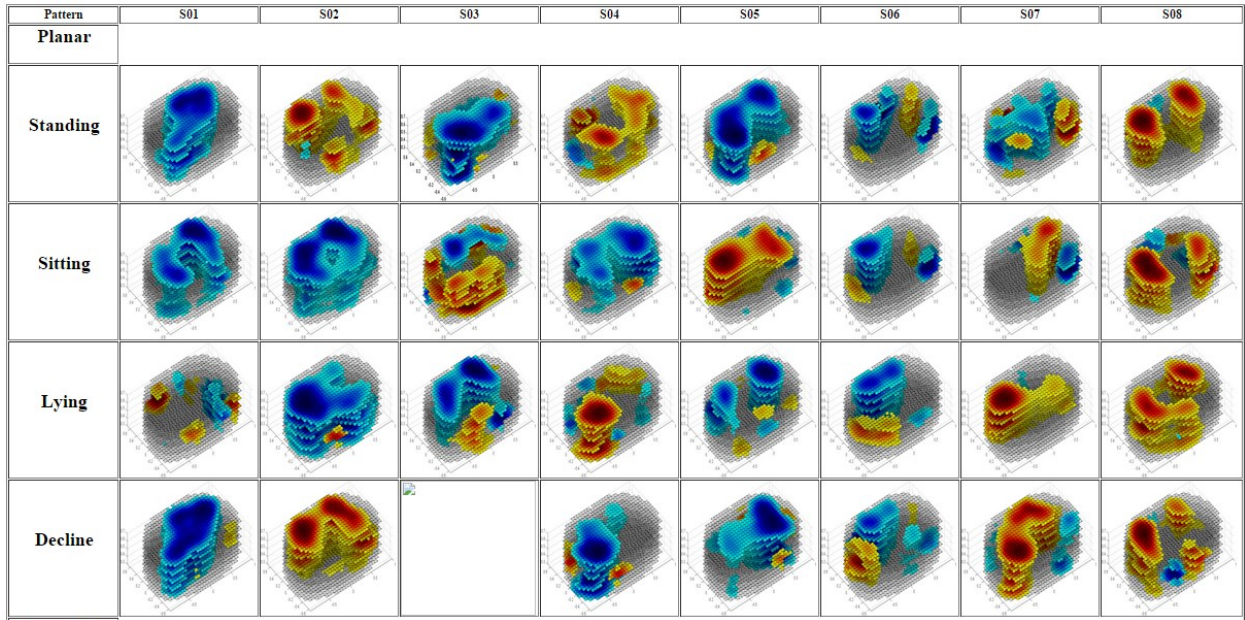


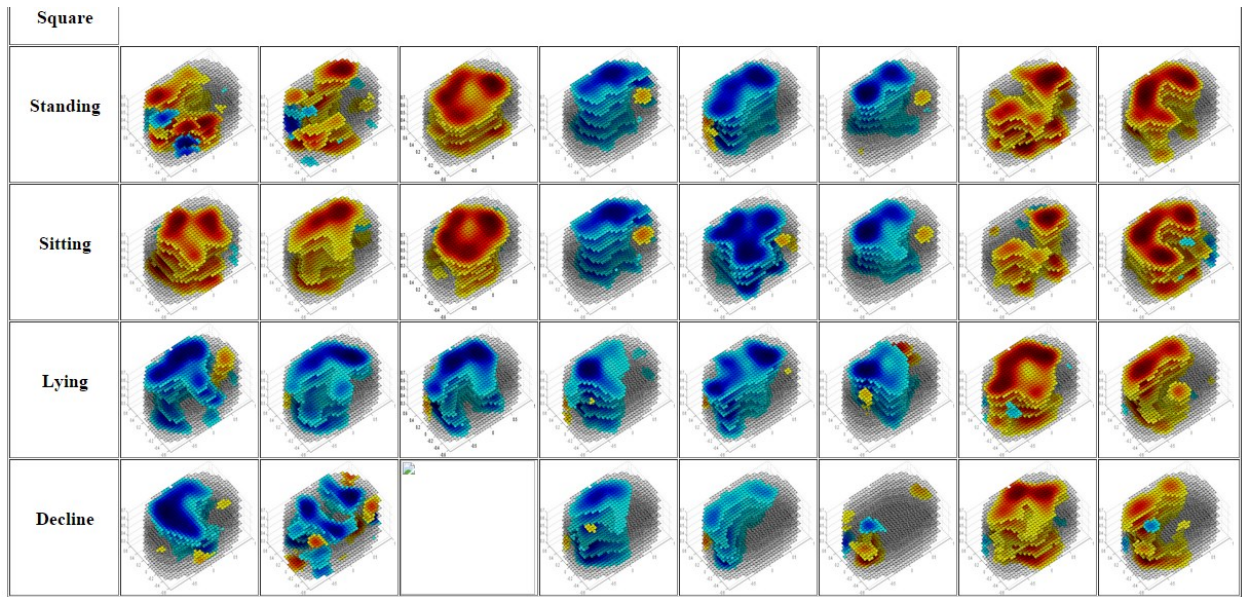
Function EIT Image 2: Polynomial Coefficient  $a_0$





Function EIT Image: Polynomial Coefficient a1





Function EIT Image: Polynomial Coefficient a2

